DETECTION AND MEASUREMENT OF
SHALLOW WATER EXPLOSIVE SOUNDS
RECEIVED AT AN ARRAY OF
GEOPHONES AND HYDROPHONES.

J.F. Green
L.C. Weltman
T.J. Cohen

ENSCO, Inc.
SAR Division
Springfield, Virginia   22151

16 January 1981

FINAL REPORT

Approved for Public Release, Distribution Unlimited

Prepared for

Office of Naval Research
Arlington, Virginia   22217

REPORT DOCUMENTATION PAGE		READ INSTRUCTIONS BEFORE COMPLETING FORM
1. REPORT NUMBER	2. GOVT ACCESSION NO. AD-A095478	3. RECIPIENT'S CATALOG NUMBER
4. TITLE *(and Subtitle)* DETECTION AND MEASUREMENT OF SHALLOW WATER EXPLOSIVE SOUNDS RECEIVED AT AN ARRAY OF GEOPHONES AND HYDROPHONES		5. TYPE OF REPORT & PERIOD COVERED FINAL
		6. PERFORMING ORG. REPORT NUMBER SAR(1396)-FR-80-01
7. AUTHOR(s) J.F. Green L.C. Weltman T.J. Cohen		8. CONTRACT OR GRANT NUMBER(s) N00014-80-C-0420
9. PERFORMING ORGANIZATION NAME AND ADDRESS ENSCO, Incorporated SAR Division Springfield, VA 22151		10. PROGRAM ELEMENT, PROJECT, TASK AREA & WORK UNIT NUMBERS
11. CONTROLLING OFFICE NAME AND ADDRESS Office of Naval Research Arlington, VA 22217		12. REPORT DATE 16 January 1981
		13. NUMBER OF PAGES 147
14. MONITORING AGENCY NAME & ADDRESS*(if different from Controlling Office)*		15. SECURITY CLASS. *(of this report)*
		15a. DECLASSIFICATION/DOWNGRADING SCHEDULE

16. DISTRIBUTION STATEMENT *(of this Report)*

Approved for Public Release, Distribution Unlimited

17. DISTRIBUTION STATEMENT *(of the abstract entered in Block 20, if different from Report)*

18. SUPPLEMENTARY NOTES

19. KEY WORDS *(Continue on reverse side if necessary and identify by block number)*
beamforming, coherent crosscorrelation, geophone array, hydrophone array, polarization filtering, seismic propagation modeling, shallow water sound, signal processing gains, spectral analysis

20. ABSTRACT *(Continue on reverse side if necessary and identify by block number)*
This report contains results of an analysis of seismic and hydro-acoustic signals received, at the Naval Coastal Systems Center Stage I array, from a series of shallow water explosions in the Gulf of Mexico. A variety of signal processing techniques were employed to determine the degree of gain realizable, and to charac-terize the received signals and their propagation paths. Techniques included spectral analysis, coherent crosscorrelative velocity filtering, and polarization filtering.

DD FORM 1473 EDITION OF 1 NOV 65 IS OBSOLETE
1 JAN 73

20.   (continued)

cont.

It was found that roughly comparable gains were achieved, using correlation techniques, for both the geophone and the hydrophone signals. The same analysis indicated, however, that the hydrophone signals had relatively larger signal-to-noise ratios than did the geophone signals. Reasonable agreement was obtained, where measurements were possible, between seismic mode propagation speeds as determined by travel time-distance and by coherent correlative beamforming methods.

Certain aspects of the signals, most likely attributable to post-experiment data contamination from an unknown origin, had significant effects on processor performance. For this reason, decisive judgments were not made regarding relative merits of geophones versus hydrophones, in this study.

mfg. 6-77

MATERIAL INSPECTION AND RECEIVING REPORT	1. PROC. INSTRUMENT IDEN(CONTRACT) N00014-80-C-0420	(ORDER) NO.	6. INVOICE NO. DATE	7. PAGE 1	CF 1
				8. ACCEPTANCE POINT D	

2. SHIPMENT NO.	3. DATE SHIPPED	4. B/L	5. DISCOUNT TERMS
ENS0001Z	16JAN81	TCN	N/A .

9. PRIME CONTRACTOR CODE 06359	10. ADMINISTERED BY CODE S2101A
ENSCO, INC. 5408A Port Royal Road Springfield, VA 22151	DCASMA - Baltimore 300 E. Joppa Road Hampton Plaza Bldg., Room 200 Towson, MD 21204

11. SHIPPED FROM (If other than 9) CODE FOB: D	12. PAYMENT WILL BE MADE BY CODE S3910A
	DCASR - Philadelphia P.O. Box 7730 Philadelphia, PA 19101

13. SHIPPED TO CODE 464	14. MARKED FOR CODE
Mr. Robert Obrochta Office of Naval Research 800 N. Quincy Street Arlington, VA 22217	N00014-80-C-0420

15. ITEM NO.	16. STOCK/PART NO. DESCRIPTION (Indicate number of shipping containers · type of container · container number.)	17. QUANTITY SHIP/REC'D *	18. UNIT	19. UNIT PRICE	20. AMOUNT
A002	Final Report	1	EA		

21. PROCUREMENT QUALITY ASSURANCE		22. RECEIVER'S USE
A. ORIGIN ☐ PQA ☐ ACCEPTANCE of listed items has been made by me or under my supervision and they conform to contract, except as noted herein or on supporting documents.	B. DESTINATION ☐ PQA ☐ ACCEPTANCE of listed items has been made by me or under my supervision and they conform to contract, except as noted herein or on supporting documents.	Quantities shown in column 17 were received in apparent good condition except as noted.
		DATE RECEIVED SIGNATURE OF AUTH GOVT REP TYPED NAME AND OFFICE
DATE SIGNATURE OF AUTH GOVT REP TYPED NAME AND OFFICE	DATE SIGNATURE OF AUTH GOVT REP TYPED NAME AND TITLE	* If quantity received by the Government is the same as quantity shipped, indicate by (✓) mark, if different, enter actual quantity received below quantity shipped and encircle.

23. CONTRACTOR USE ONLY

ACKNOWLEDGEMENT

TABLE OF CONTENTS

LIST OF FIGURES

LIST OF FIGURES (cont'd)

LIST OF FIGURES (cont'd)

LIST OF FIGURES (cont'd)

LIST OF FIGURES (cont'd)

LIST OF FIGURES (cont'd)

LIST OF TABLES

1.0 INTRODUCTION

The puapose of this work was to analyze seismic-hydro-acoustic signals recorded, at an ocean bottom geophone/hydrophone array, during a shallow-water explosive shot experiment conducted by the Naval Coastal Systems Center. This analysis was to employ a variety of special signal processing techniques, in order to determine the degree of processing gain realizable and to characterize the received signals and their propagation paths.

In the experiment, charges having the equivalent of .8 pounds TNT were exploded at different ranges along a 110 km southwesterly radial leg, from the Naval Coastal Systems Center Stage I array located in the Gulf of Mexico near Panama City, Florida. Signals from the shots were received and tape recorded at the array, which contained seven tri-axial geophones and six hydrophones deployed along three radii. Array configuration is defined in Figure 1a and Table 1. All geophones were buried about .3 meters deep in the ocean bottom; all hydrophones were suspended about .6 meters above the bottom. Water depth was approximately 30 meters at the array, gradually increasing to about 40 meters at range 25 kilometers. Further out, the bottom slope was about .8 meters downward per kilometer.

Thirty events were digitized, representing shot ranges from 3.73 to 108.89 kilometers. An analysis was made of these digital time series, using reduced travel time-distance plots, concentrating on the high signal-to-noise events within 30 kilometers of the array. From this analysis, a preliminary seismic propagation model was established to explain the observed mode structure. A subset of these events was then

ENSCO, Inc.   - 1 -

• = Tri-axial geophone
○ = Hydrophone

Geophone Axes

Shot Direction
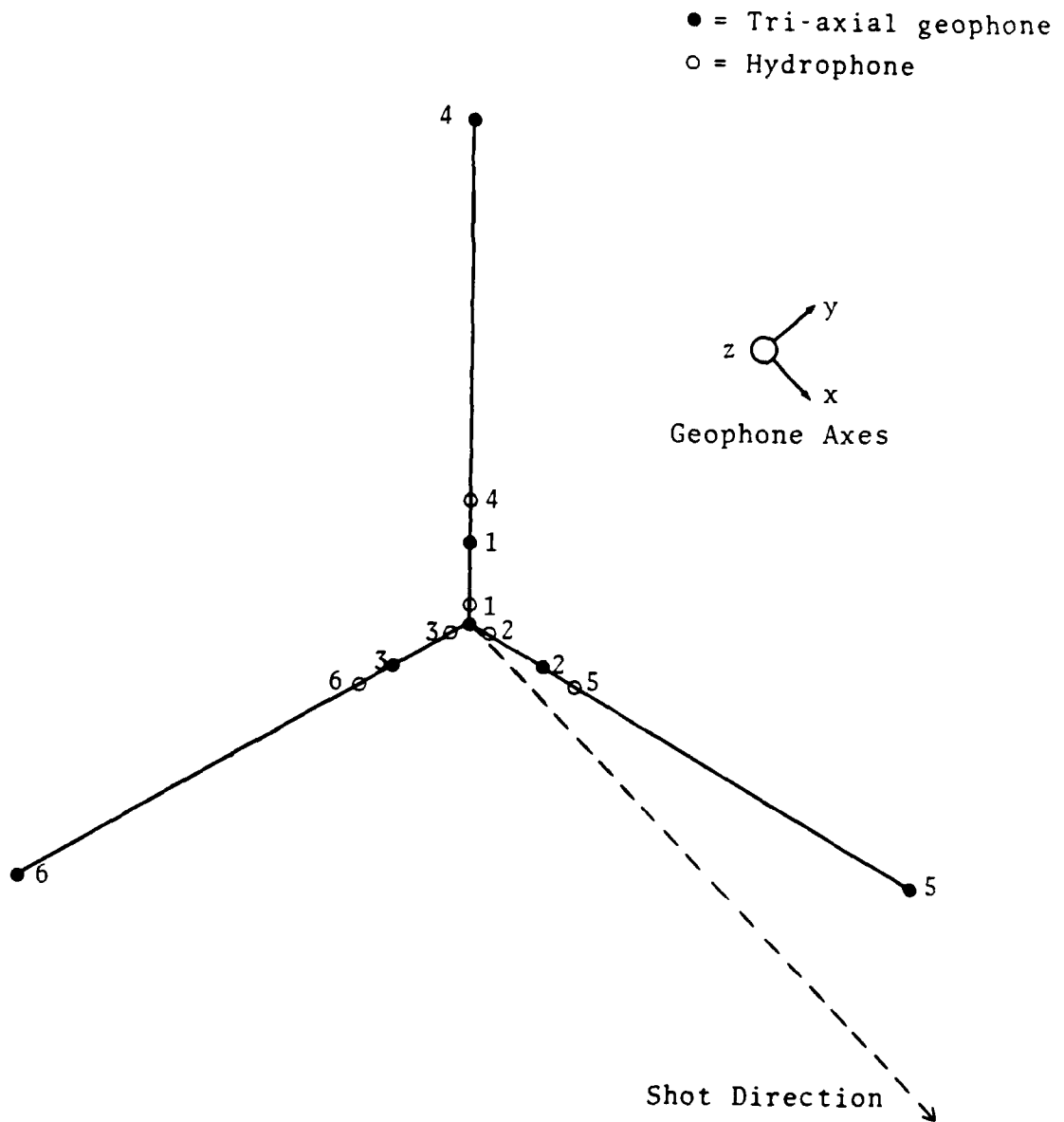
Figure 1a   Stage I Array Configuration (From Reference 1)
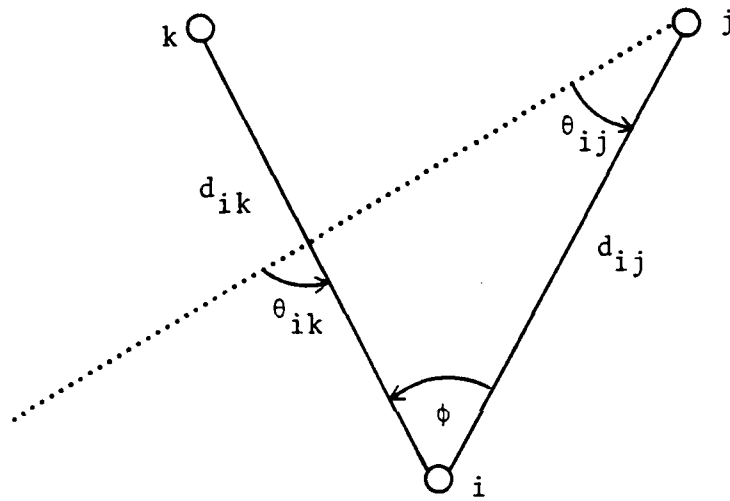
Figure 1b Correlation Array Geometry

TABLE 1

SENSOR DISPLACEMENTS

Sensor	Distance from Array Center (meters)
H_1	.635
H_2	.457
H_3	.762
H_4	8.839
H_5	8.966
H_6	9.322
G_1	6.045
G_2	5.893
G_3	6.121
G_4	35.408
G_5	34.925
G_6	35.408
G_7	0.000

(From Reference 1)

subjected to intensive signal processing, including time series and spectral analysis, coherent crosscorrelation and beamforming, and polarization filtering.

Substantial signal-to-noise ratio (SNR) gains were achieved by use of the coherent crosscorrelation techniques, although certain attributes of this digitized data set may be unrepresentative of typically encountered signals. In particular, a very highly correlated, but apparently unphysical, signal was found to contaminate the data set. It is not clear to ENSCO what the source of this artifact might have been. Application of polarization filters yielded generally unusable or untenable results, even though the signals clearly should have been, at least partially, susceptible to this processing. A possibility exists that the transfer of code and modification of (previously successful) poliarization filter algorithms, for the present application, was not made satisfactorily.

Both seismometer and hydrophone-received signals were analyzed as part of this investigation. In spite of the fact that the hydrophones had a much smaller array baseline than did the geophones, calculations implied the hydrophones might serve as a better sensor for detection and measurement of shallow water events, at least for ranges closer than 20 kilometers. This conclusion would remain valid here, even allowing for potential improvements in geophone SNR expected to be achievable with proper poliarization filtering. However, this judgment must be weighed in view of the markedly different transfer functions of the two types of sensors and of the fact that both sensor signals were processed at the same bandwidth. It should also be cautioned that, owing to the relatively small hydrophone array baseline, the hydrophone-derived SNR and correlation/beamforming gain are subject to large uncertainties.

2.0 ANALYSIS

The investigation discussed in this section was conducted in four phases. During the first phase, digital representations of the shot signals were graphically analyzed in order to develop a preliminary description of the seismic propagation environment. Four different shots were selected for further processing. In the second phase, these selected shots were subjected to time series and spectral analysis, to determine their temporal and spectral content. In the third phase, the selected signals were analyzed by means of coherent crosscorrelation processing to enable event mode detection and isolation, and measurement of mode propagation direction (coherent beamforming) and speed. Estimates were obtained for input mode SNR's and correlation processing gain. Equivalent processing was then performed on polarization filtered time series, in the fourth phase.

2.1 Seismic Modeling

Low resolution digital time series displays of the geophone and hydrophone signals were used to assemble a reduced travel-time versus distance plot for all the shots listed in Table 2. Truncated versions of these plots are presented in Figures 2 through 7. All even numbered Figures contain signals only from shots exploded on the ocean bottom. Odd numbered Figures contain signals only from shots exploded at mid-depth (about 20 m).

Seismic mode trajectories were identified, wherever possible, and measured from the time-distance plots. The Figures show these trajectories, superimposed on the time

TABLE 2
SHOT DESCRIPTIONS

Shot	Distance from Array (km)	Location	Shot	Distance from Array (km)	Location
A1	108.89	M	A16	14.96	B
A2	109.04	M	A17	11.17	M
A3	109.13	M	A18	11.24	B
A4	101.96	M	A19	9.28	M
A5	92.38	M	A20	9.27	B
A6	83.36	M	A21	8.85	B
A7	73.67	M	A22	8.26	B
A8	64.89	M	A23	7.79	B
A9	55.85	M	A24	7.37	B
A10	46.37	M	A25	6.93	B
A11	36.89	M	A26	6.48	B
A12	27.84	M	A27	6.03	B
A13	18.44	M	A28	5.64	B
A14	18.27	B	A30	4.53	B
A15	14.88	M	A32	3.73	B

M = mid-depth ($\sim$18m)

B = bottom ($\sim$40m)

(From Reference 1)

ENSCO, Inc.   - 7 -
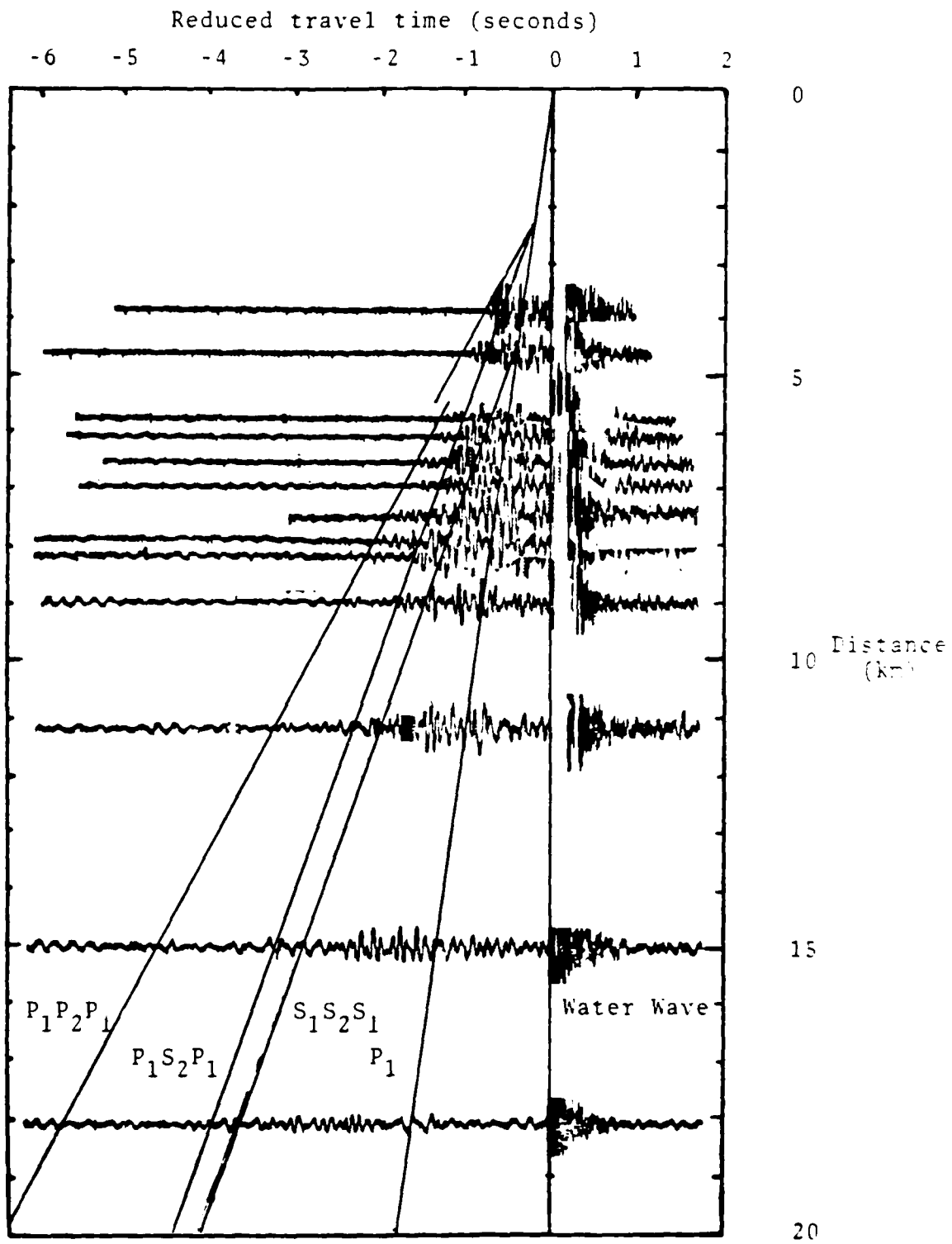
Figure 2 Reduced Travel Time-Distance Plot,
Geophone 3X (Bottom Shots)
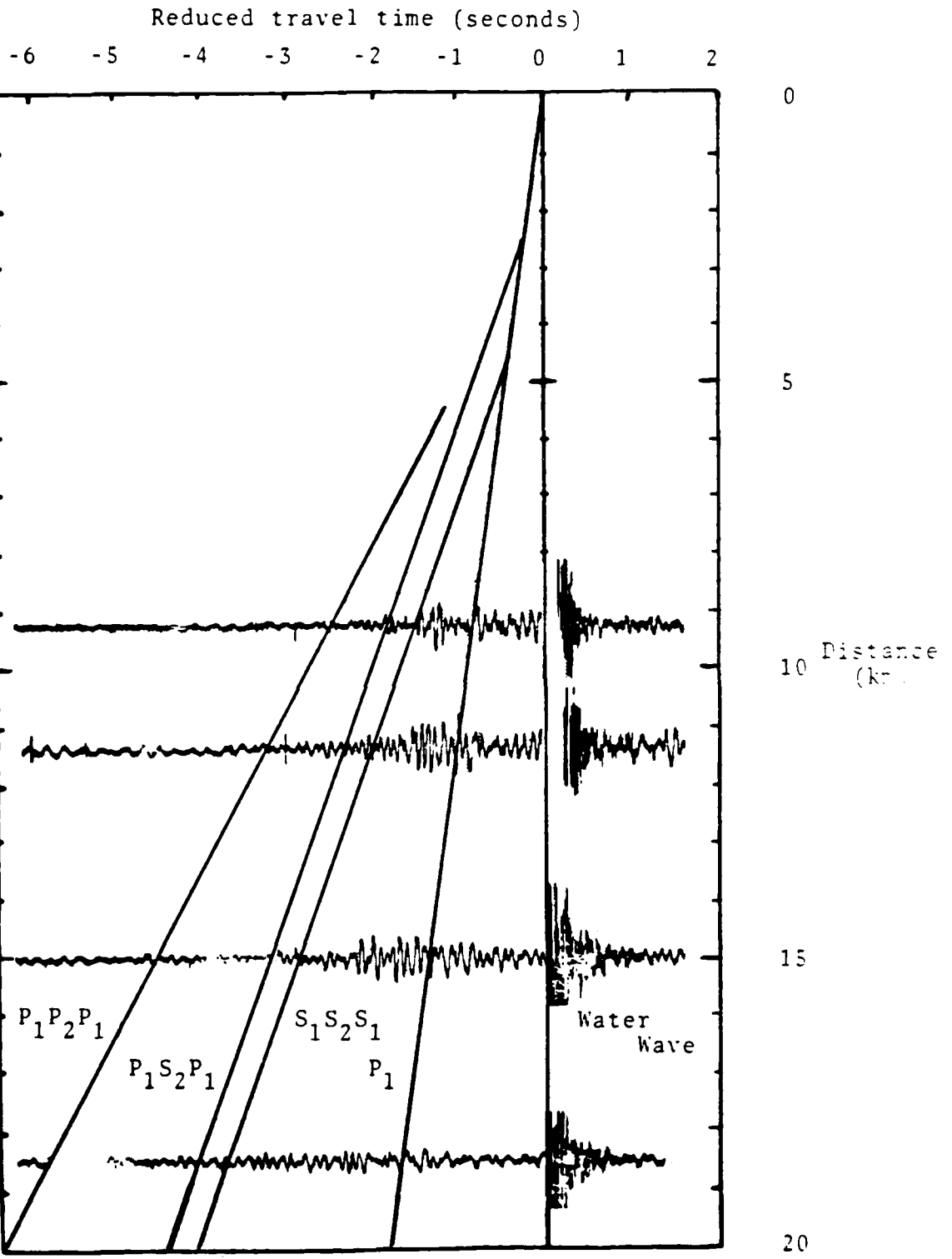
Figure 3   Reduced Travel Time-Distance Plot,
Geophone 3X (Mid-depth Shots)

Reduced travel time (seconds)
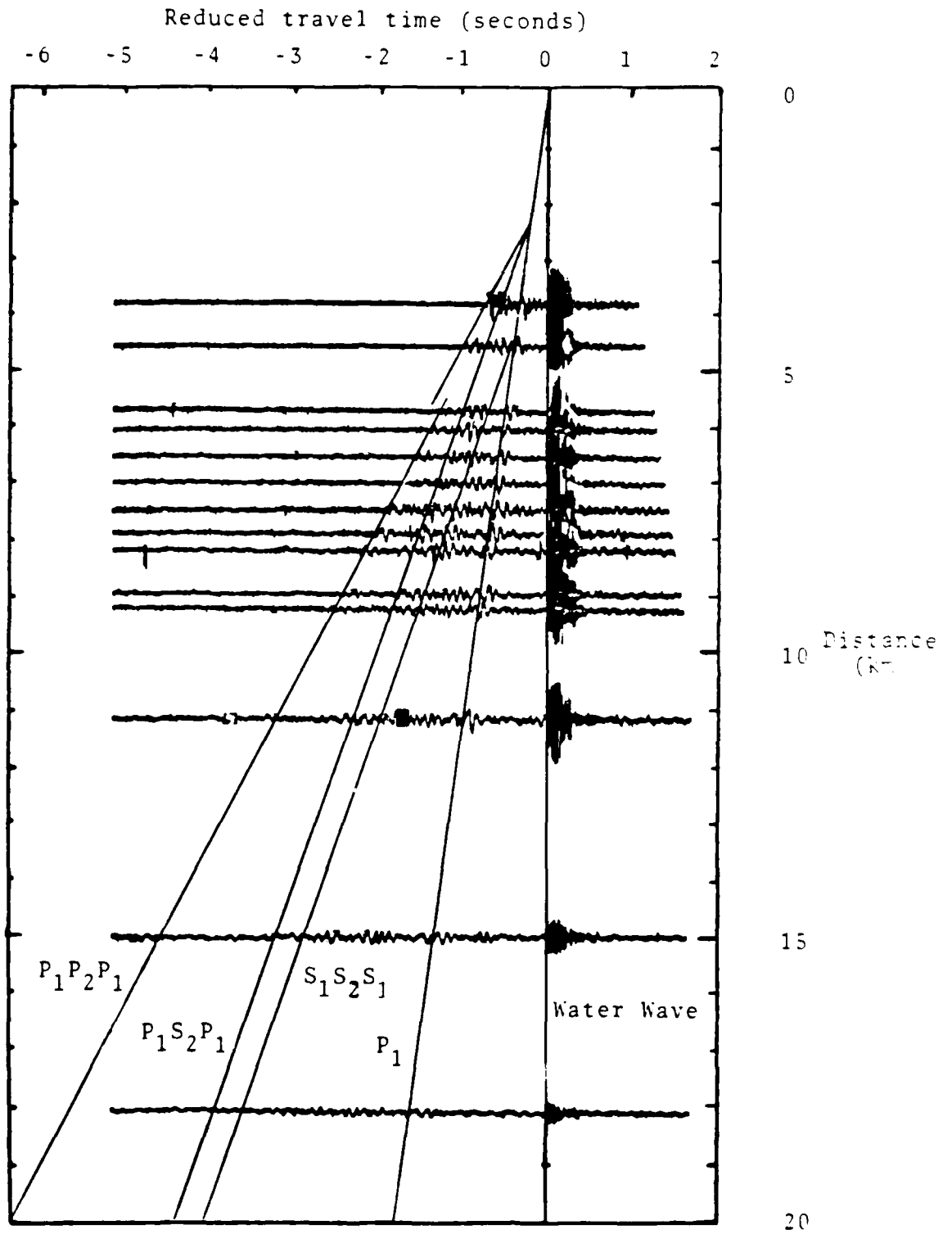
Figure 4   Reduced Travel Time-Distance Plot,
Geophone 3Z (Bottom Shots)
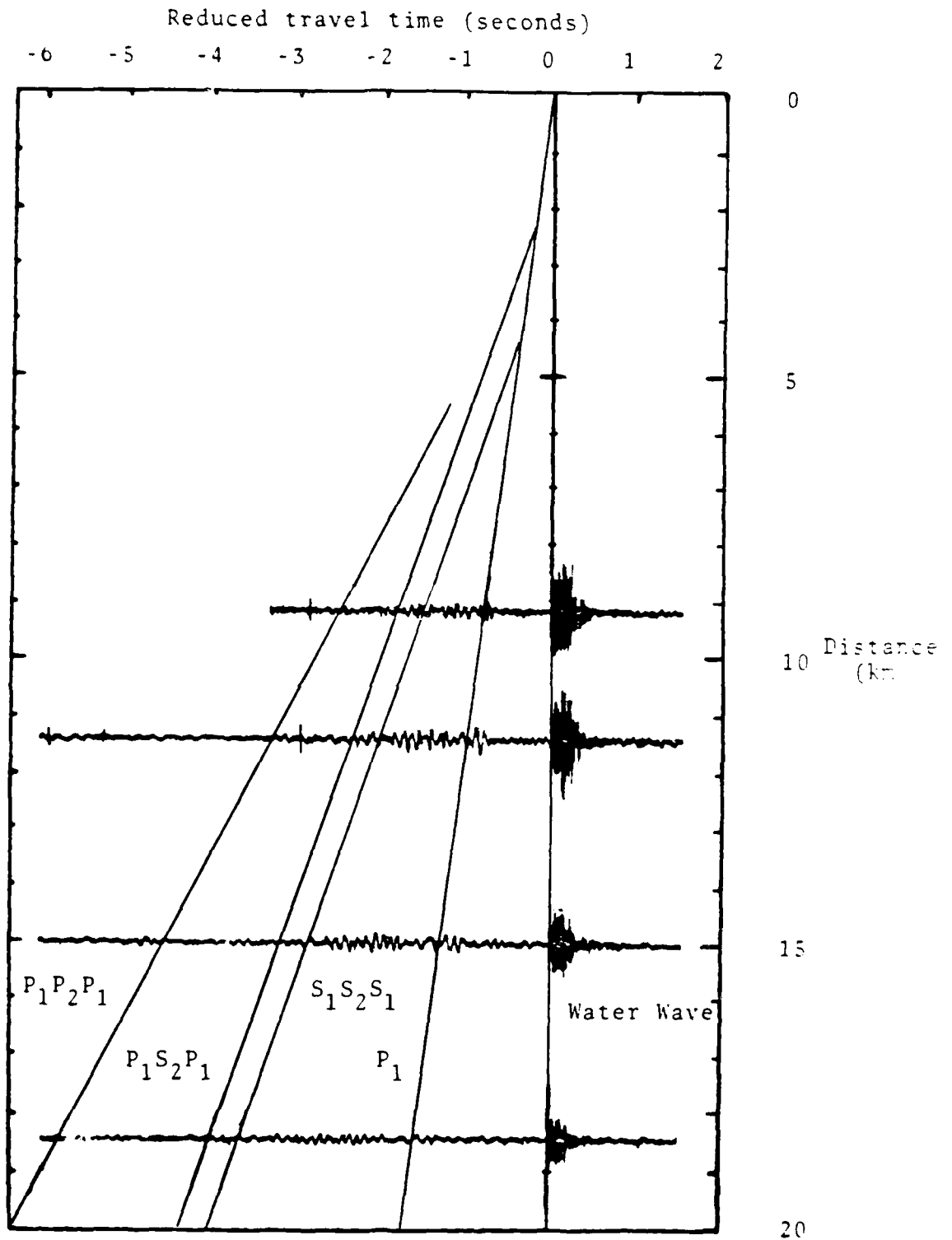
Figure 5 Reduced Travel-Time-Distance Plot, Geophone 3Z (Mid-depth Shots)
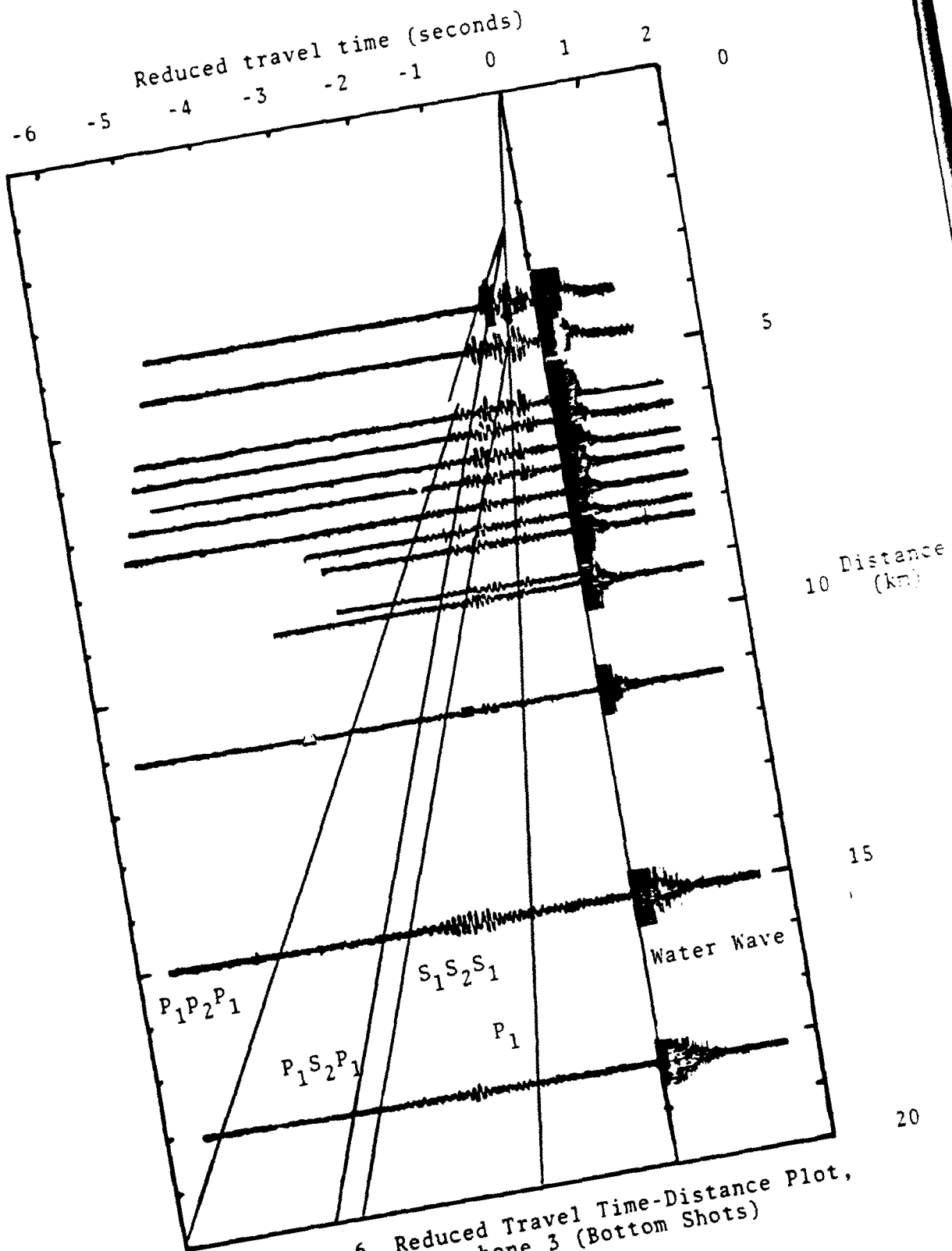
Figure 6   Reduced Travel Time-Distance Plot, Hydrophone 3 (Bottom Shots)

- 12 -

ENSCO, Inc.

Reduced travel time (seconds)
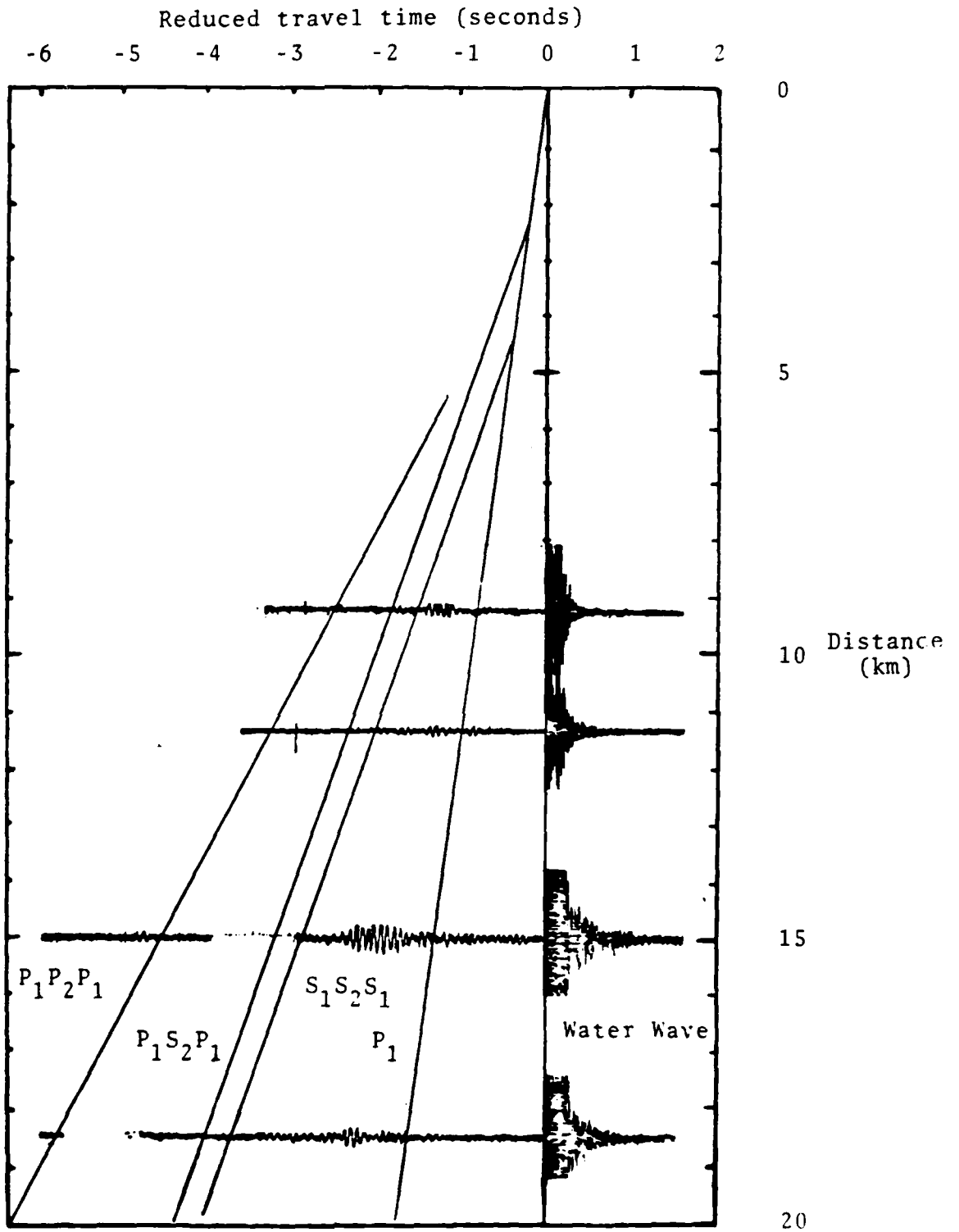
Figure 7   Reduced Travel Time-Distance Plot,
Hydrophone 3 (Mid-Depth Shots)

series displays. A two-layer model was then developed to accommodate the observations. Equations necessary to computation of the seismic model parameters are discussed below.

Propagation time, t_a, for a mode which travels in a uniform layer is

$$t_a = \frac{R}{c_a} \tag{1}$$

where R is the range from source to receiver. Propagation time, t_{afa}, for a mode which traverses from the top of the first layer, critically refracts into a second layer, then refracts back through the first layer, is

$$t_{afa} = 2 \frac{h}{c_a} \sqrt{1 - \frac{c_a^2}{c_f^2}} + \frac{R}{c_f} \tag{2}$$

where h is the first layer thickness; c_a is the mode speed in the first layer; c_b is the mode speed in the second layer. Arrival time difference, $\Delta t(a, afa)$, between the modes described by equations (1) and (2), is

$$\Delta t(a,\ afa) = R\left(\frac{1}{c_a} - \frac{1}{c_f}\right) - 2 \frac{h}{c_a} \sqrt{1 - \frac{c_a^2}{c_f^2}} \tag{3}$$

Arrival time difference, $\Delta t(afa,\ aga)$, for two modes traversing as described by equation (2), but having different second layer speeds, c_f and c_g, is

$$\Delta t(afa, aga) = 2\frac{h}{c_a} \left(\sqrt{1 - \frac{c_a^2}{c_f^2}} - \sqrt{1 - \frac{c_a^2}{c_g^2}} \right)$$

$$+ R\left(\frac{1}{c_f} - \frac{1}{c_g}\right) \tag{4}$$

Finally, the arrival time difference, $\Delta t(afa,bfb)$, for the two modes traveling as described by equation (2), but having different first layer speeds, c_a and c_b, is

$$t(afa,bfb) = 2h \left(\frac{1}{c_a} \sqrt{1 - \frac{c_a^2}{c_f^2}} \right.$$

$$\left. - \frac{1}{c_b} \sqrt{1 - \frac{c_b^2}{c_f^2}} \right) \tag{5}$$

It is found, from equations (3), (4) and (5), that

$$\frac{\delta(\Delta t(a,afa))}{\delta R} = \frac{1}{c_a} - \frac{1}{c_f} \tag{3'}$$

$$\frac{\delta(\Delta t(afa,aga))}{\delta R} = \frac{1}{c_f} - \frac{1}{c_g} \tag{4'}$$

$$\frac{\delta(\angle t(afa,bfb))}{\delta R} = 0 \tag{5'}$$

ENSCO, Inc.   - 15 -

Equations (3) and (4) simplify when t = 0, a condition which can be established on time-distance plots by projecting appropriate mode trajectories to their intersection point along the time axis.

Equations (1) through (5) and their derivatives were used to compute seismic propagation speeds and layer thickness, given measurements made from the reduced travel-time versus distance plots. The results of these computations are given in Table 3. It was assumed throughout that the hydroacoustic propagation speed was 1.51 km/sec., as reported in reference 1, from earlier experiments. The upper layer shear speed was deduced indirectly from the arrival time difference between $P_1S_2P_1$ and $S_1S_2S_1$. Evidence is seen for the direct arrival of S_1, especially in the z-axis time traces, but it is not as consistent or obvious as for the other modes. A curious effect is seen wherein the first arrival trajectory for shots A32 and A30 appears delayed about .1 seconds, for the more distant shots. This is as-cribed to a low velocity zone, situated between the upper and lower layers, which must have been encountered for ranges greater than about 5 kilometers. Where possible in the cal-culations, the effects of the low velocity zone were removed. Other, much lower speed, modes were perceived in the nearer shots, but were not able to be analyzed.

High resolution time series displays, shown in Figures 8 through 23, were generated for signals from shots A27, A25, A20, and A14. Note that the waterwave has been clipped to maintain a substantial amplitude dynamic range for the seismic

TABLE 3

DERIVED SEISMIC PROPAGATION PARAMETERS

| Layer | Thickness (km) | Propagation Speed (km/sec) | |
		Compressive	Shear
First	.63 ± .09	1.74 ± .02	1.32 ± .12
Second	--	3.28 ± .16	2.34 ± .06
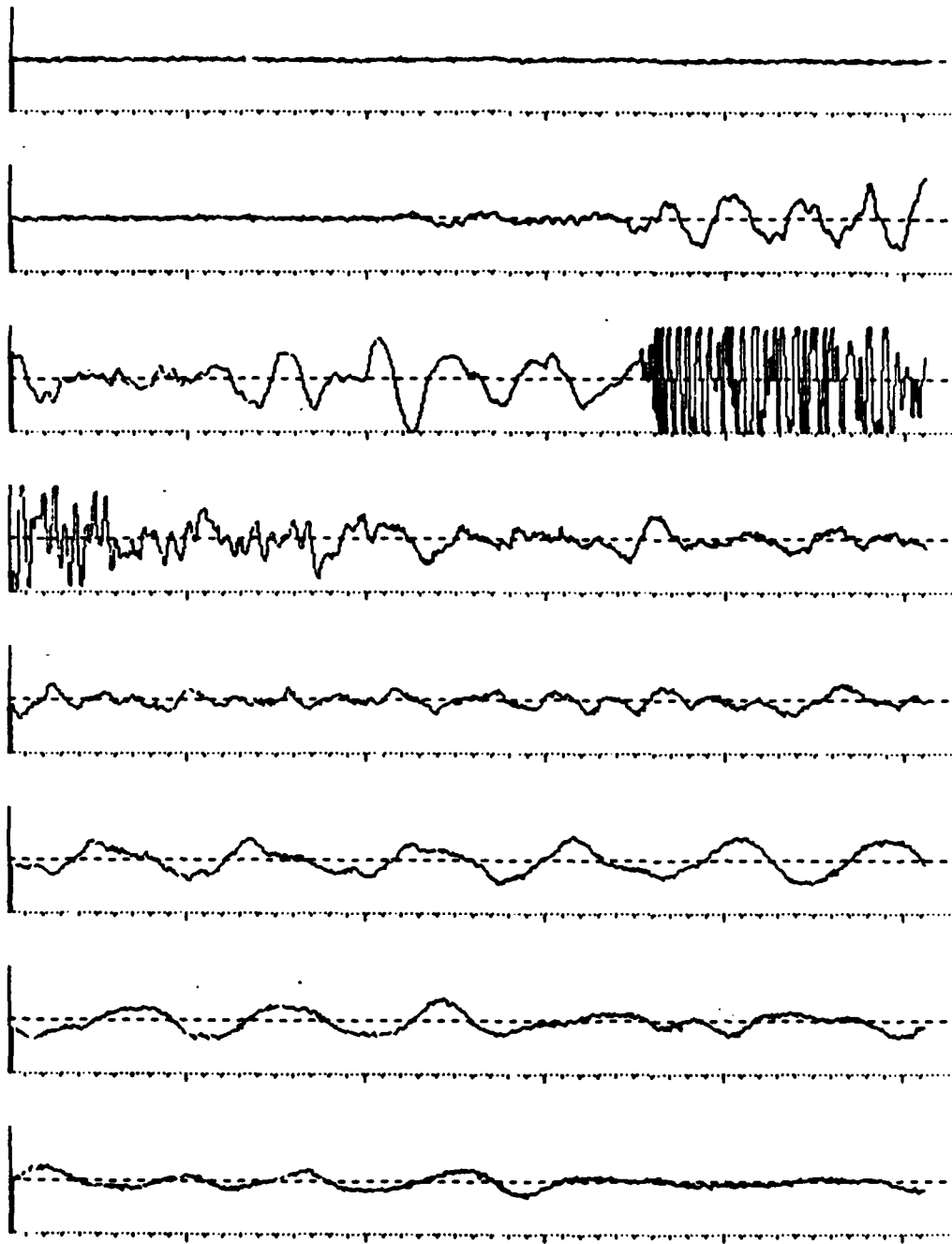
1.024 sec.

Figure 8a   Shot A27, Geophone 5X
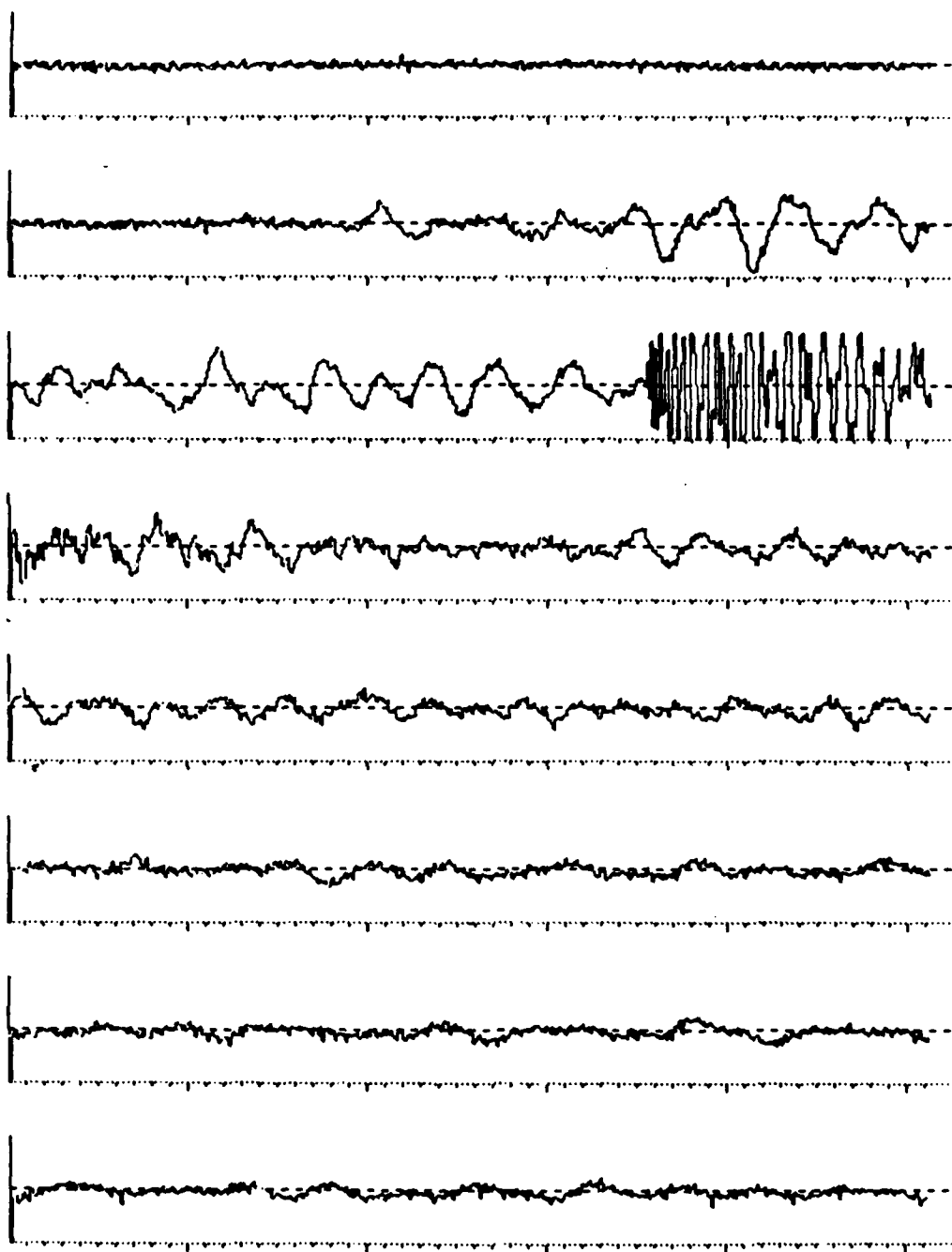
1.024 sec.

Figure 8b Shot A27, Geophone 5Z
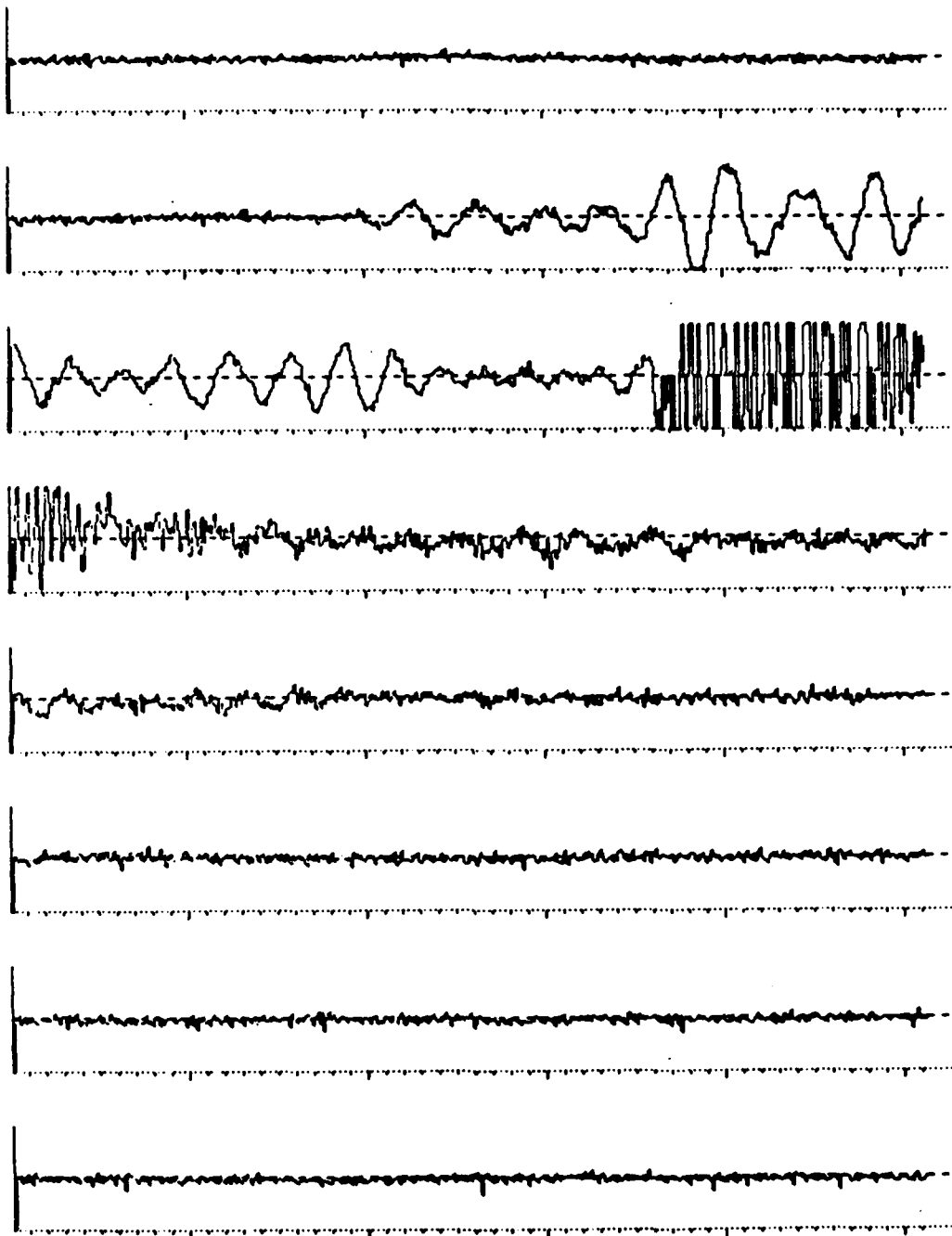
1.024 sec.

Figure 8c   Shot A27, Hydrophone 5
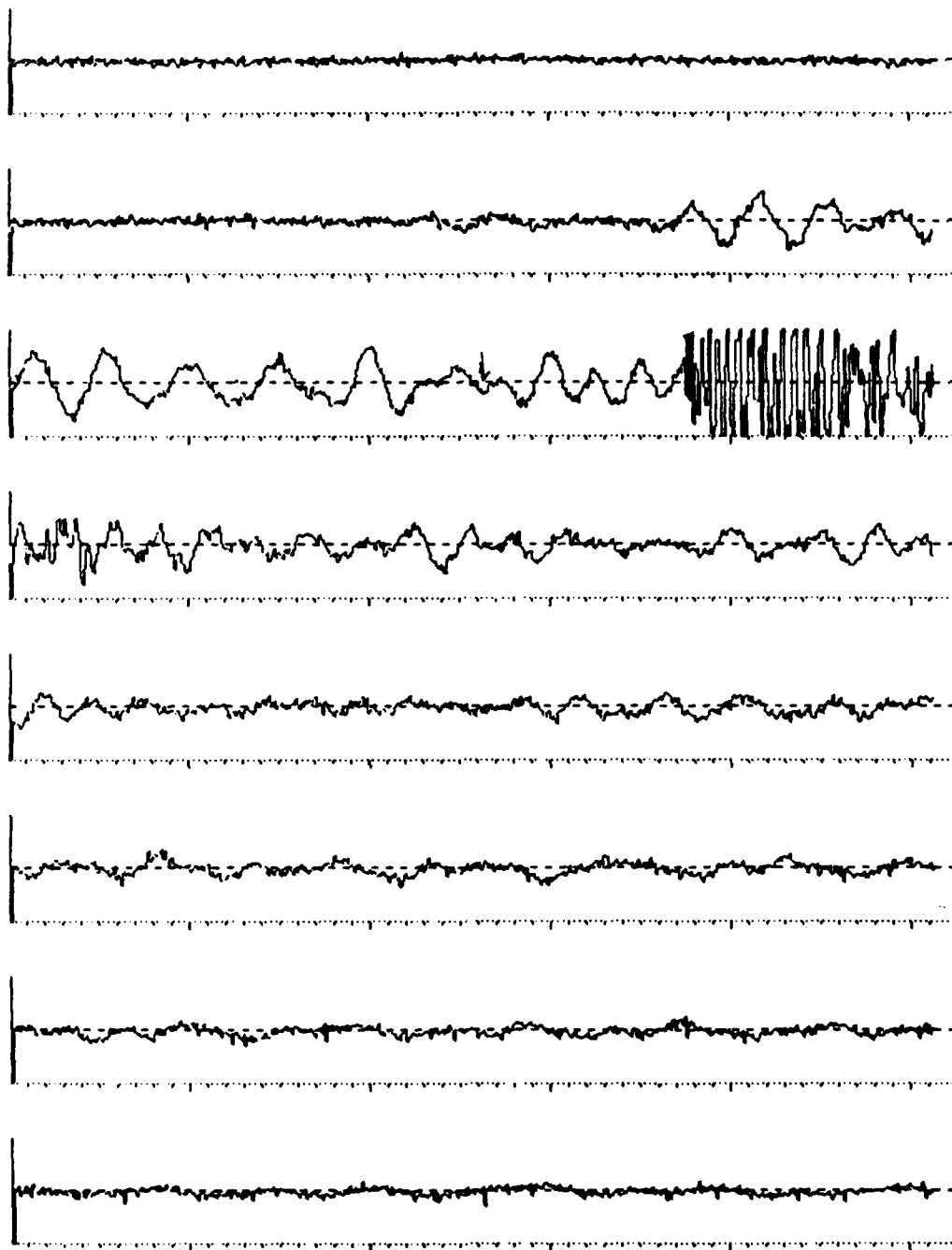
1.024 sec.

Figure 8d   Shot A27, Geophone 4X
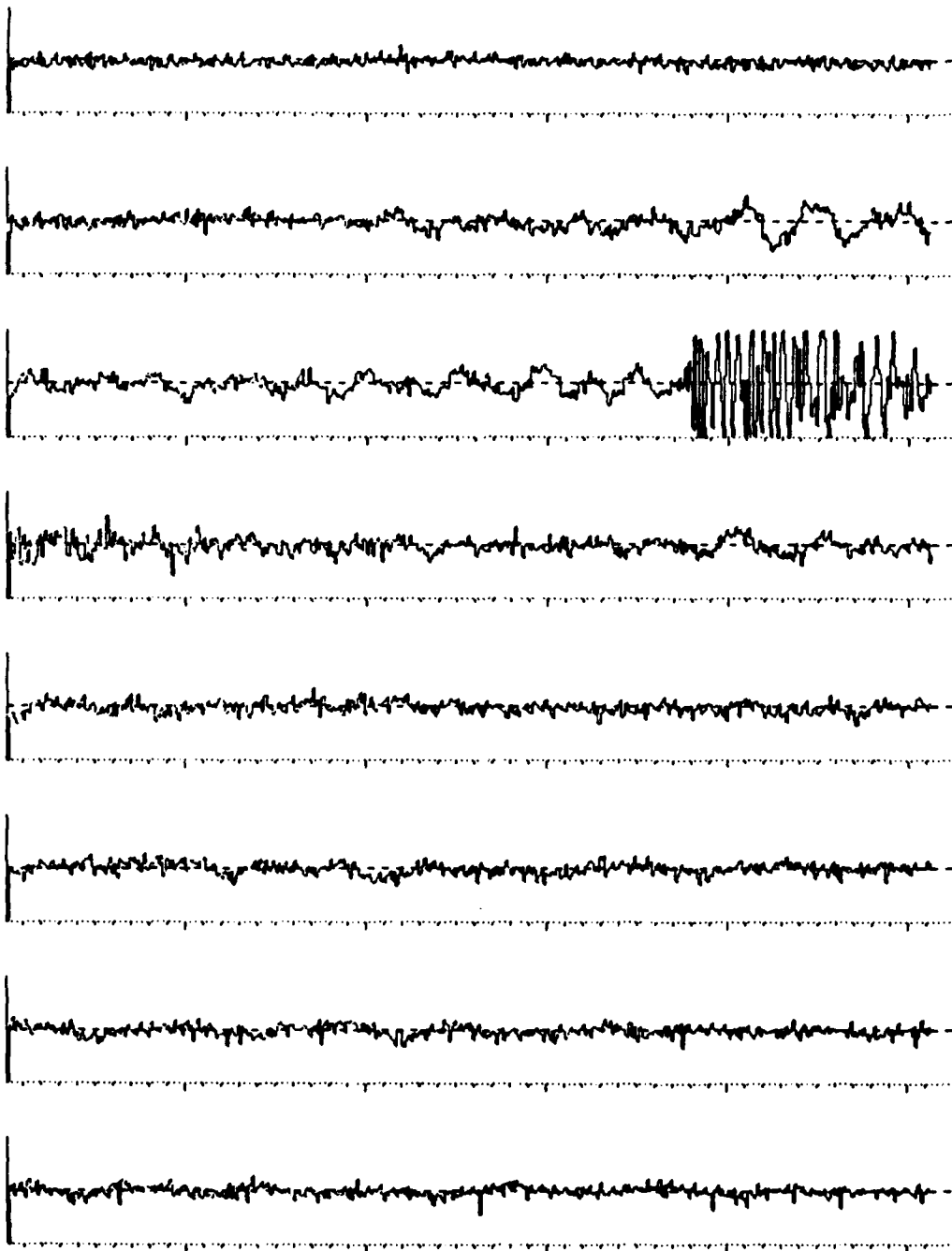
1.024 sec.

Figure 8e   Shot A27, Geophone 4Z
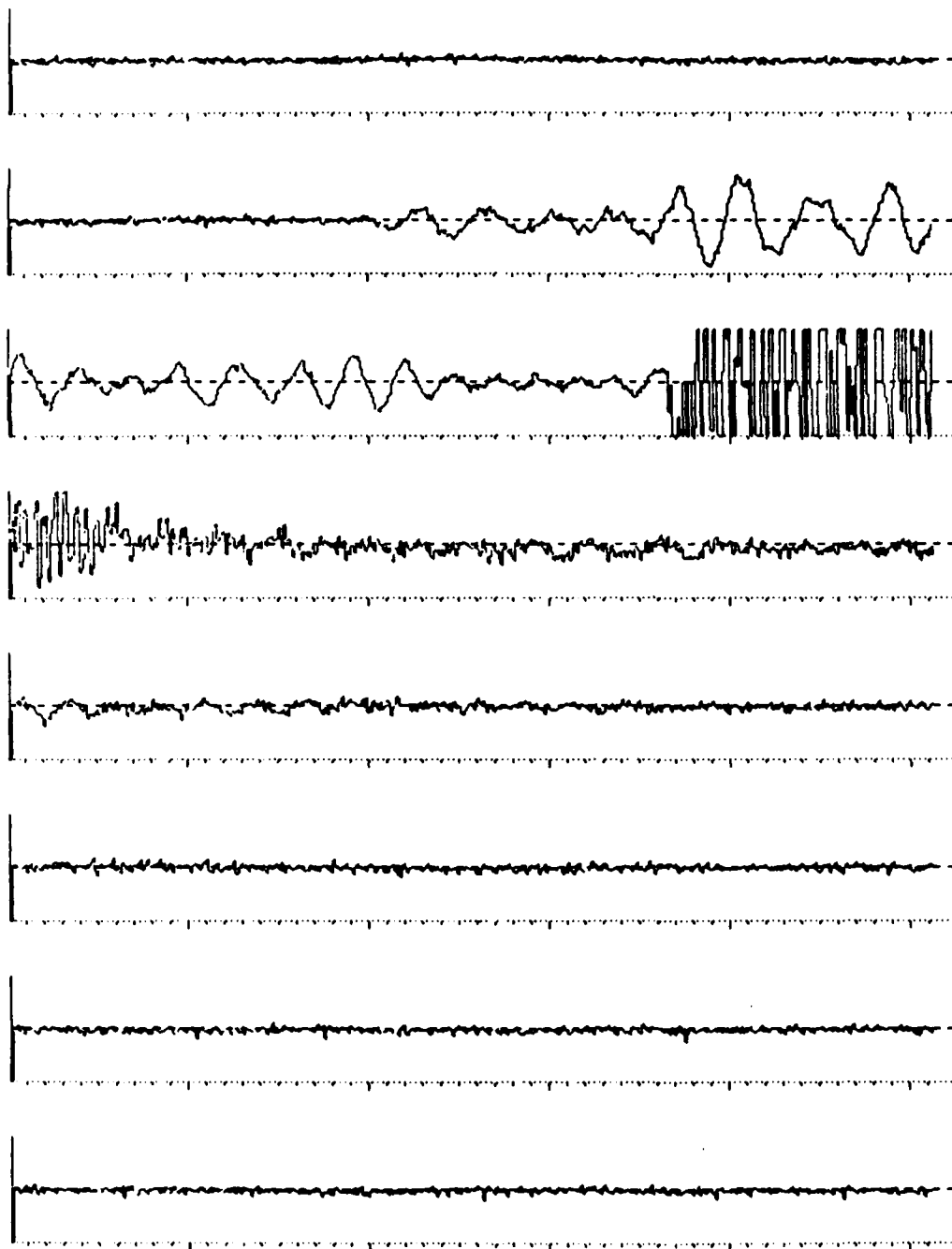
1.024 sec.

Figure 8f Shot A27, Hydrophone 4
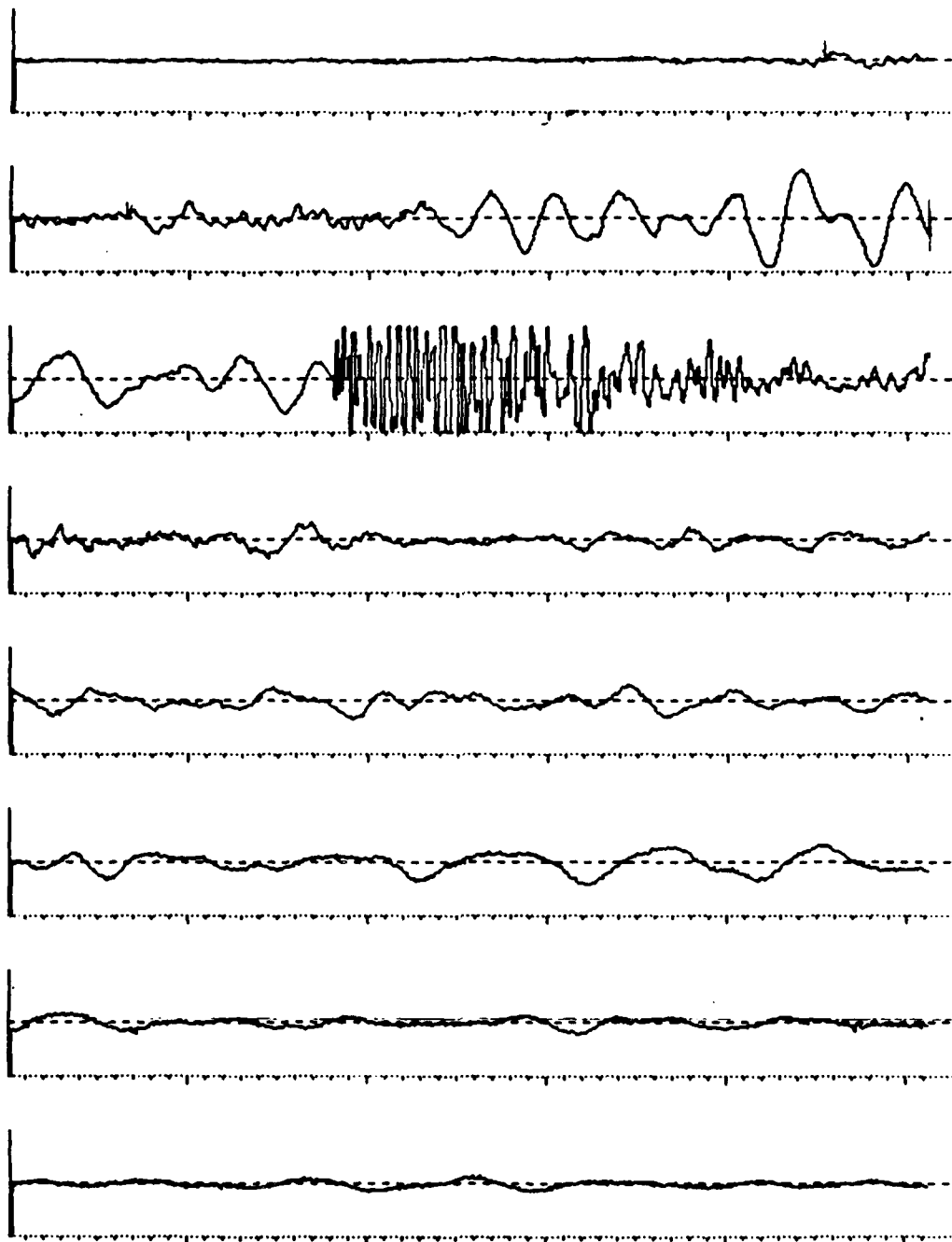
1.024 sec.

Figure 9a   Shot A25, Geophone 5X
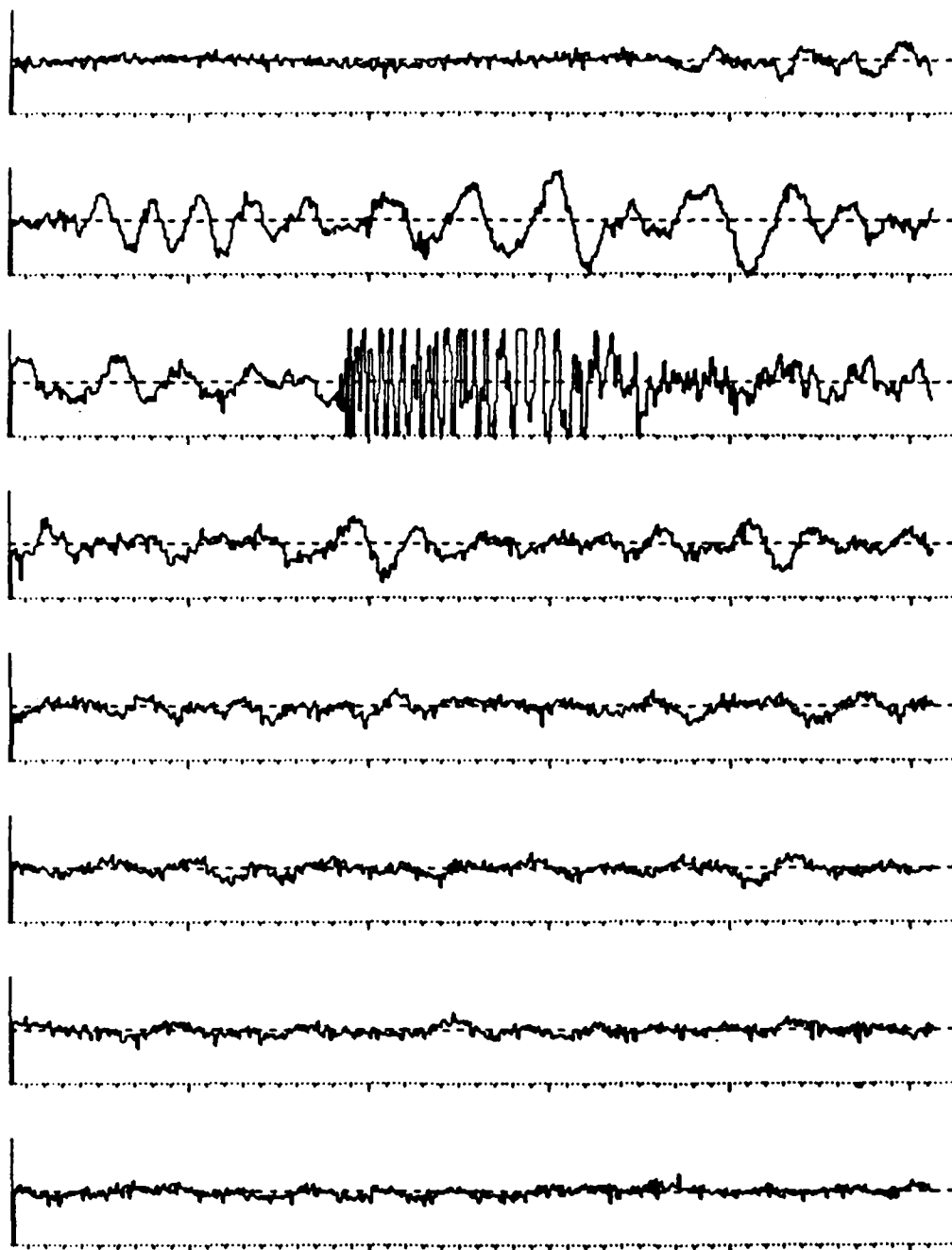
1.024 sec.

Figure 9b   Shot A25, Geophone 5Z
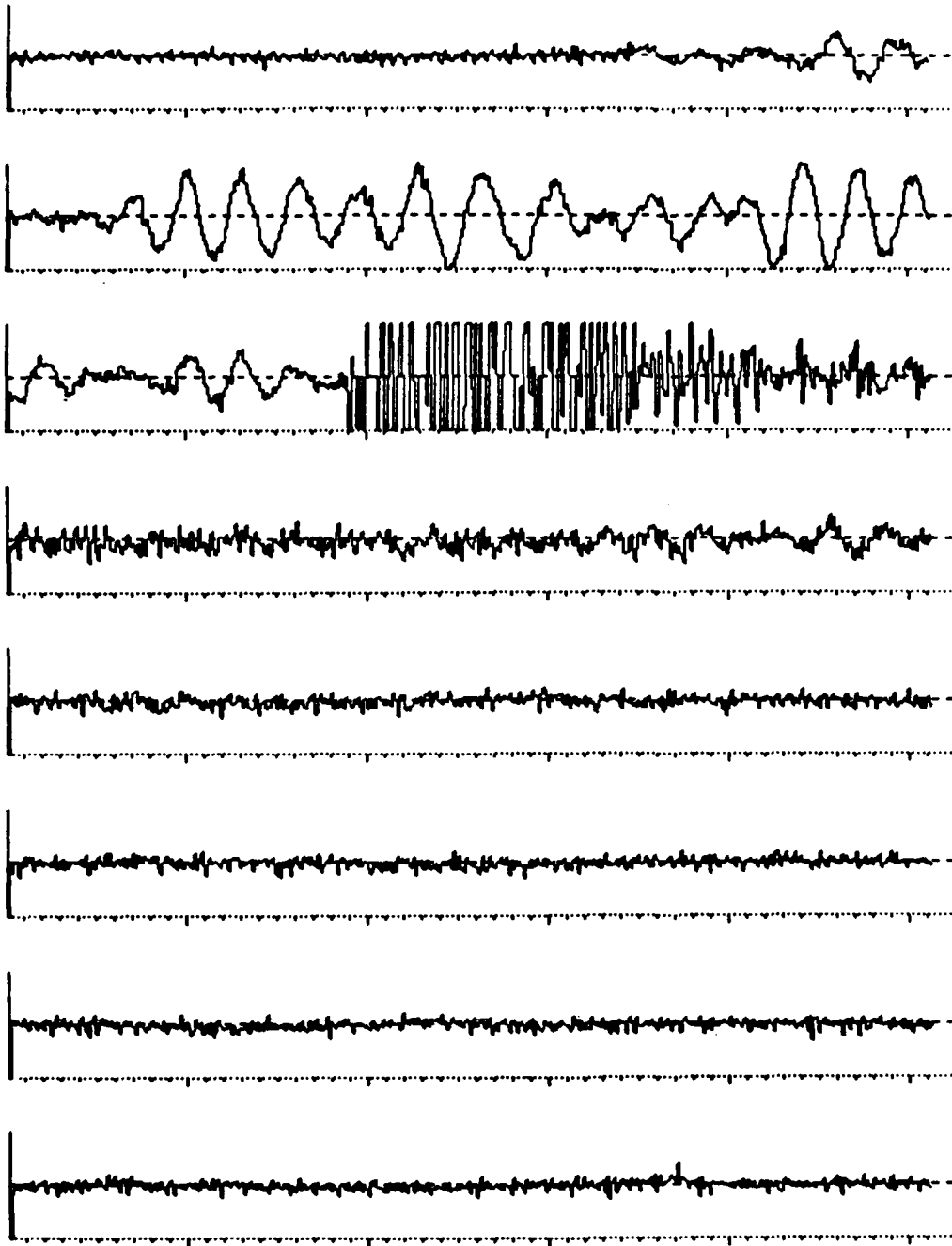
10.24 sec.

Figure 9c   Shot A25, Hydrophone 5
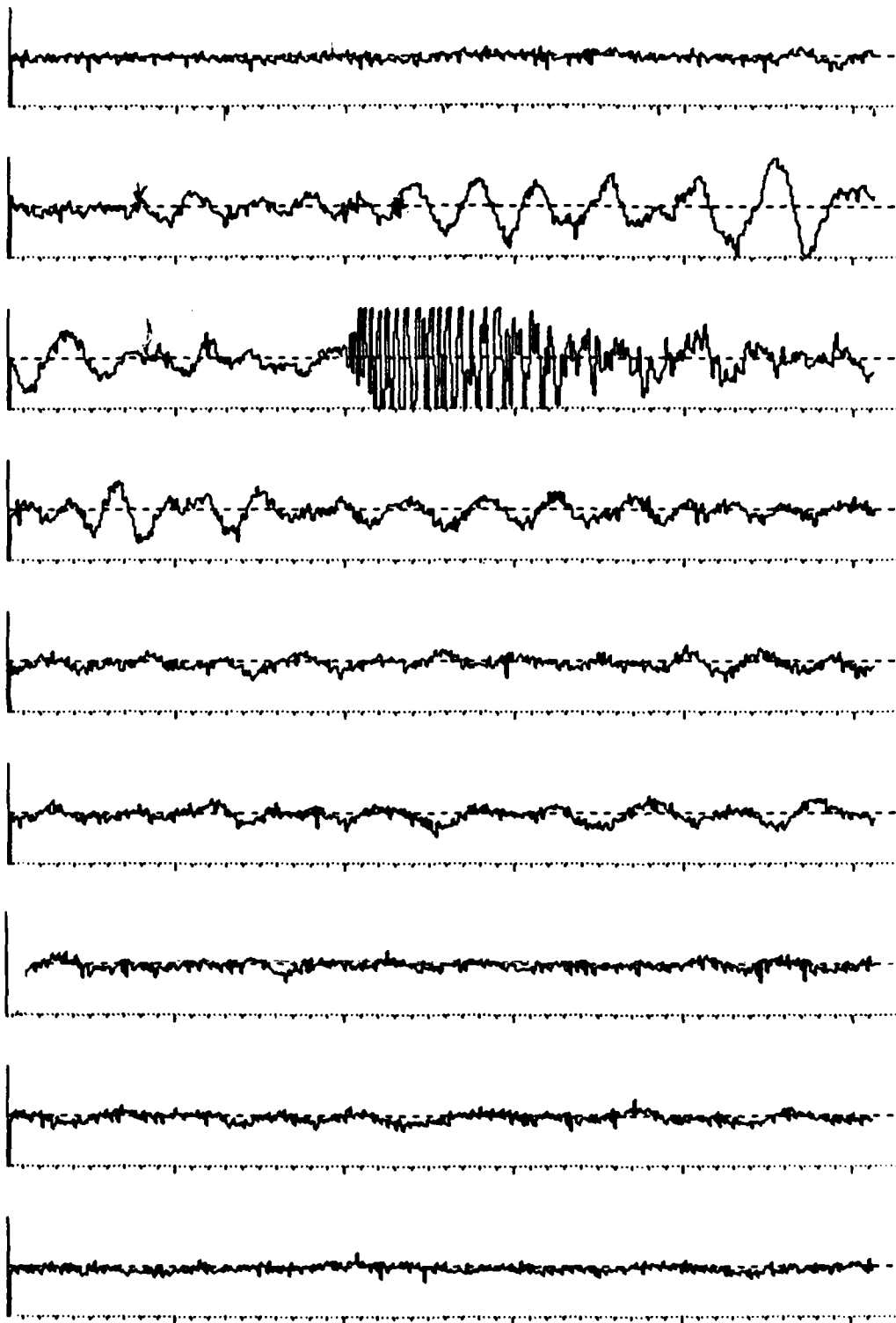
1.024 sec.

Figure 9d   Shot A25, Geophone 4X

ENSCO, Inc.
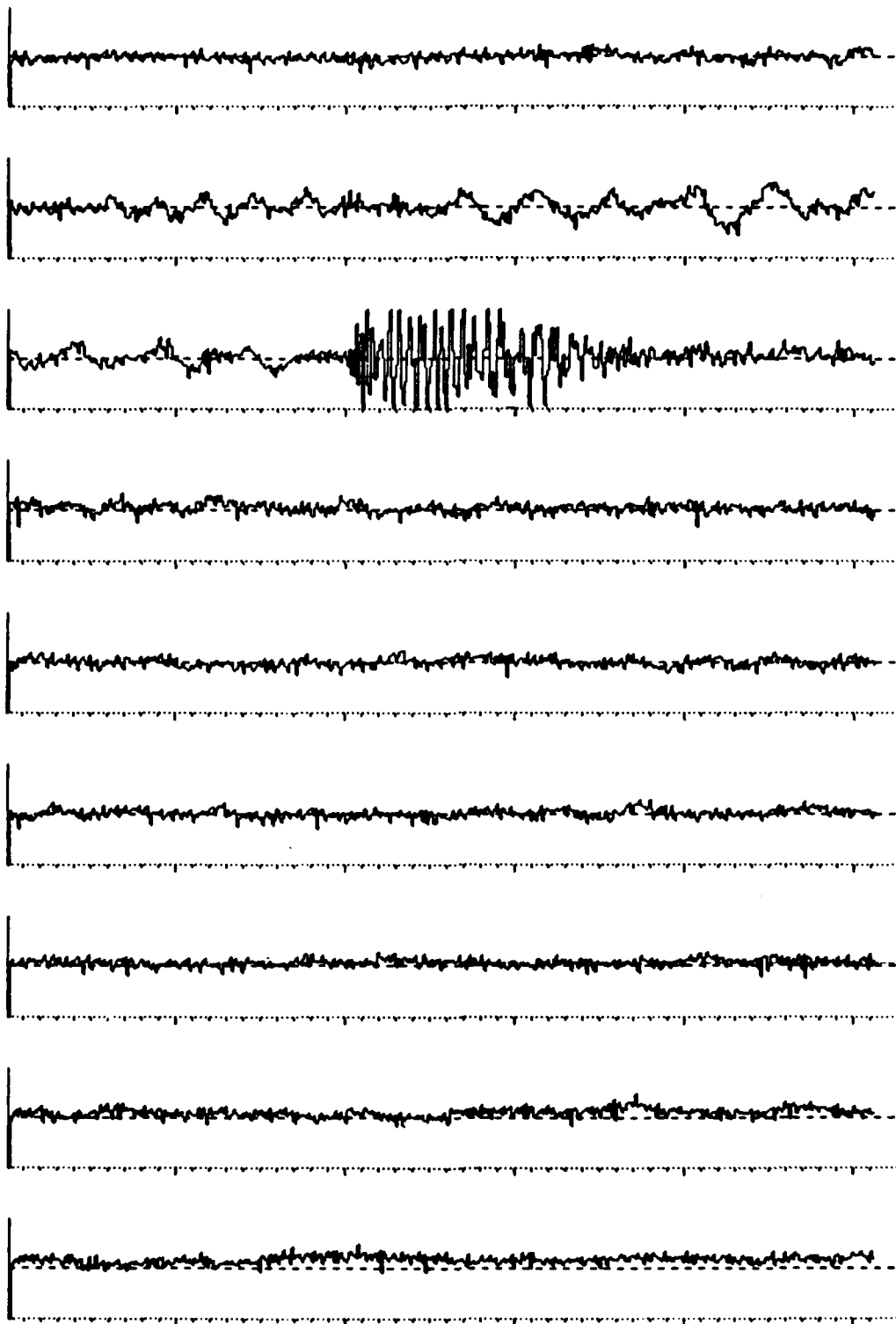
1.024 sec.

Figure 9e   Shot A25, Geophone 4Z
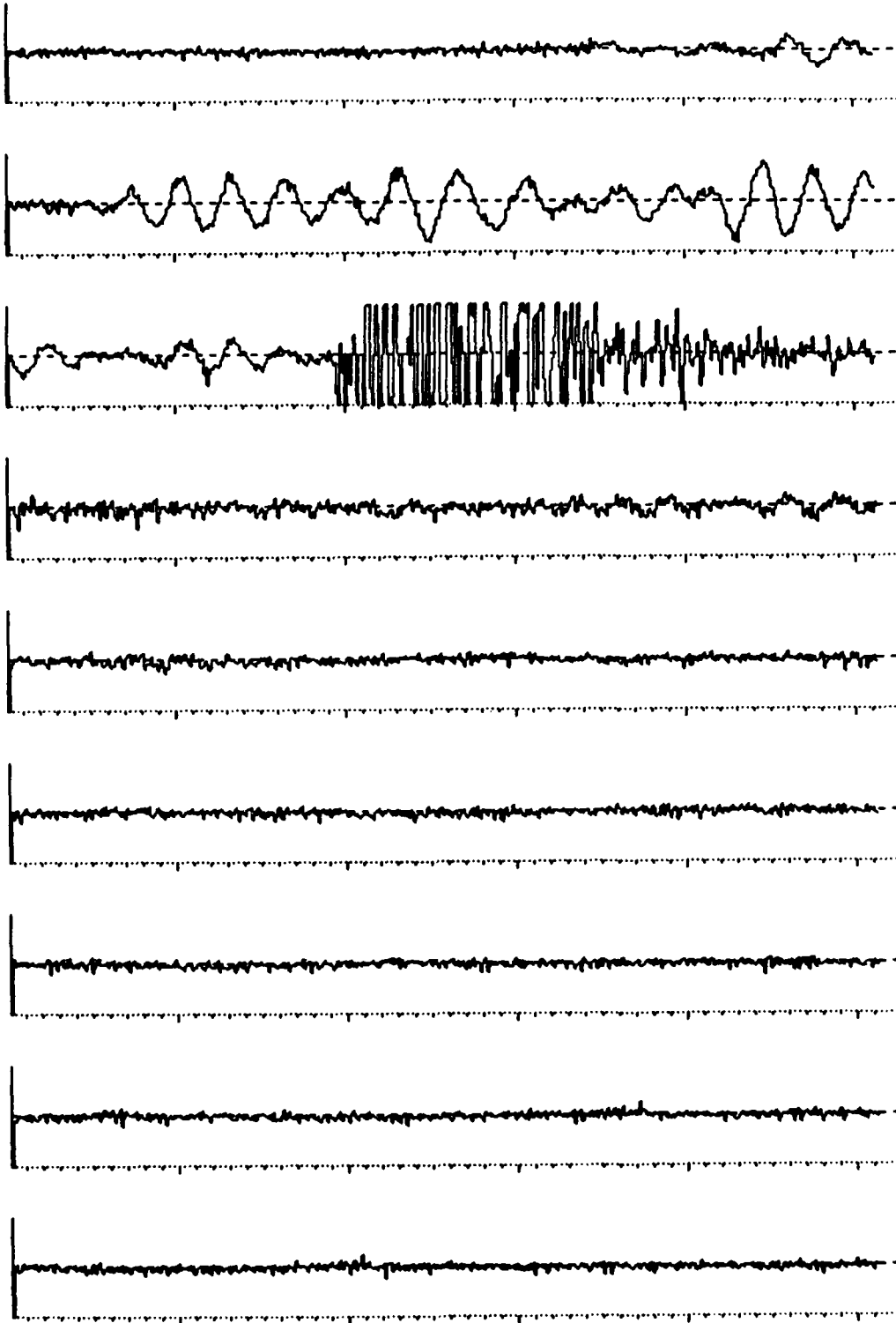
1.024 sec.

Figure 9f   Shot A25, Hydrophone 4
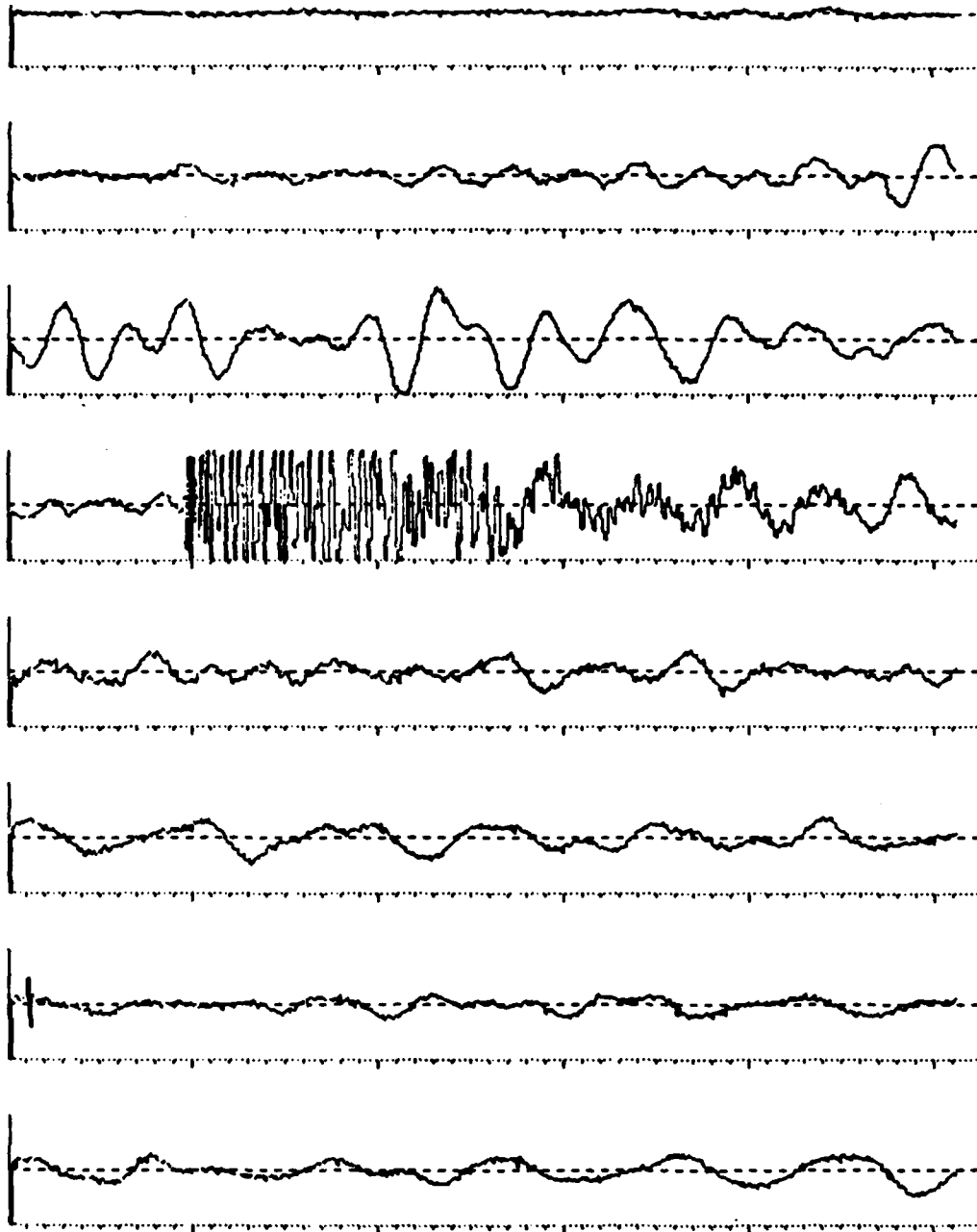
1.024 sec.

Figure 10a   Shot A20, Geophone 5X
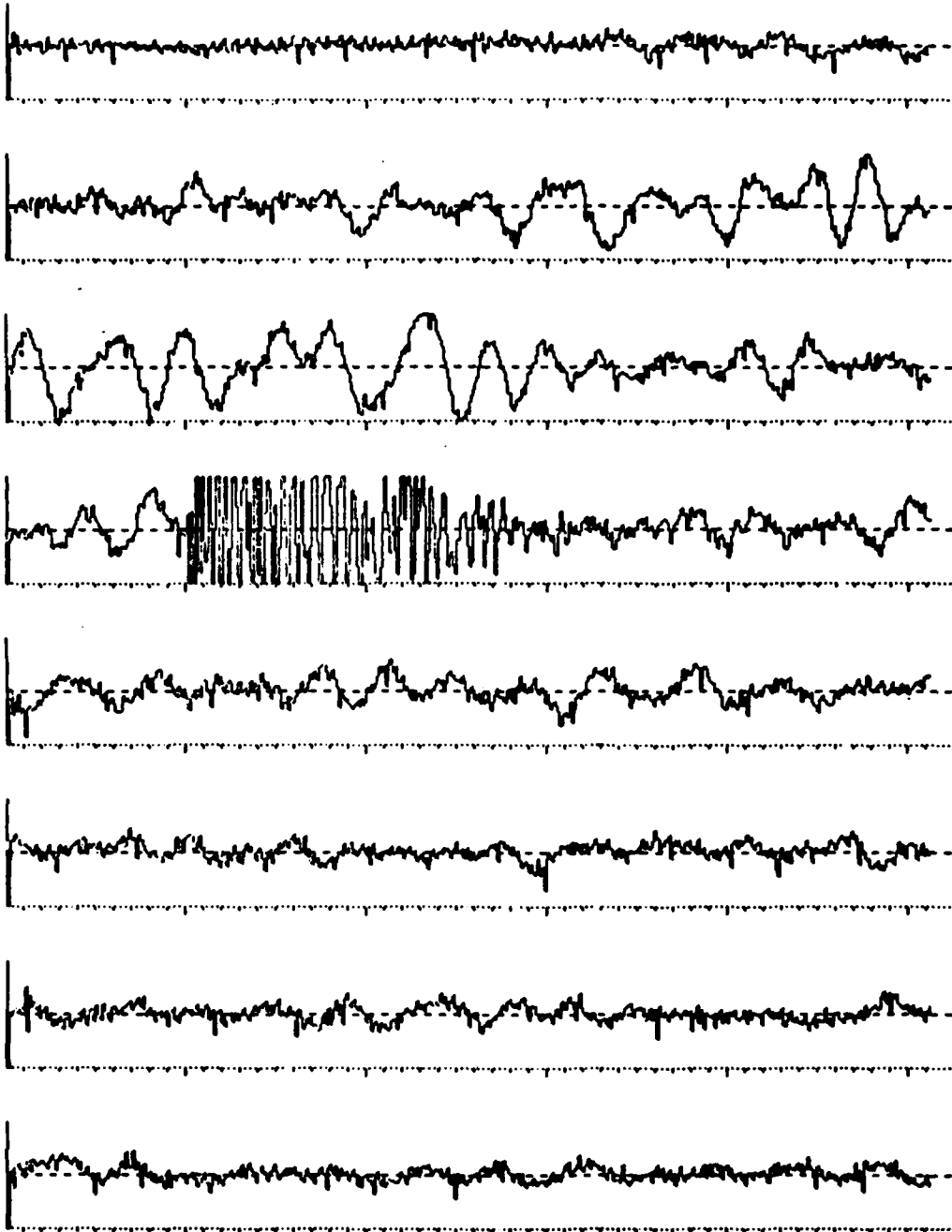
1.024 sec.

Figure 10b   Shot A20, Geophone 5Z
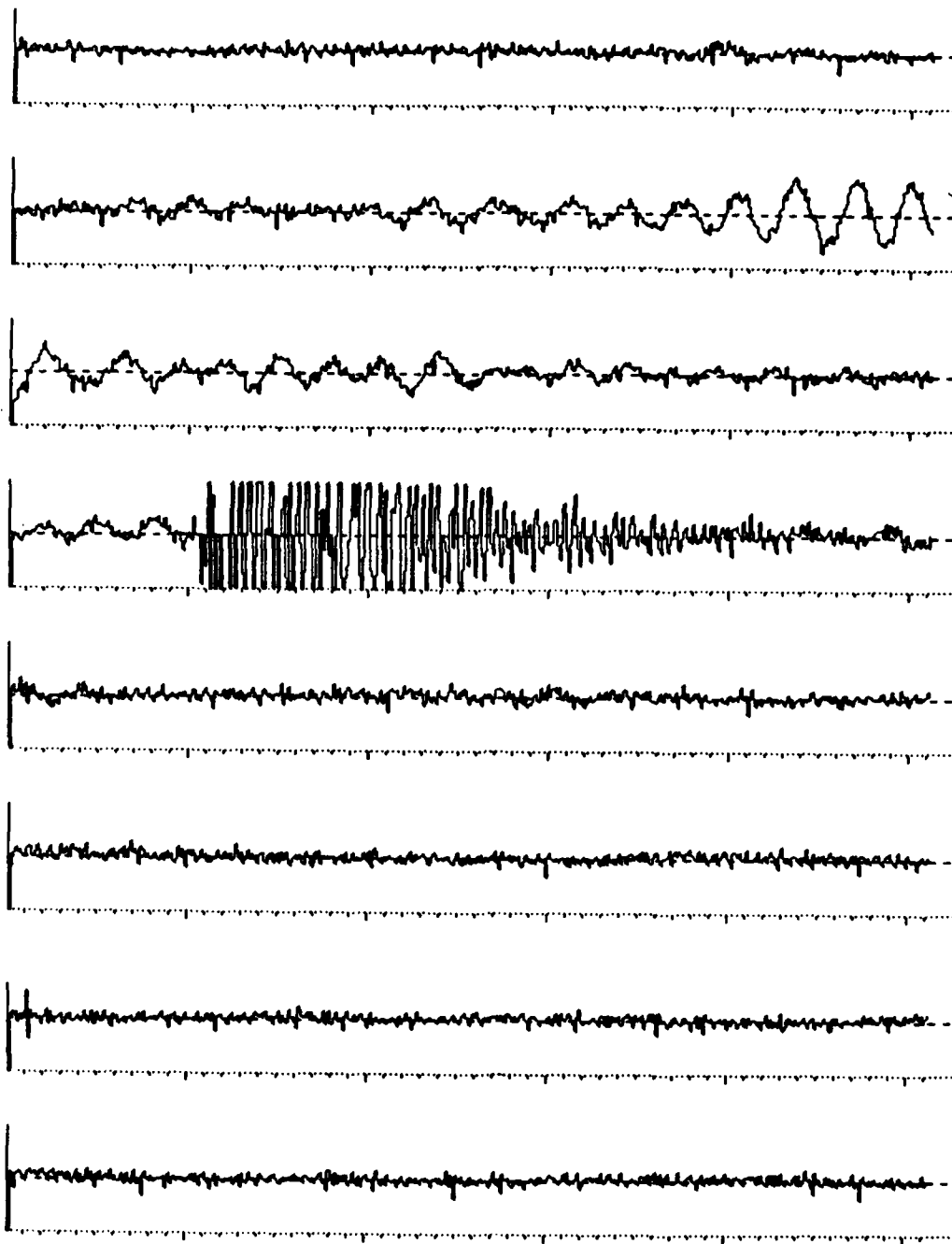
1.024 sec.

Figure 10c   Shot A20, Hydrophone 5
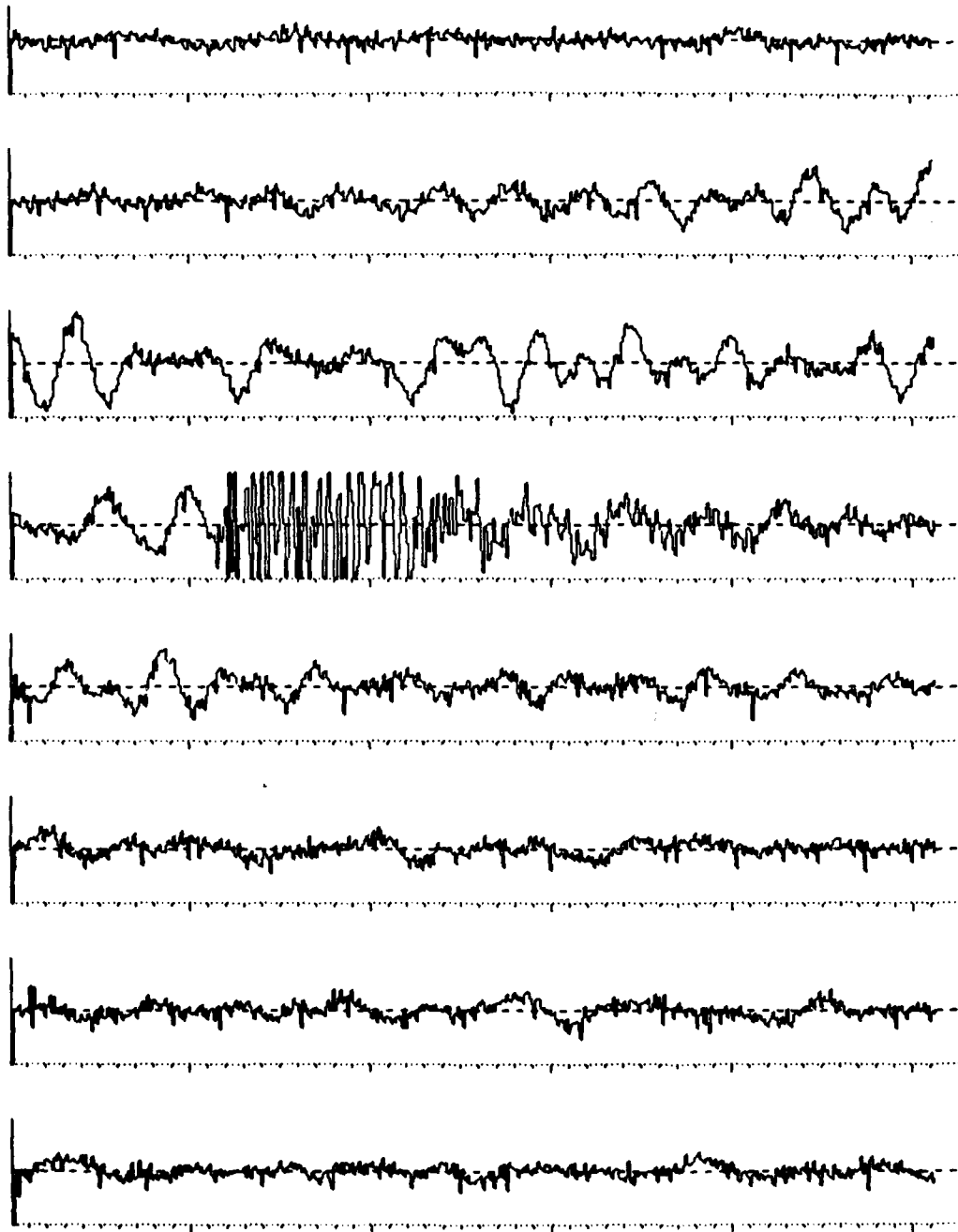
1.024 sec.

Figure 10d   Shot A20, Geophone 4X
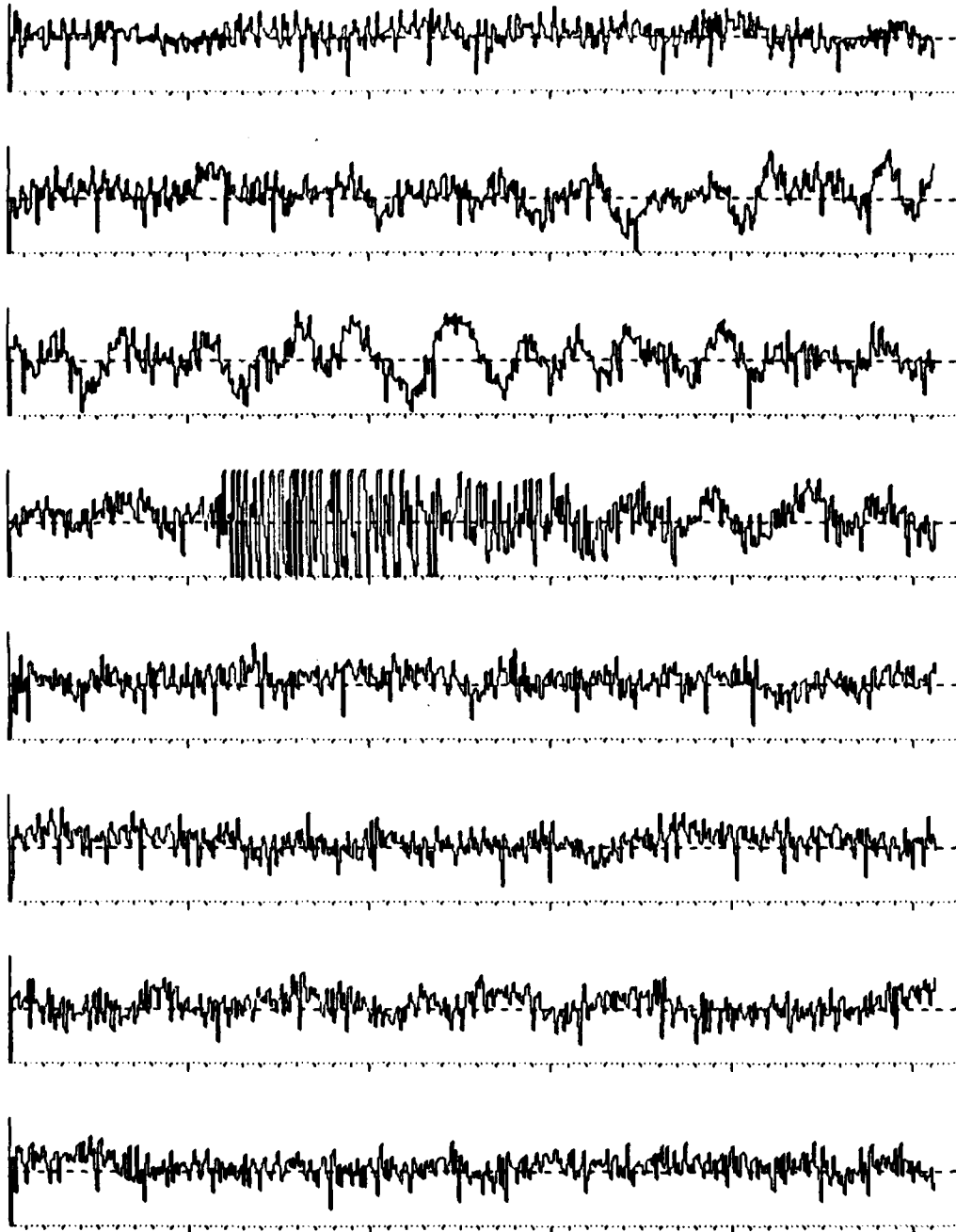
1.024 sec.

Figure 10e   Shot A20, Geophone 4Z
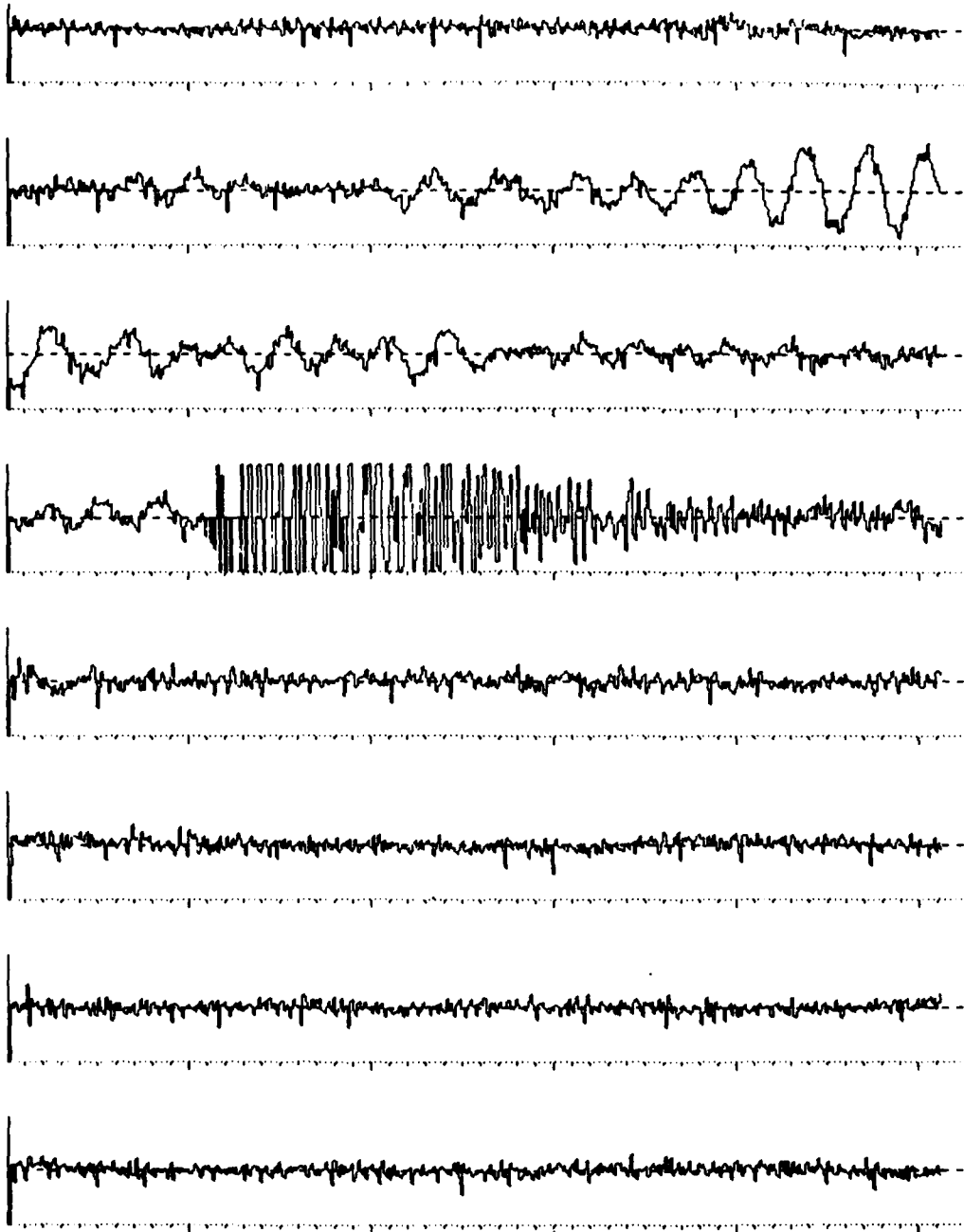
1.024 sec.

Figure 10f   Shot A20, Hydrophone 4
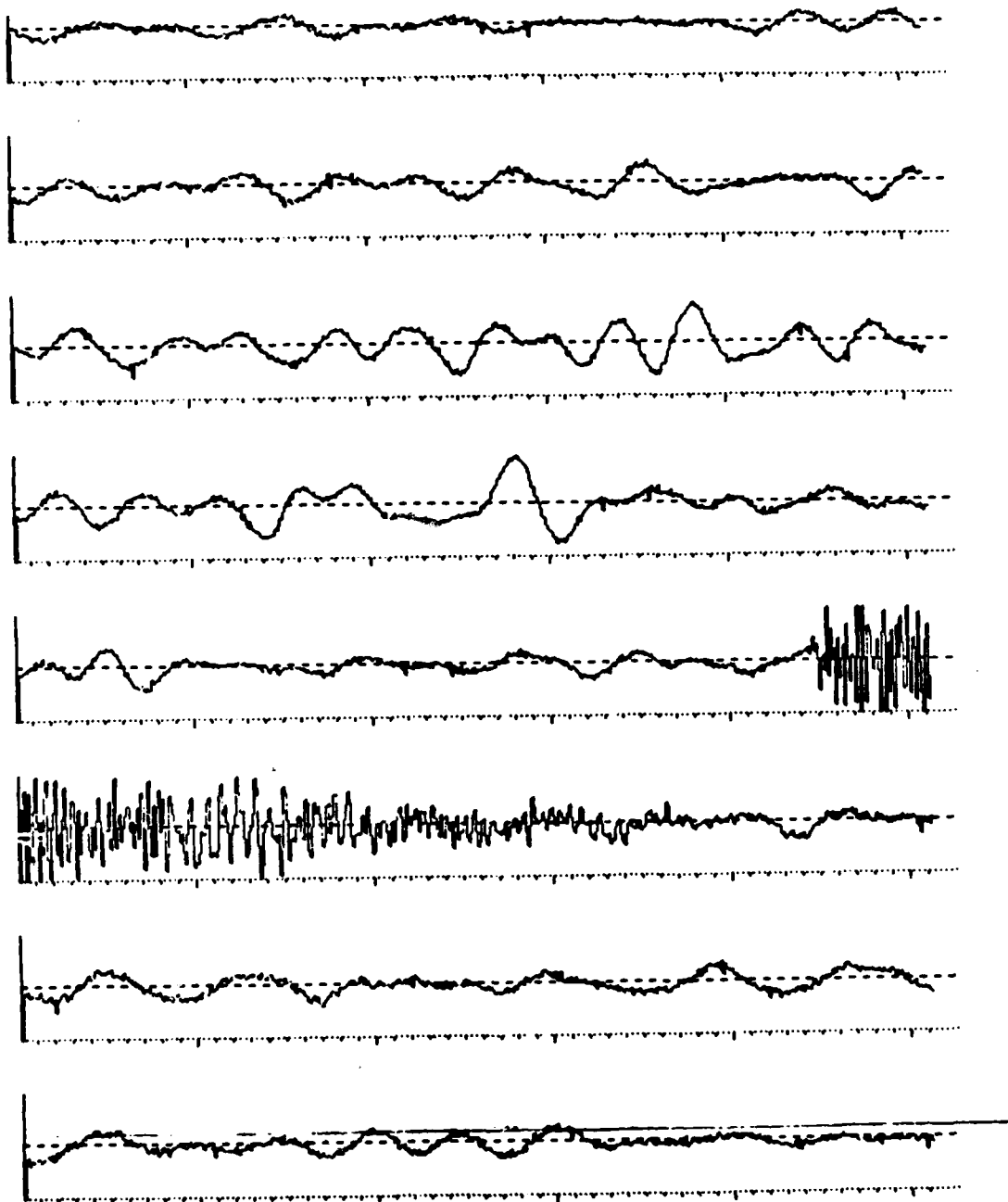
1.024 sec.

Figure 11a   Shot A14, Geophone 5X
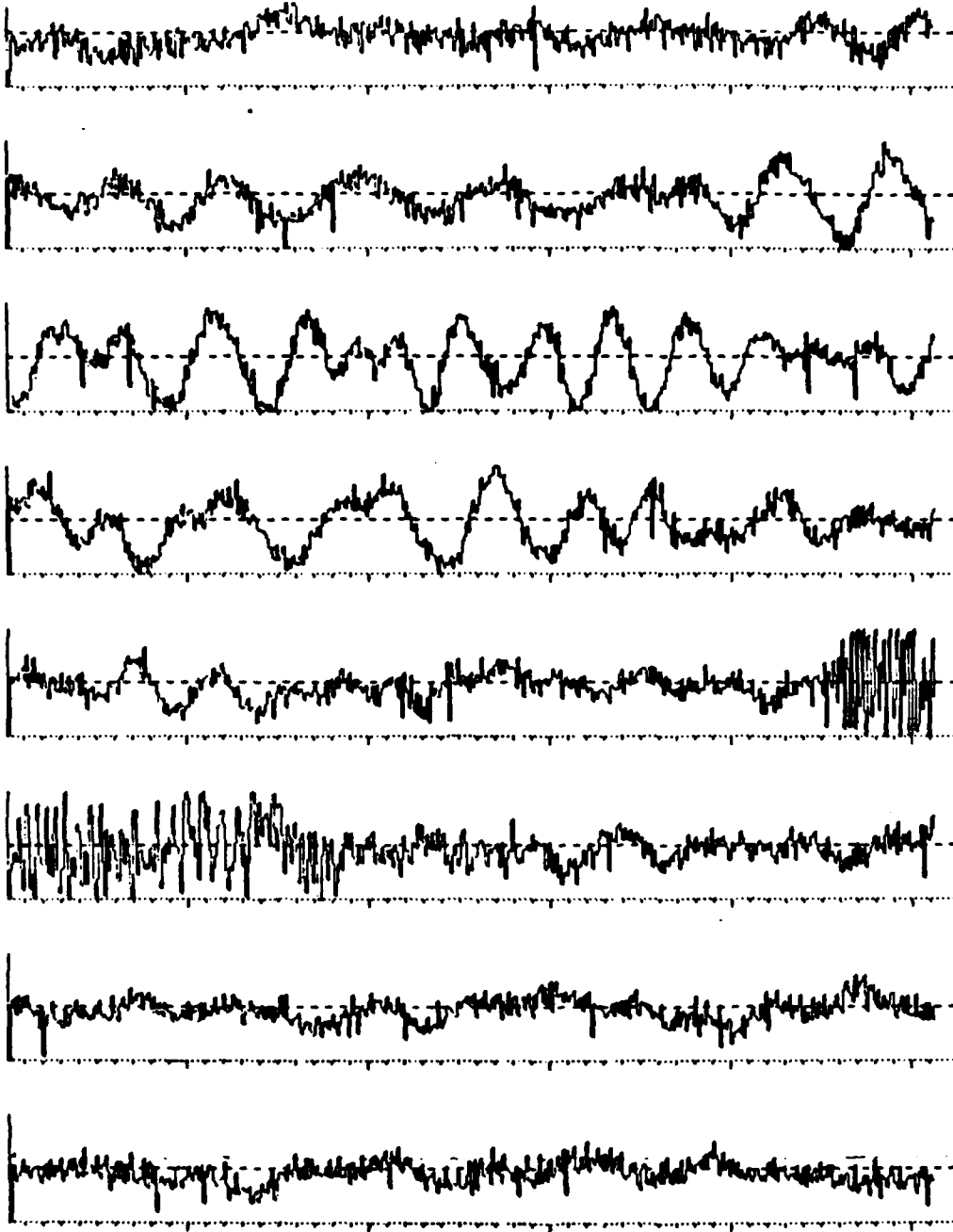
1.024 sec.

Figure 11b   Shot A14, Geophone 5Z
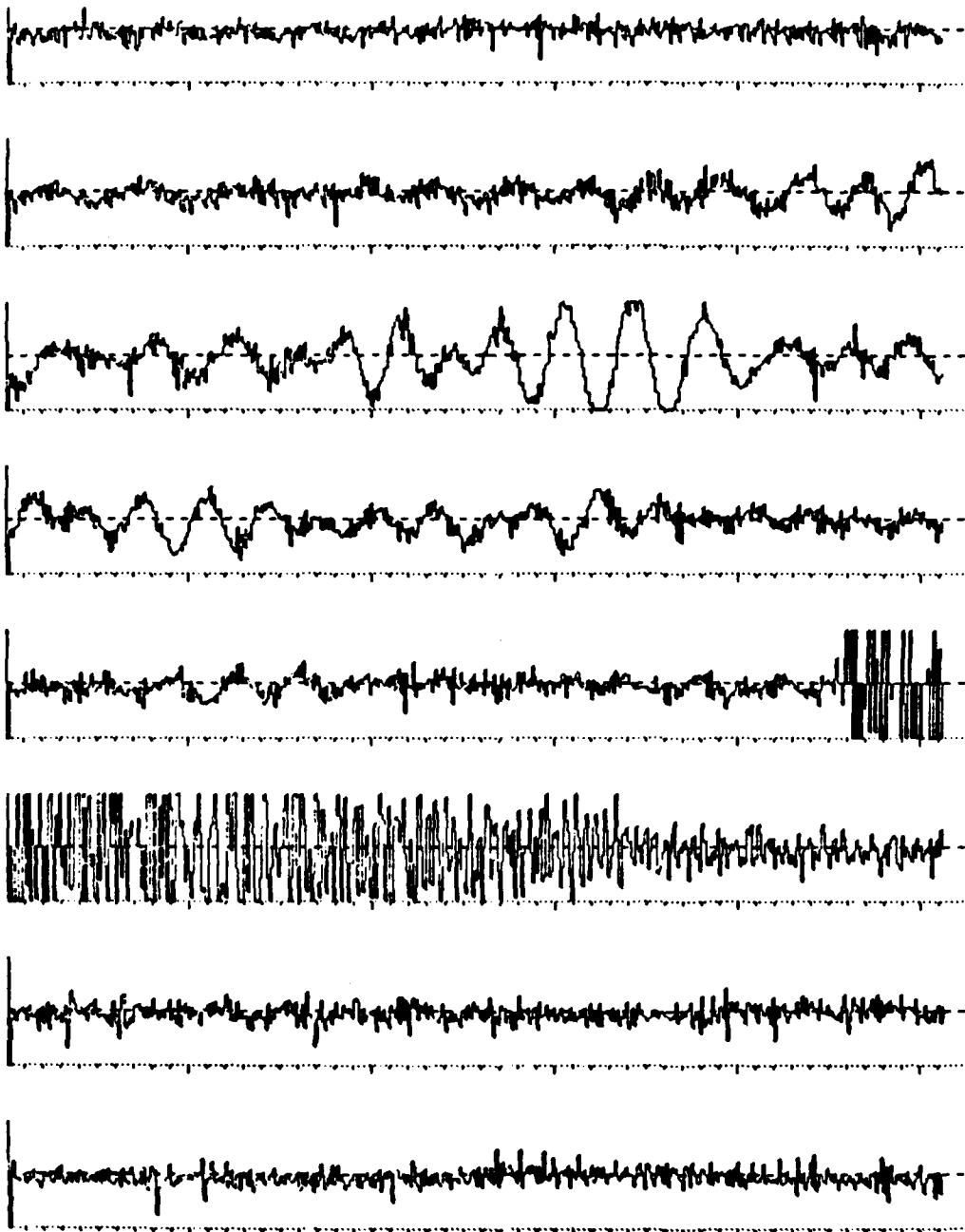
1.024 sec.

Figure 11c   Shot A14, Hydrophone 5
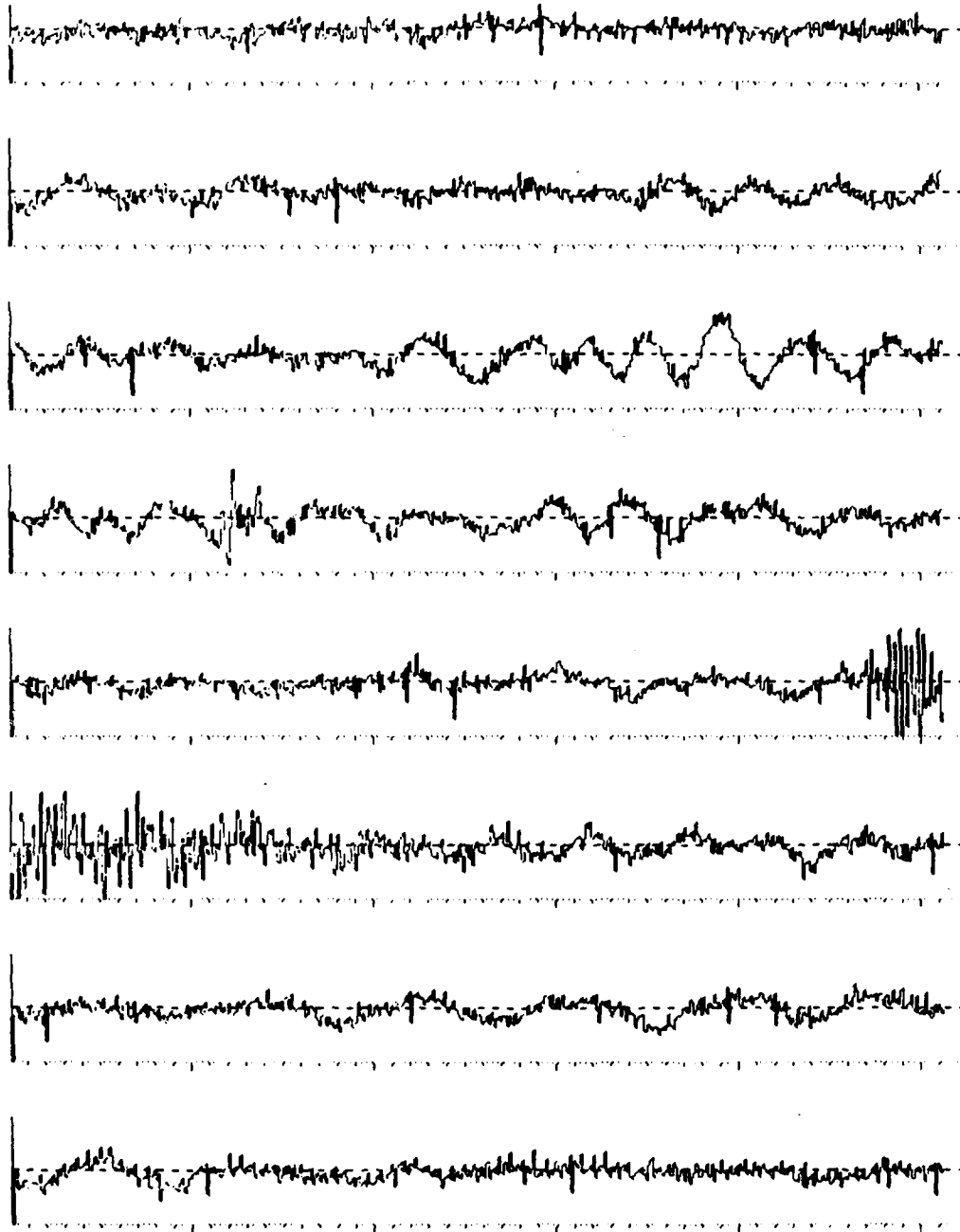
1.024 sec.

Figure 11d   Shot A14, Geophone 4X
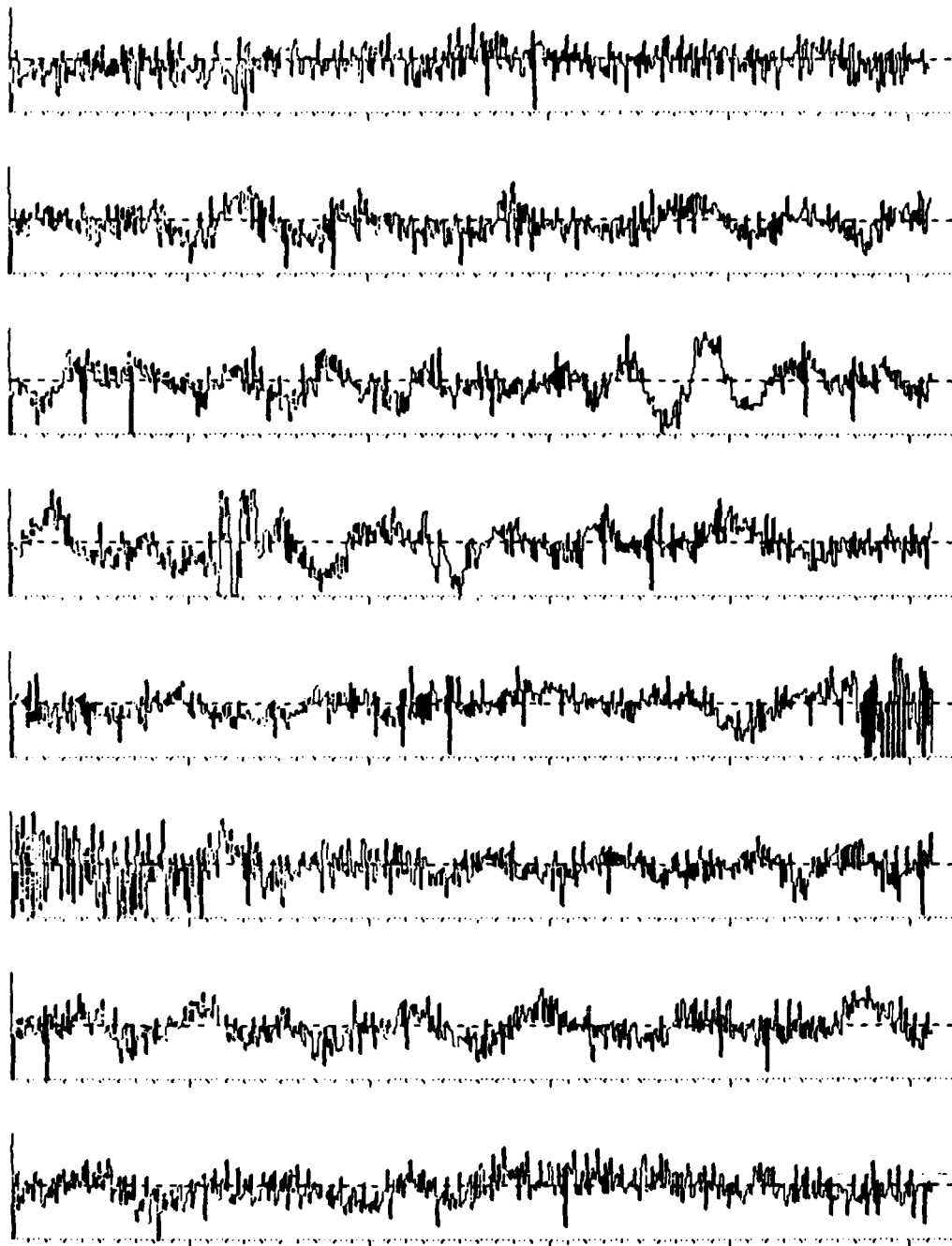
1.024 sec.

Figure 11e   Shot A14, Geophone 4Z
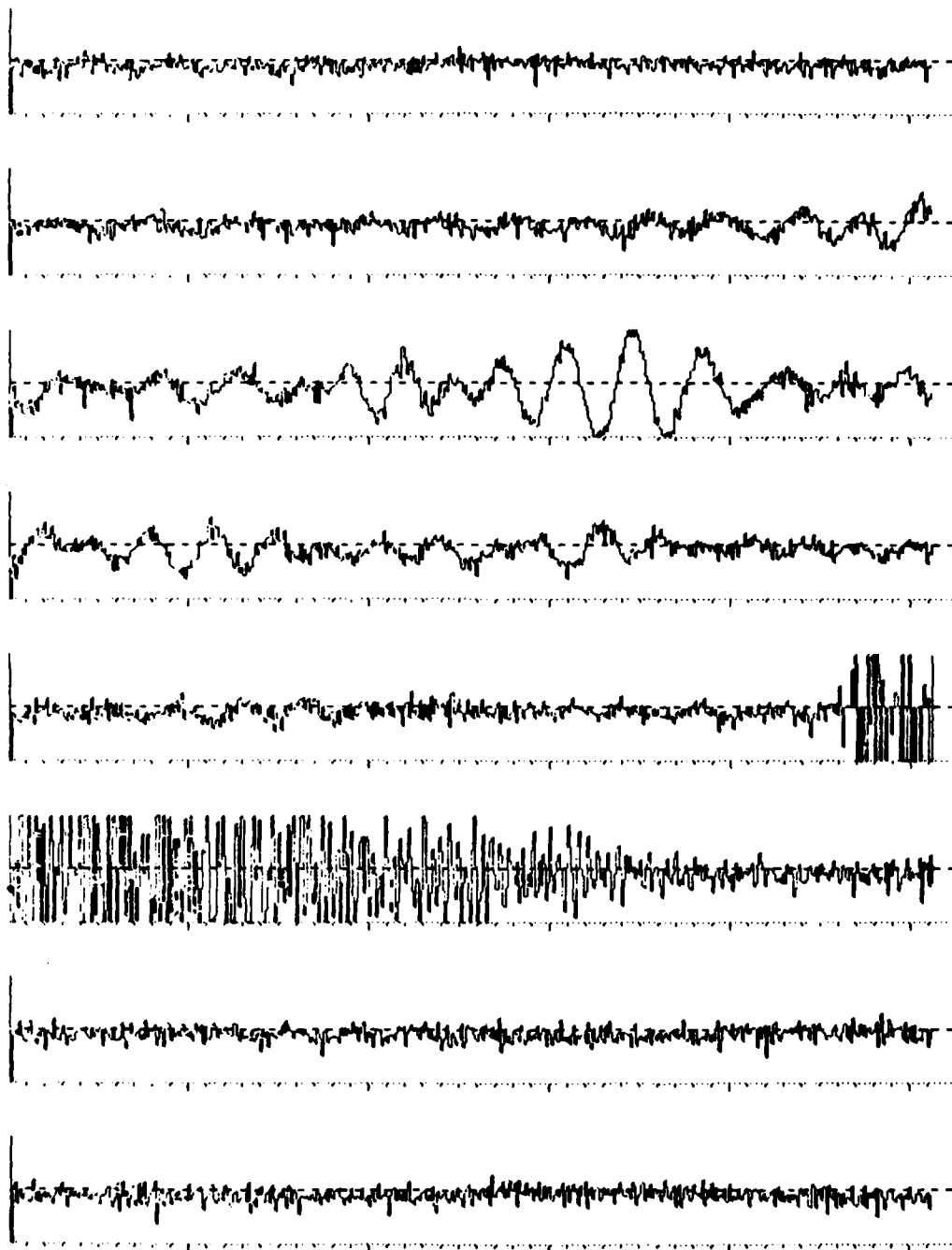
1.024 sec.

Figure 11f   Shot A14, Hydrophone 4

components. In each of the signal traces, the long term mean has been removed. Transparencies of these high resolution traces were overlaid to facilitate preliminary judgments regarding mode polarization states and array transit times. This examination of polarization led to the assignment of $S_1 S_2 S_1$ as the propagation mode for the third seismic arrival. It also was helpful in searching for the direct S_1 (?) propagation mode. Seismic energy was observed, in the geophone signals, to persist for a significant time after the water-wave arrival. Most of this "coda" appeared to arrive as a P wave, except for the possible S_1 mode. The mechanisms and propagation paths for the coda were not pursued, owing to its complexity. A listing of measured signal-to-noise ratios for the seismic modes is presented in Table 4. SNR's were derived using maximum signal and noise amplitudes, respectively.

During the preliminary investigation of the high resolution time traces, it became obvious that the bulk of the pre-first arrival signals, in any given shot, were very highly correlated, at zero relative time shift, for all sensors in the array. Correlated amplitude "glitches" were also seen occurring throughout the data in a periodic fashion (about every 3/4 seconds). Since a signal of this sort could arise naturally only as a plane wave incident vertically on the array, it is quite unlikely that its origin lay in phenomena typically expected to characterize the array environment. This signal is discussed further in later sections.

2.2 Spectral Analysis

The selected digital data signals were next analyzed to determine their temporal and spectral content. The principal

TABLE 4

MEASURED SEISMIC MODE SIGNAL-TO-NOISE LEVELS
FOR
VARIOUS SENSORS

Shot Number	Mode	Sensor*					
		5X	5Z	5H	4X	4Z	4H
A27	$P_1P_2P_1$	4 (4)	3 (3)	5 (2)	1 (2)	-6 (1)	6 (3)
	$P_1S_2P_1$	17 (4)	12 (2)	16 (2)	10 (2)	3 (2)	16 (3)
	$S_1S_2S_1$	15 (5)	9 (2)	14 (3)	12 (2)	1 (1)	14 (3)
	P_1	18 (4)	11 (2)	12 (3)	12 (2)	-3 (2)	12 (3)
A25	$P_1P_2P_1$	0 (6)	1 (1)	7 (2)	-4 (3)	-13 (1)	3 (3)
	$P_1S_2P_1$	17 (6)	5 (2)	13 (2)	3 (2)	-1 (2)	9 (2)
	$S_1S_2S_1$	17 (6)	4 (2)	15 (2)	2 (2)	-3 (2)	5 (2)
	P_1	27 (6)	9 (1)	15 (3)	13 (2)	4 (2)	13 (3)
A20	$P_1P_2P_1$	2 (4)	-5 (1)	-6 (1)	-13 (1)	-16 (2)	-12 (1)
	$P_1S_2P_1$	8 (4)	1 (1)	-2 (2)	-4 (2)	-14 (2)	-1 (1)
	$S_1S_2S_1$	8 (4)	6 (2)	0 (1)	0 (2)	-10 (2)	-1 (1)
	P_1	21 (4)	11 (1)	3 (2)	5 (2)	-6 (1)	2 (1)
A14	$P_1P_2P_1$	2 (2)	-3 (1)	-14 (1)	--	-8 (1)	-13 (1)
	$P_1S_2P_1$	3 (3)	-4 (2)	-10 (2)	-6 (1)	-10 (1)	-13 (1)
	$S_1S_2S_1$	5 (2)	-4 (2)	-10 (2)	-8 (1)	-7 (1)	-13 (1)
	P_1	9 (3)	2 (2)	3 (1)	-2 (1)	-4 (1)	0 (1)

*All signal-to-noise levels in decibels; estimated error in parenthesis.

ENSCO, Inc.   - 43 -

working tool to facilitate this process was the spectrogram, which is a graphic representation of signal power as a function of time and frequency. An extensive collection of spectrograms for the selected shot signals are shown in Figures 12 through 15. Prior to spectral analysis, the signals were digitally filtered and decimated to a sampling rate of 500 Hz.

Every display line in each spectrogram was developed from 1/4 second segments of the input time series. Each such data block was augmented with zeros to a total length of one second. Thus, the spectral sampling increment is one hertz. The temporal analysis window (of 1/4 second length) was incremented (slipped) by 1/8 second, thereby producing a 50% overlapped spectrogram. Analysis bandwidth spans the range from -250 Hz to +250 Hz (i.e., to the Nyquist sampling limits). After the Fourier transform of each zero-filled time data block was obtained, its logarithmic power spectrum was computed. The upper 10 dB of each such spectrum was converted into a 10 level density format for plotting, all values below (relative) -10 dB having been blanked. Note that each spectrogram line is therefore scaled only locally, not globally. Also, since the digital signals were not bandshifted, the spectrograms are symmetric about 0 hertz. Indicators on the spectrograms mark the onset of different modes which comprise the seismic and hydroacoustic signal structure.

The spectrograms demonstrate clearly that the waterwave has a very broadband structure, compared with the seismic modes, on both the geophones and the hydrophones. Seismic energy appears to be confined generally to less than 25 Hz,
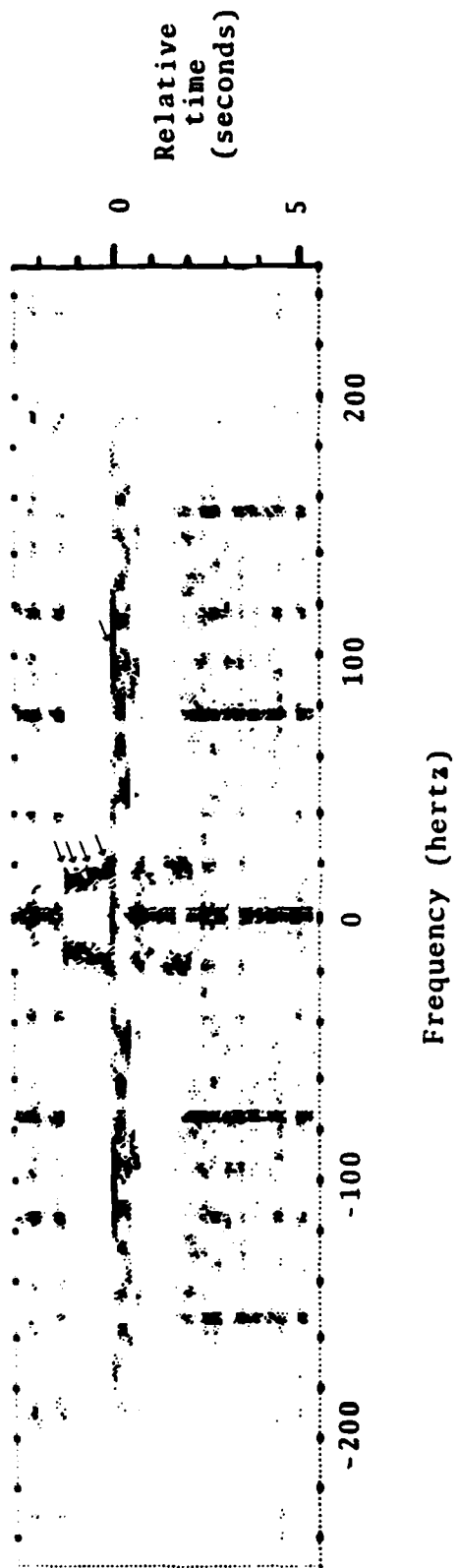
Figure 12a   Spectrogram, Shot A27, Hydrophone 5

Relative
time
(seconds)

Frequency (hertz)
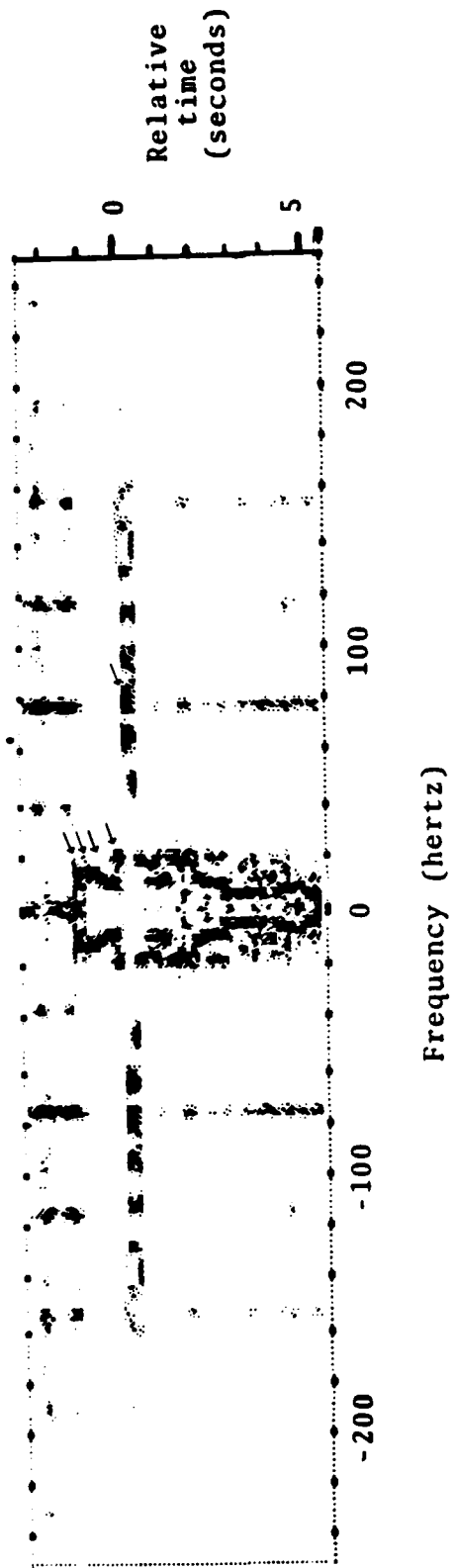
Figure 12b Spectrogram, Shot A27, Geophone 4X
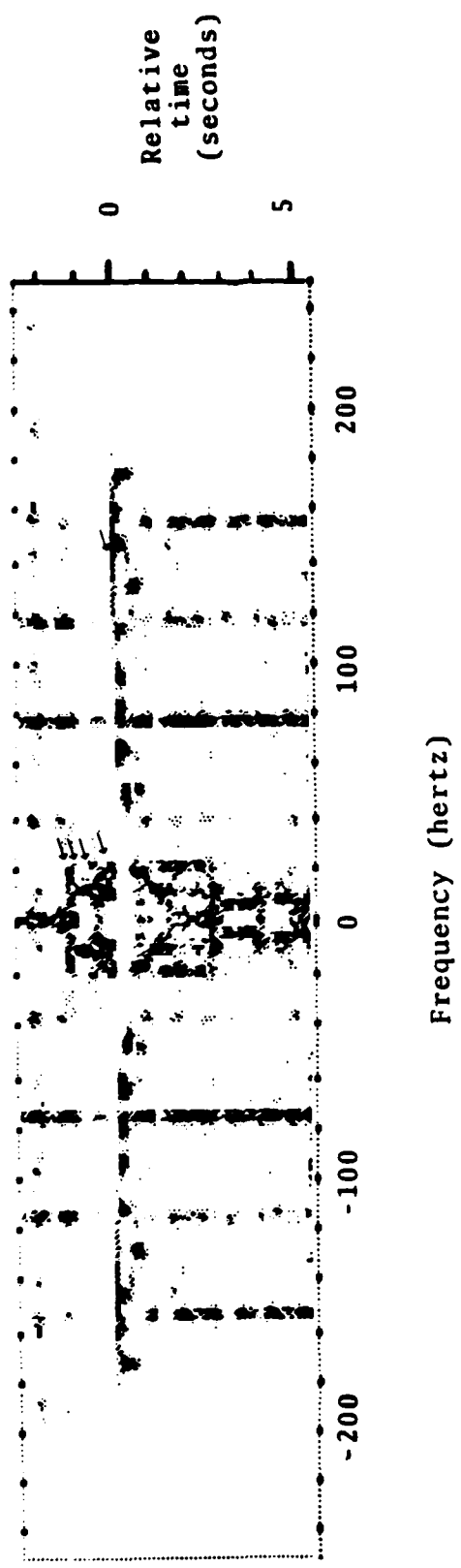
ENSCO, Inc.   - 46 -

Figure 12c Spectrogram, Shot A27, Geophone 4Z

Relative time (seconds)

Frequency (hertz)

ENSCO, Inc.   - 47 -
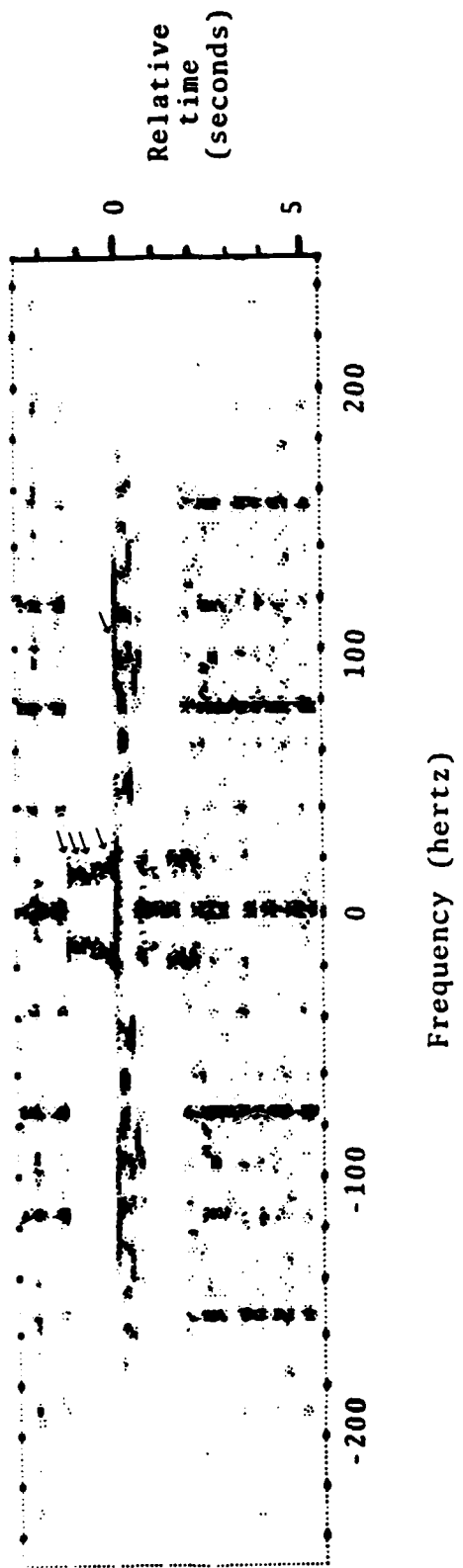
Figure 12d   Spectrogram, Shot A27, Hydrophone 4

Figure 12e Spectrogram, Shot A27, Geophone 6X
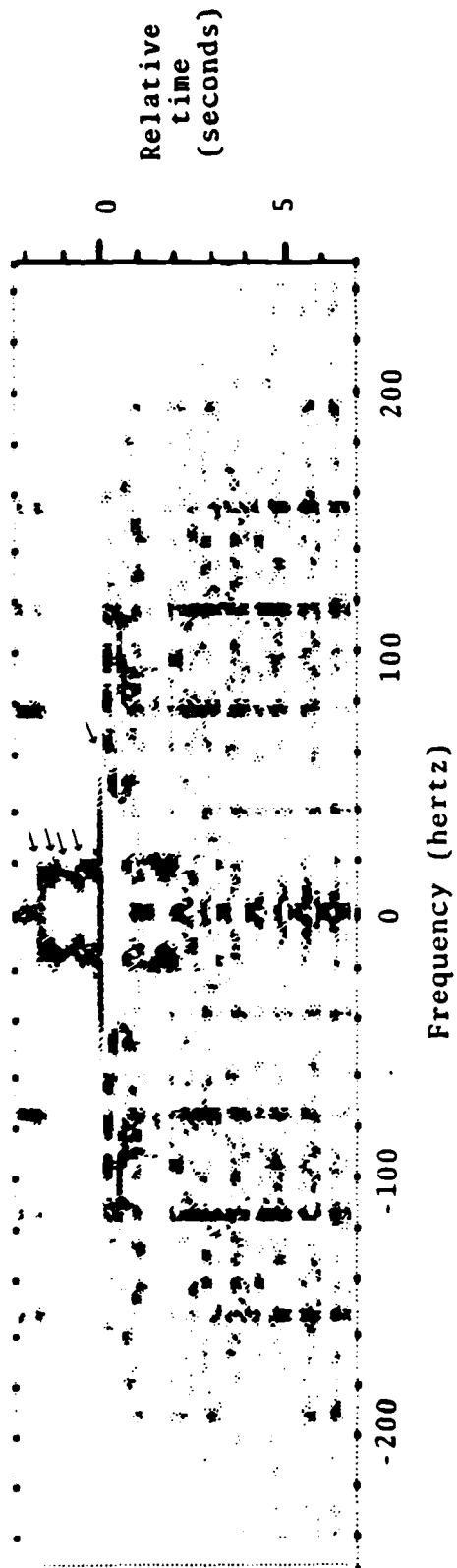
Figure 13a Spectrogram, Shot A25, Hydrophone 5

Figure 13b Spectrogram, Shot A25, Geophone 4X
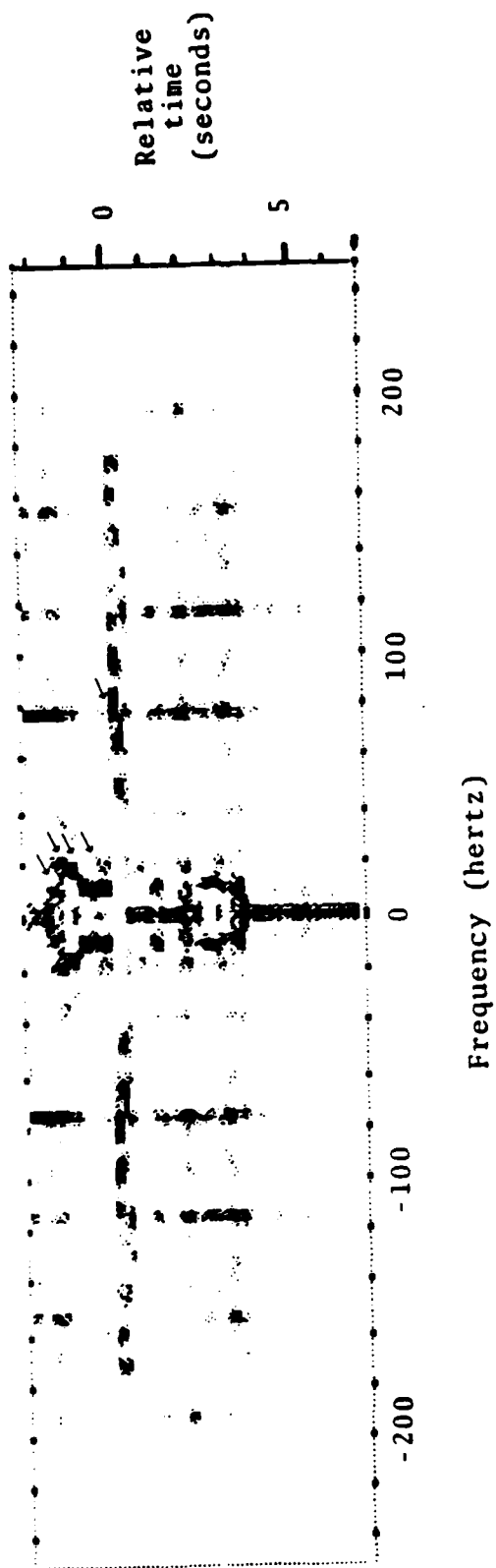
Figure 13c   Spectrogram, Shot A25, Geophone 4Z

ENSCO, Inc.   - 52 -

Figure 13d Spectrogram, Shot A25, Hydrophone 4

Figure 13e Spectrogram, Shot A25, Geophone 6X
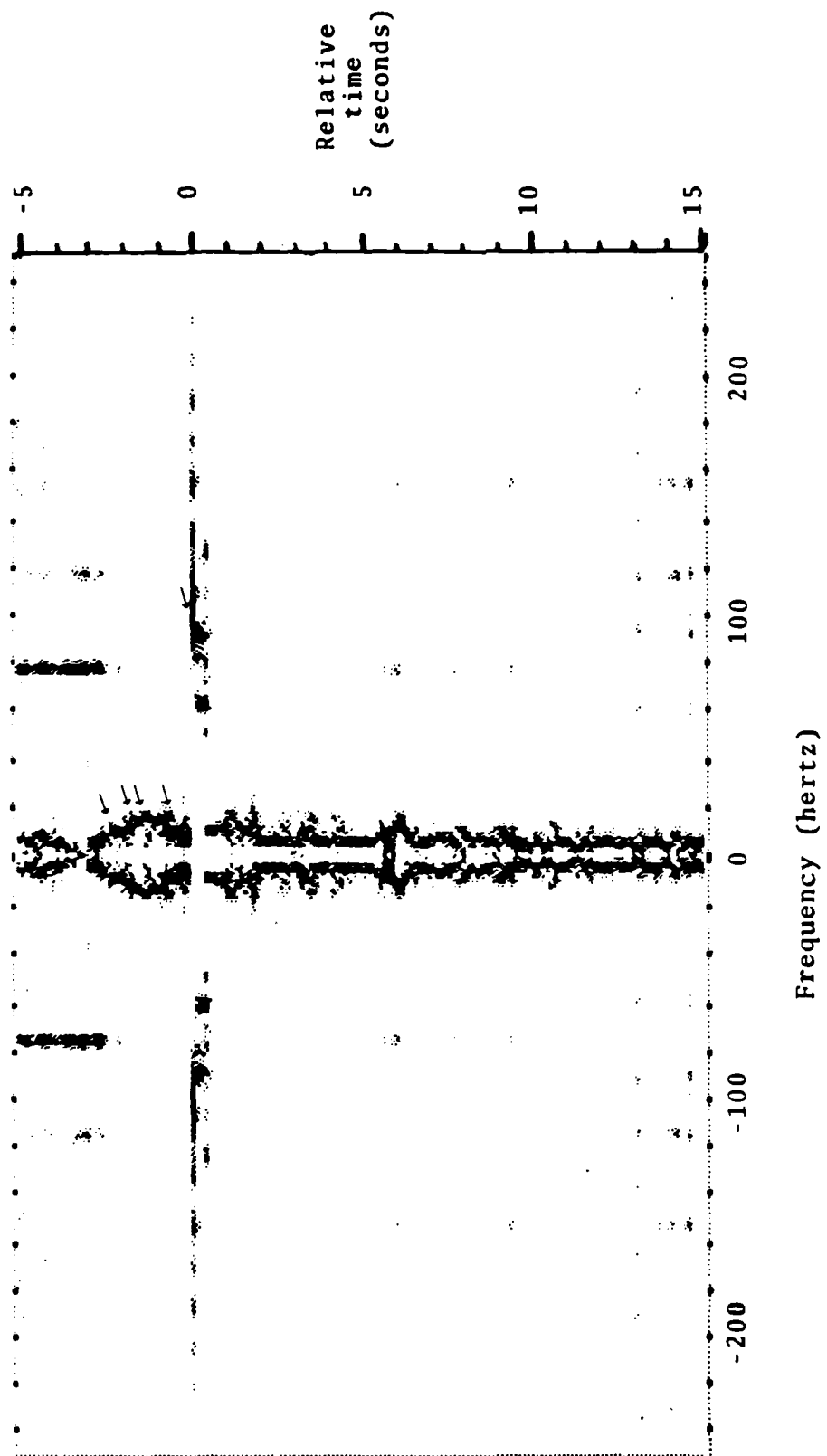
Figure 14a Spectrogram, Shot A20, Geophone 5X

Relative
time
(seconds)

-5

0

5

10

15

200

100

Frequency (hertz)

0

-100

-200
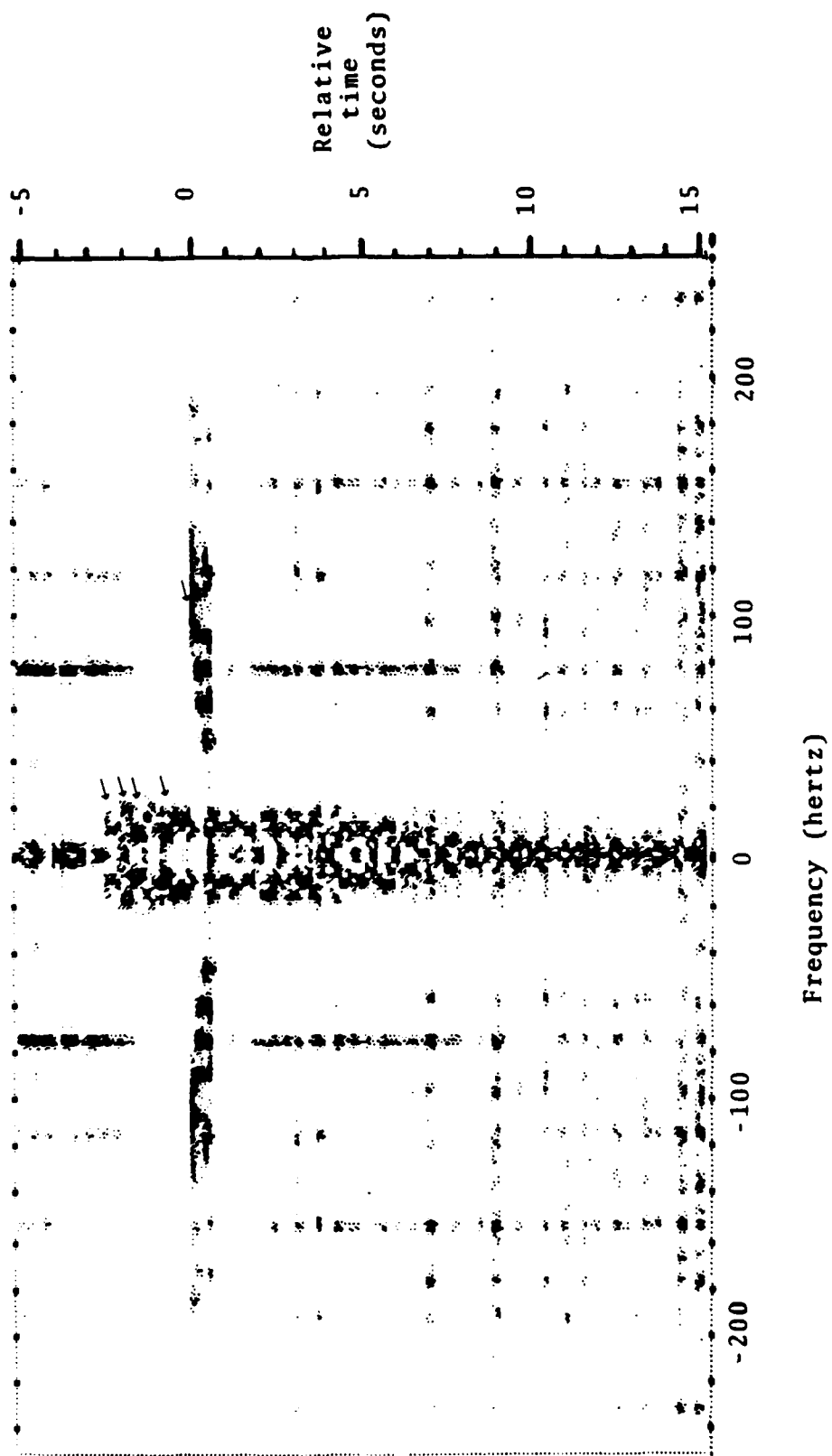
Figure 14b Spectrogram, Shot A20, Geophone 5Z

ENSCO, Inc.   - 56 -
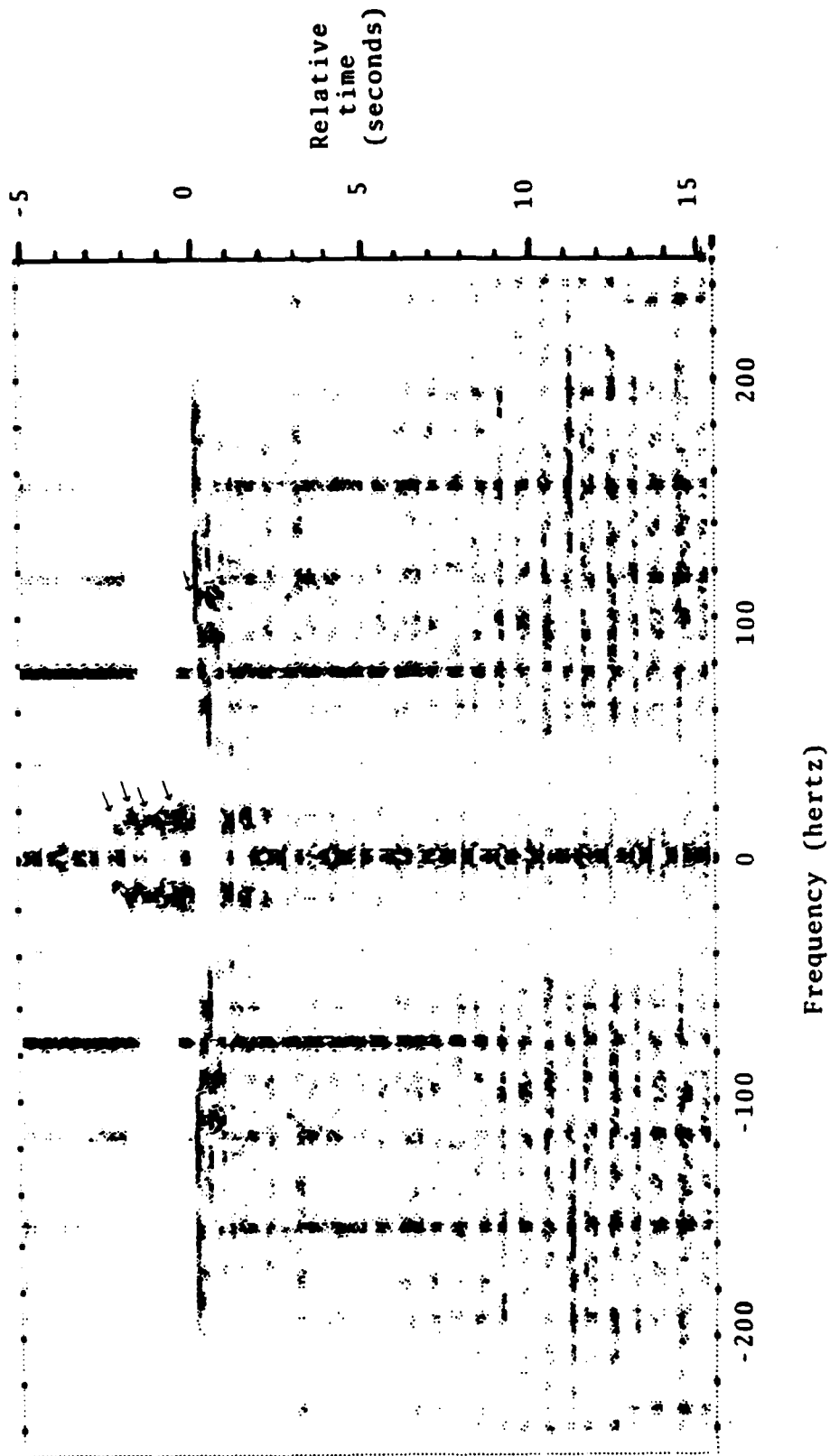
Figure 14c Spectrogram, Shot A20, Hydrophone 5

ENSCO, Inc.   - 57 -
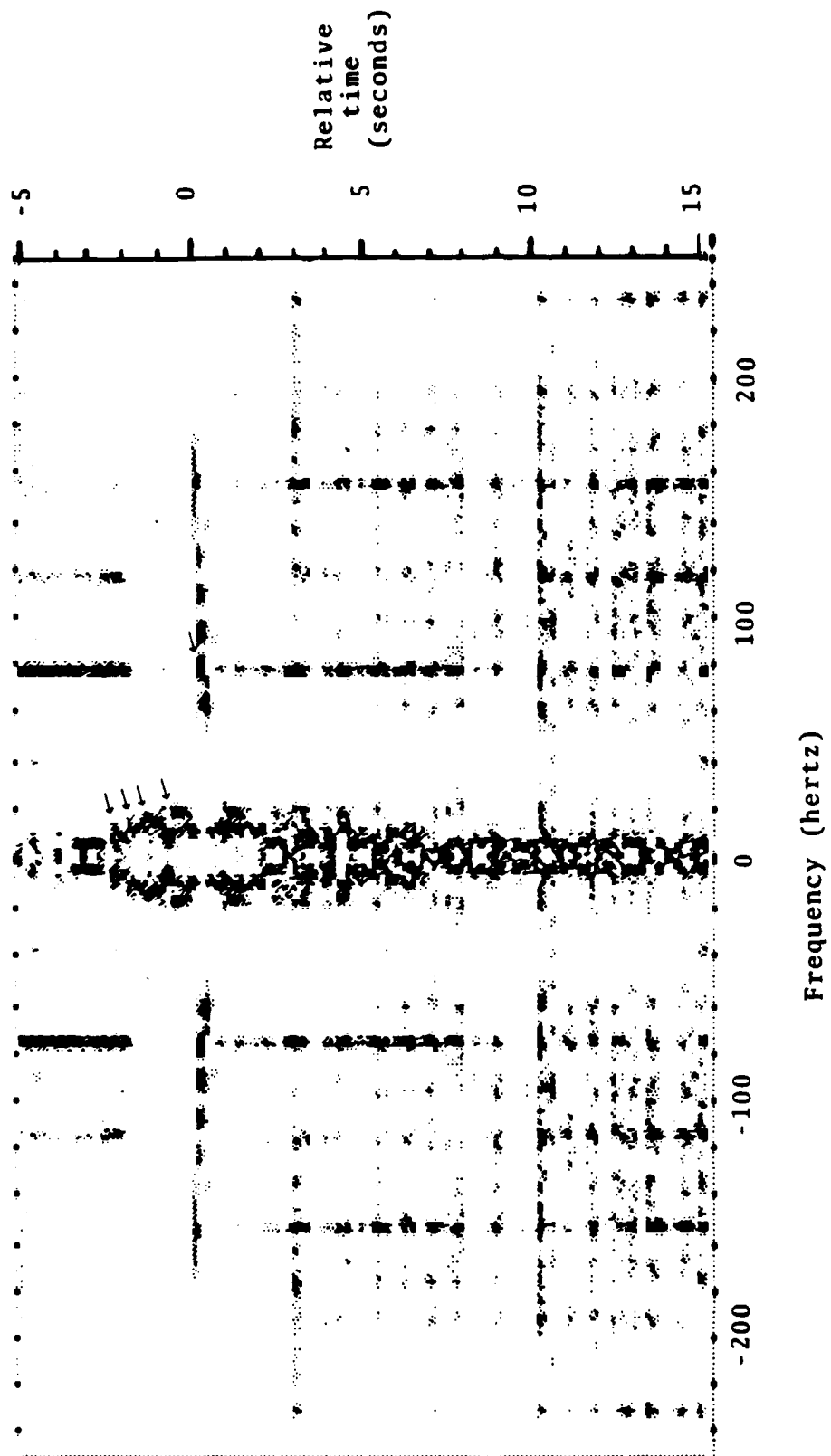
Figure 14d Spectrogram, Shot A20, Geophone 4X

Frequency (hertz)

Relative
time
(seconds)

ENSCO, Inc.   - 58 -
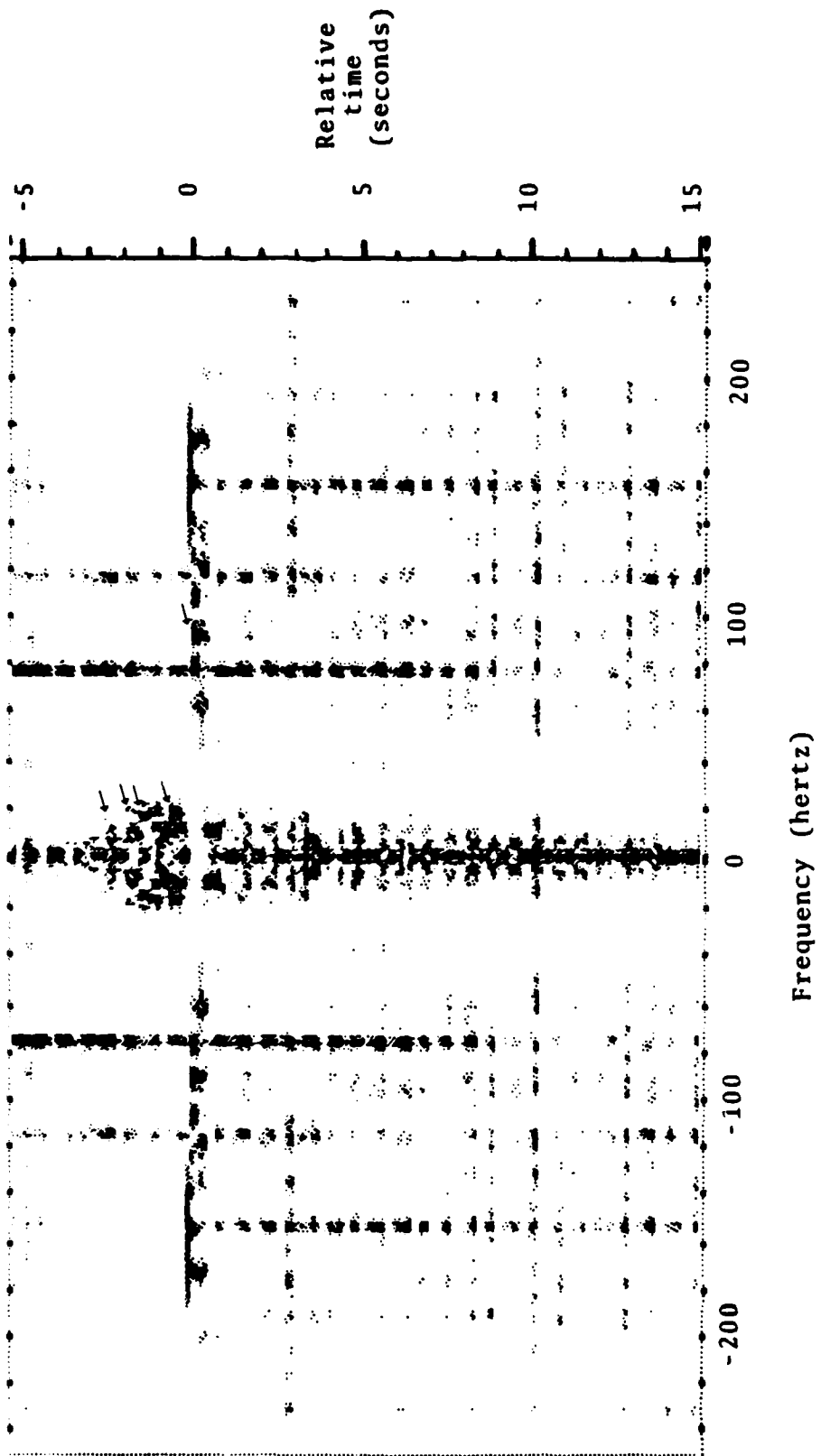
Figure 14e Spectrogram, Shot A20, Geophone 4Z
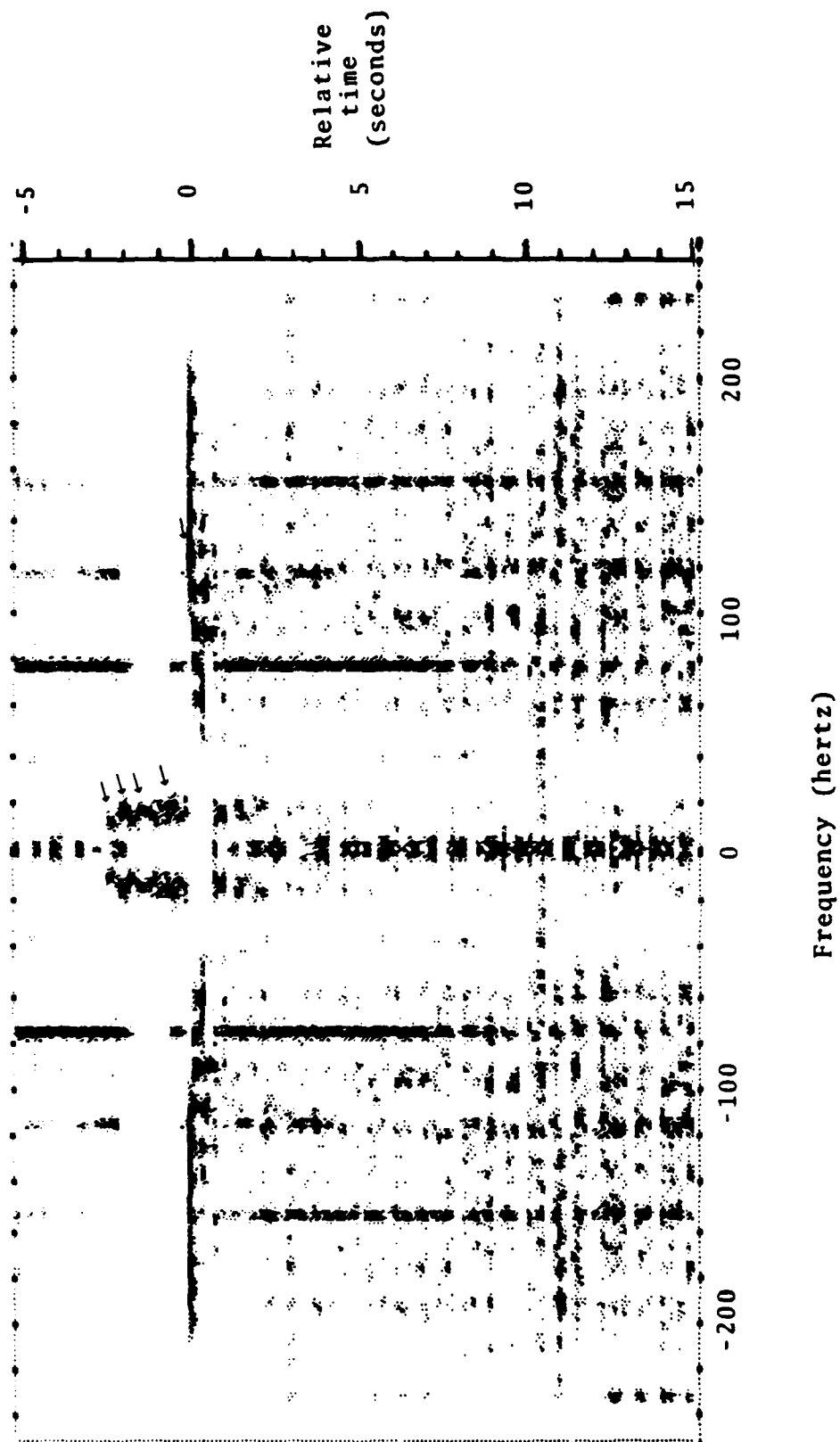
Figure 14f   Spectrogram, Shot A20, Hydrophone 4

ENSCO, Inc.   - 60 -
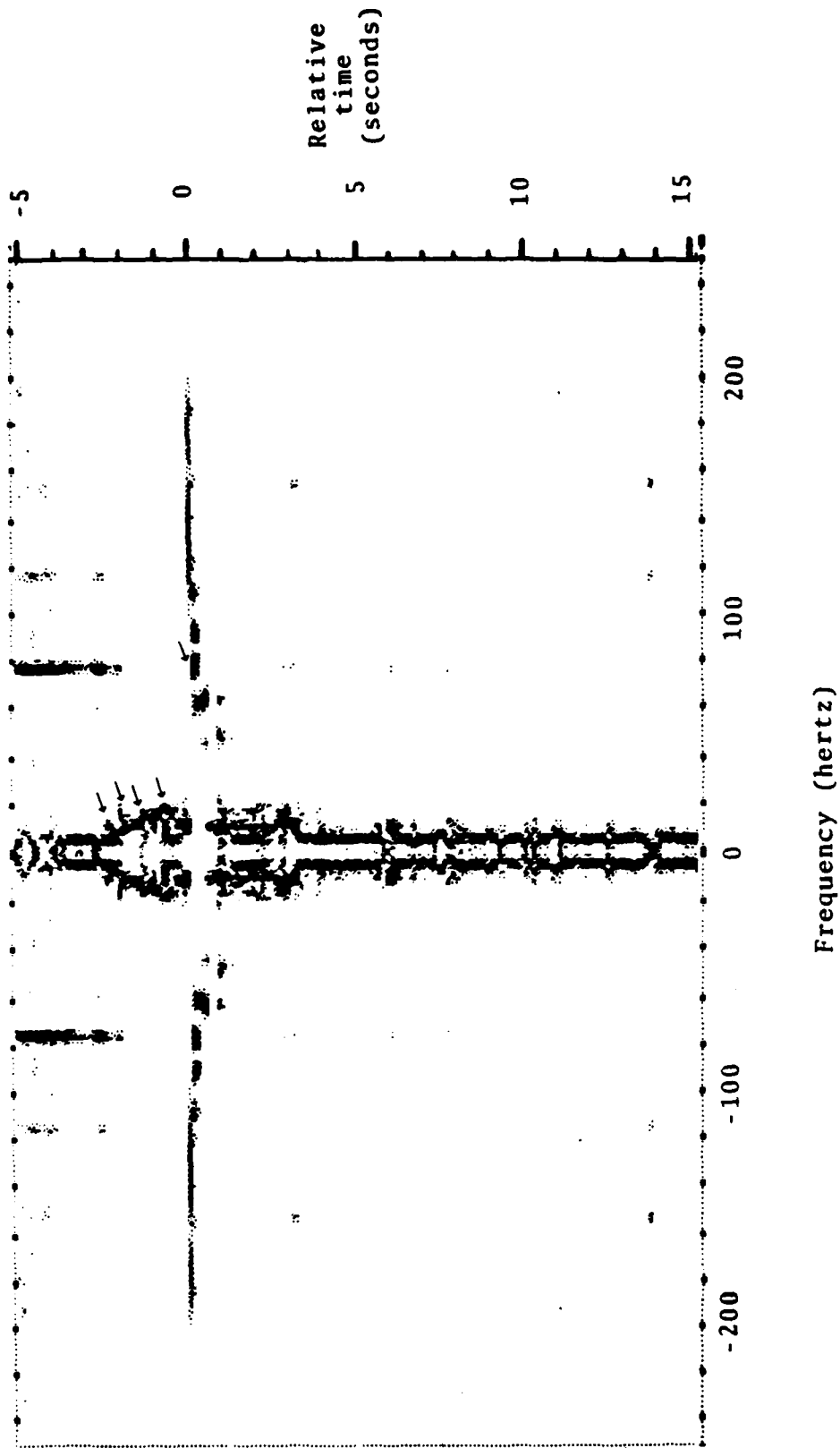
Figure 14g   Spectrogram, Shot A20, Geophone 6X

ENSCO, Inc.   - 61 -
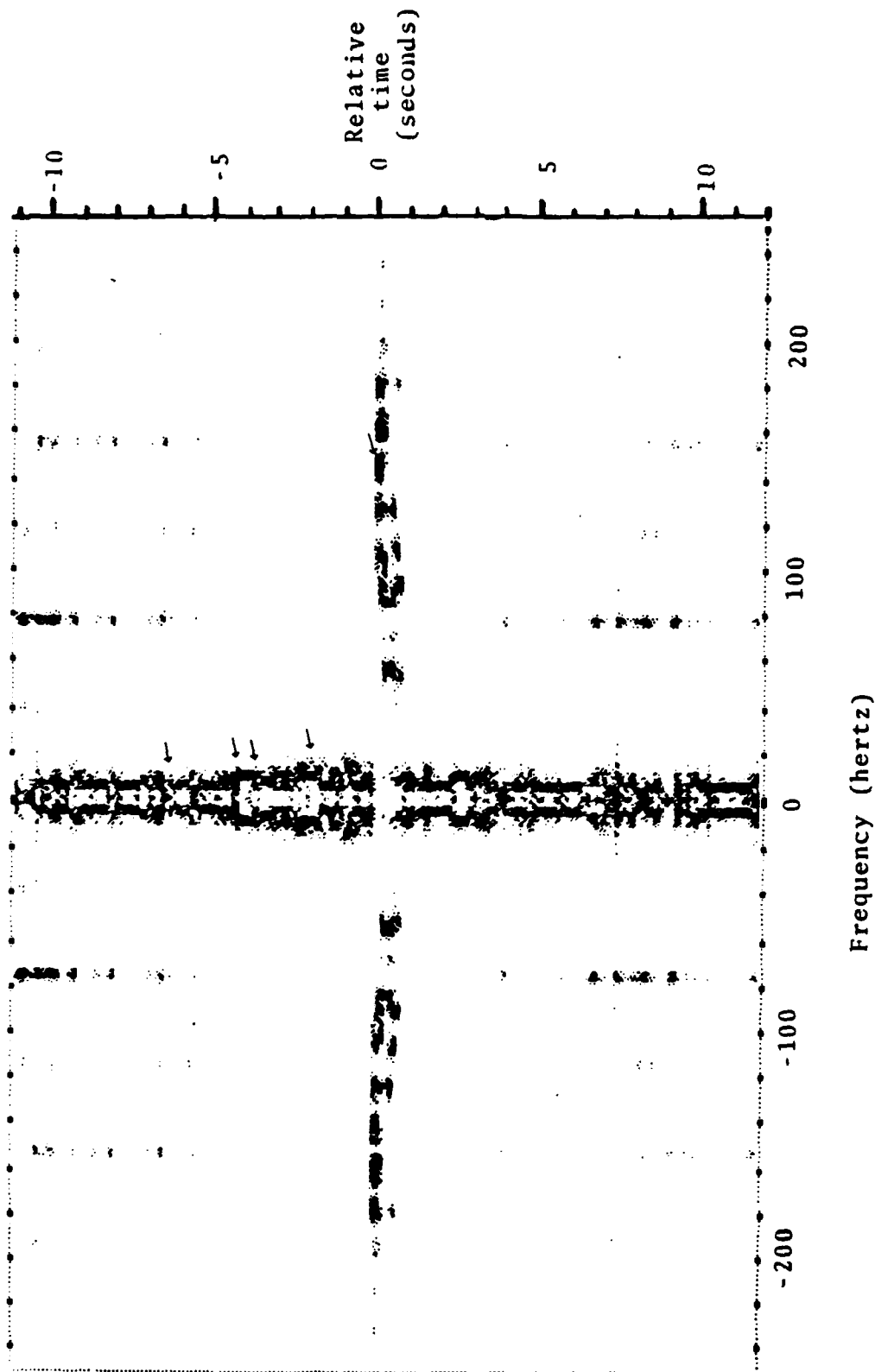
Figure 15a Spectrogram, Shot A14, Geophone 5X
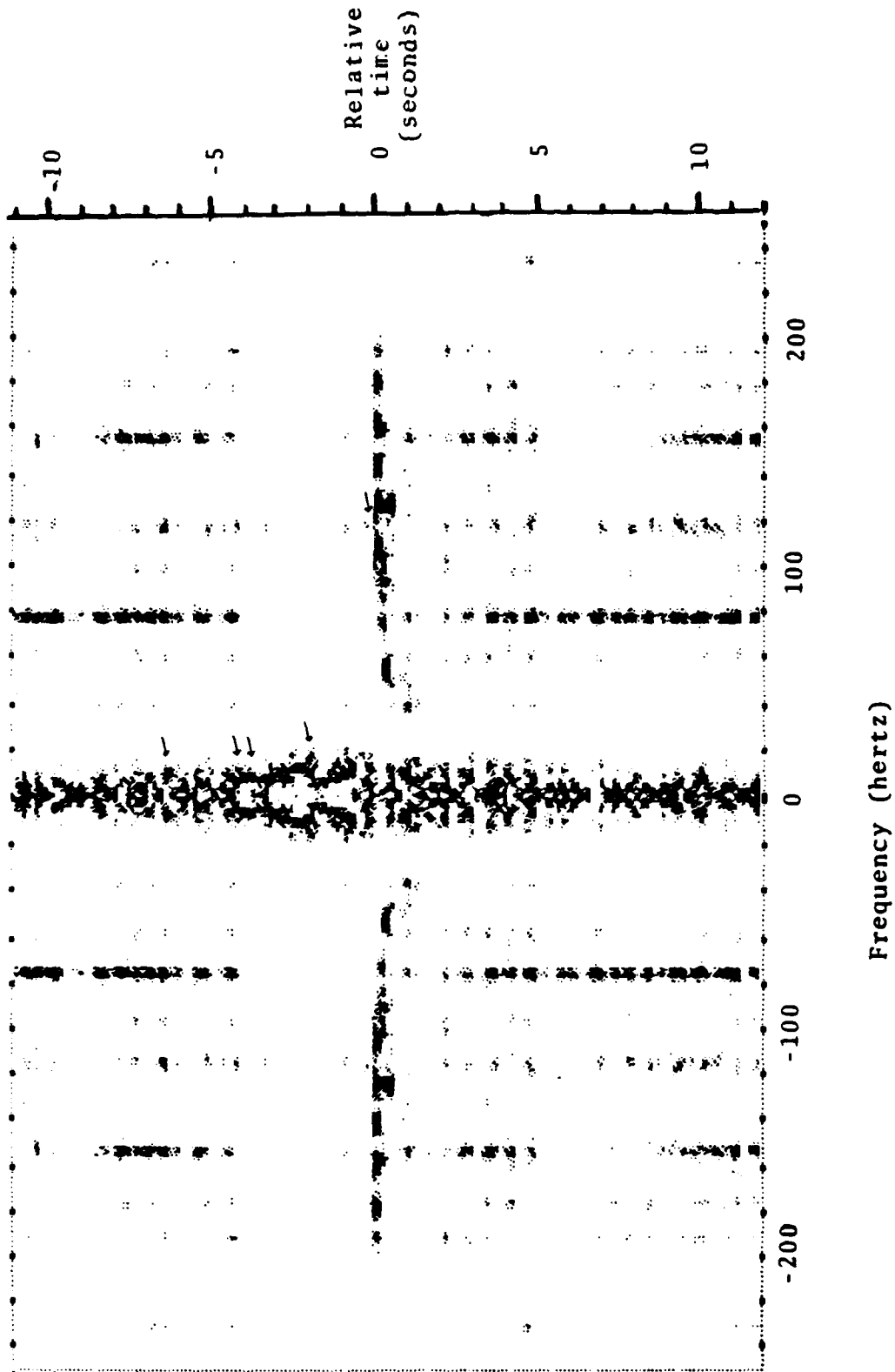
Figure 15b Spectrogram, Shot A14, Geophone 5Z

Relative time (seconds)

Frequency (hertz)

ENSCO, Inc.

- 63 -
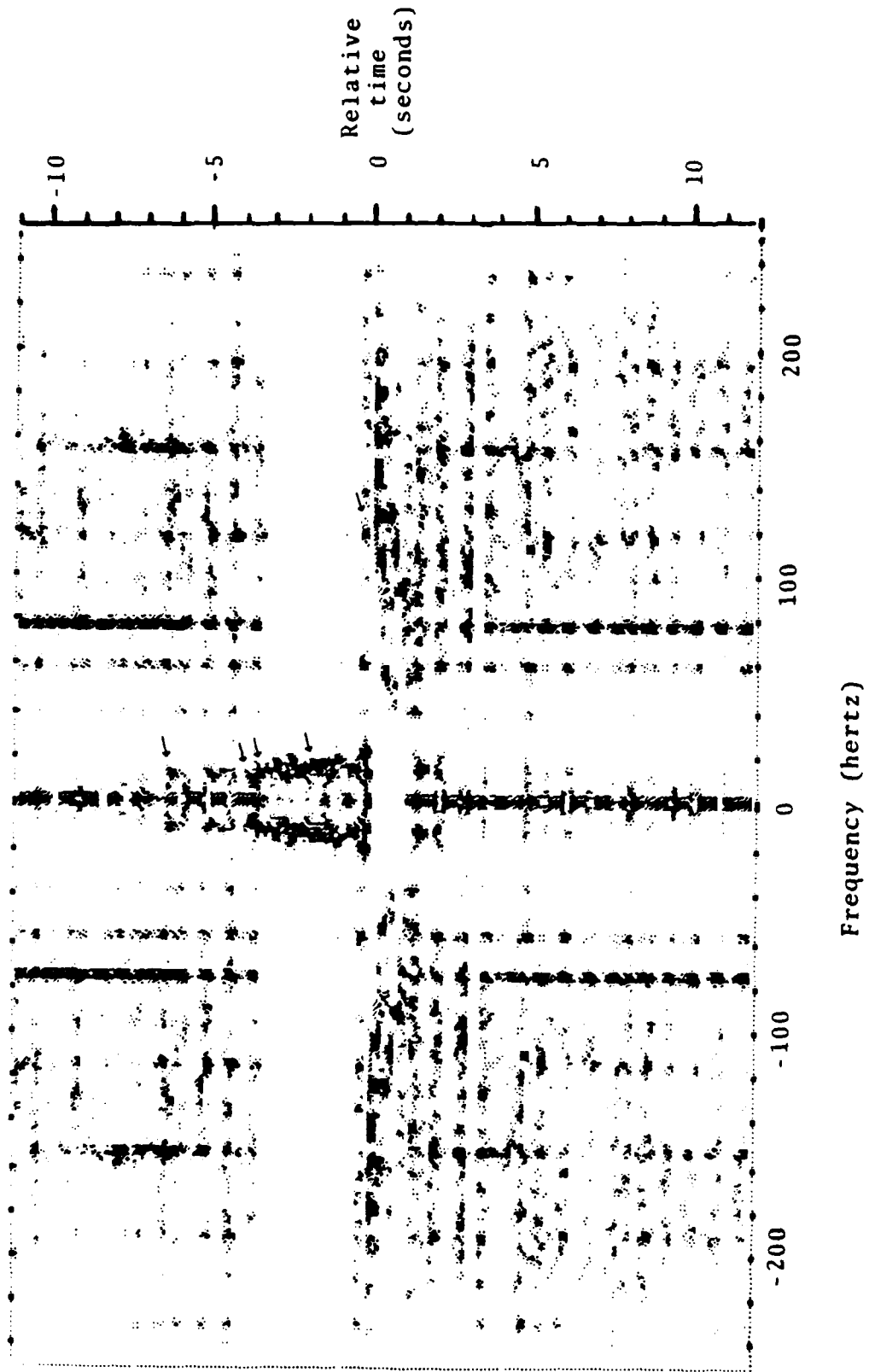
Figure 15c   Spectrogram, Shot A14, Hydrophone 5

Relative
time
(seconds)

-10

-5

0

5

10

200

100

0

-100

-200

Frequency (hertz)
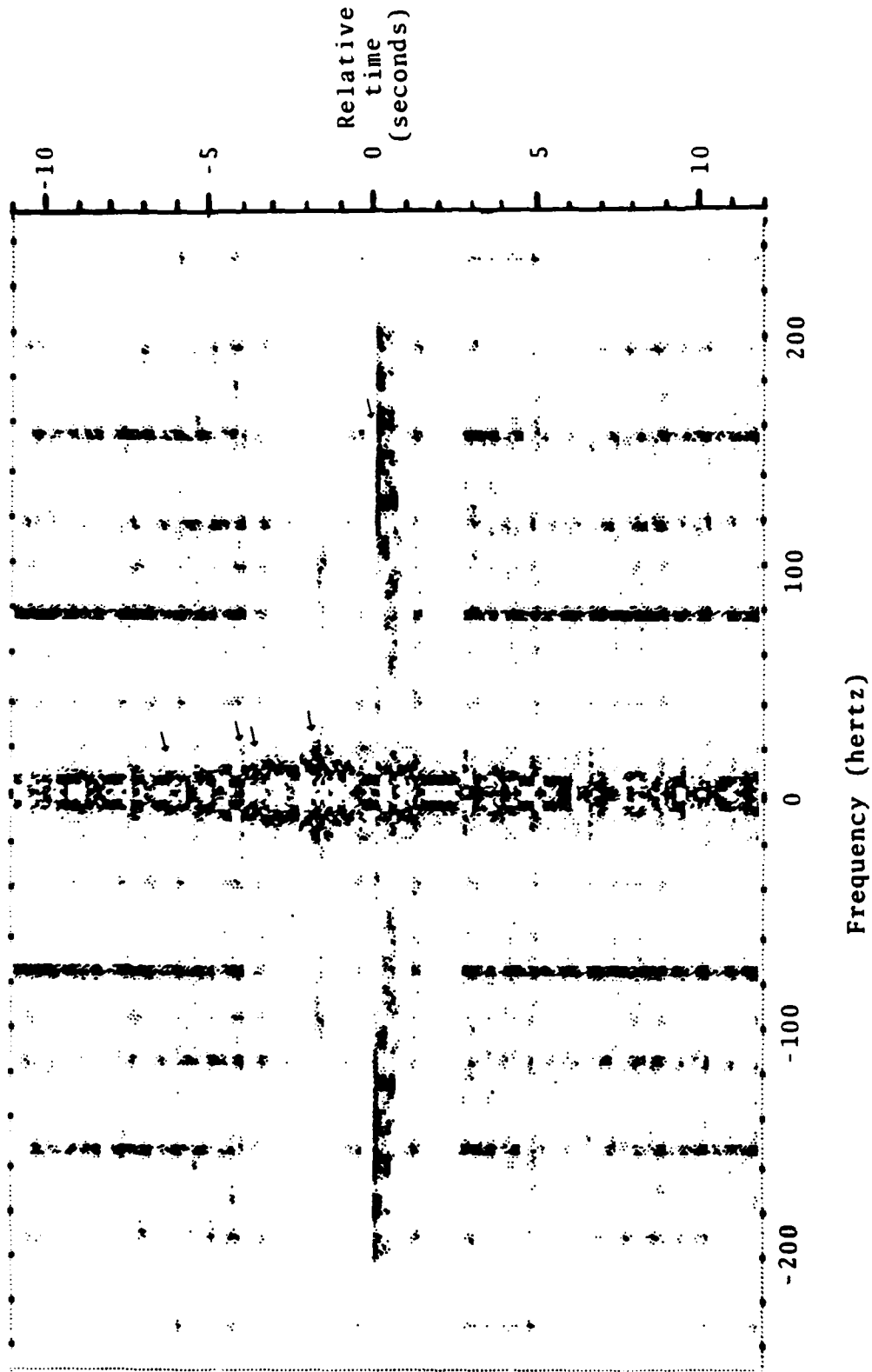
Figure 15d   Spectrogram, Shot A14, Geophone 4X

ENSCO, Inc.   - 65 -
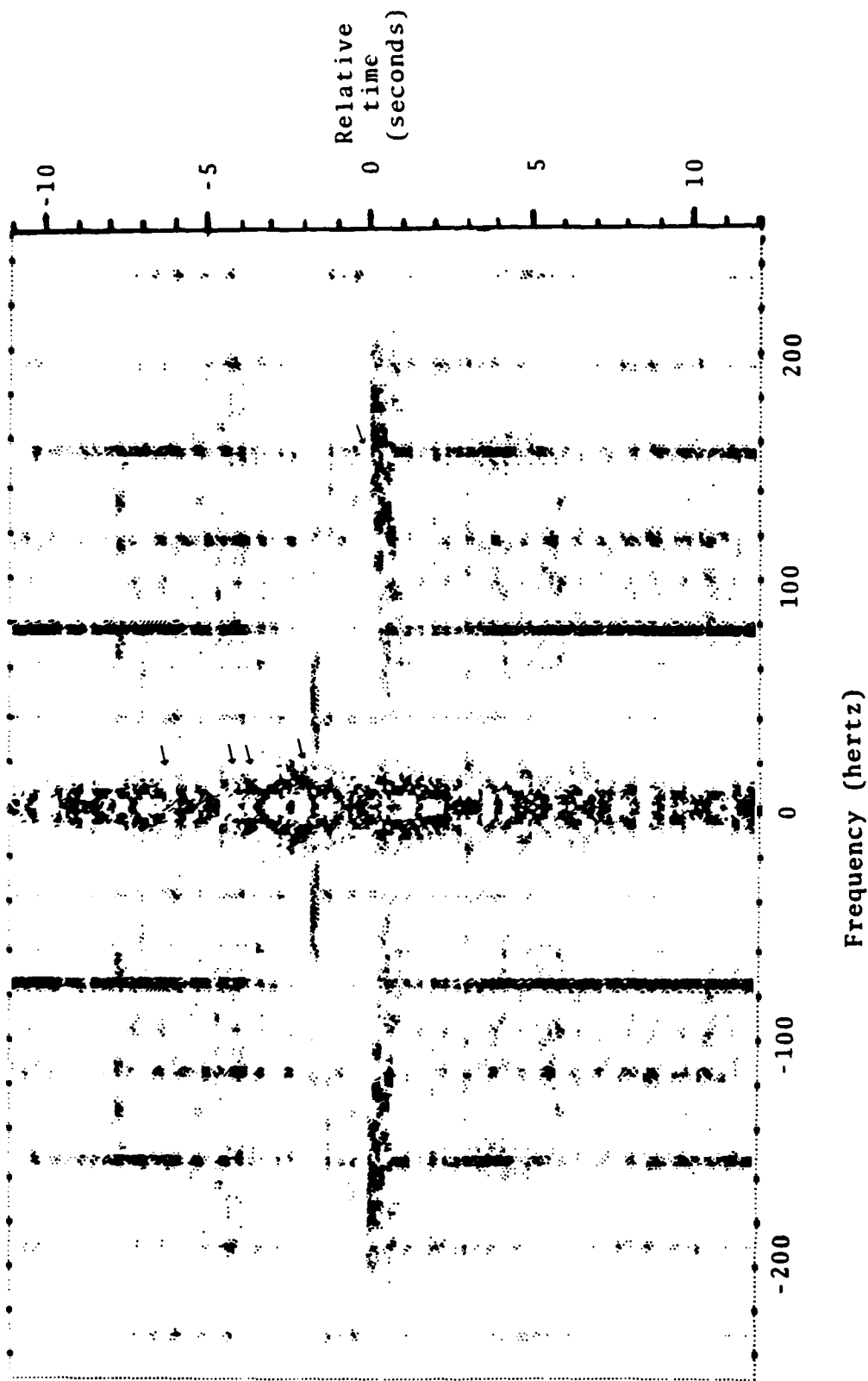
Figure 15e Spectrogram, Shot A14, Geophone 42
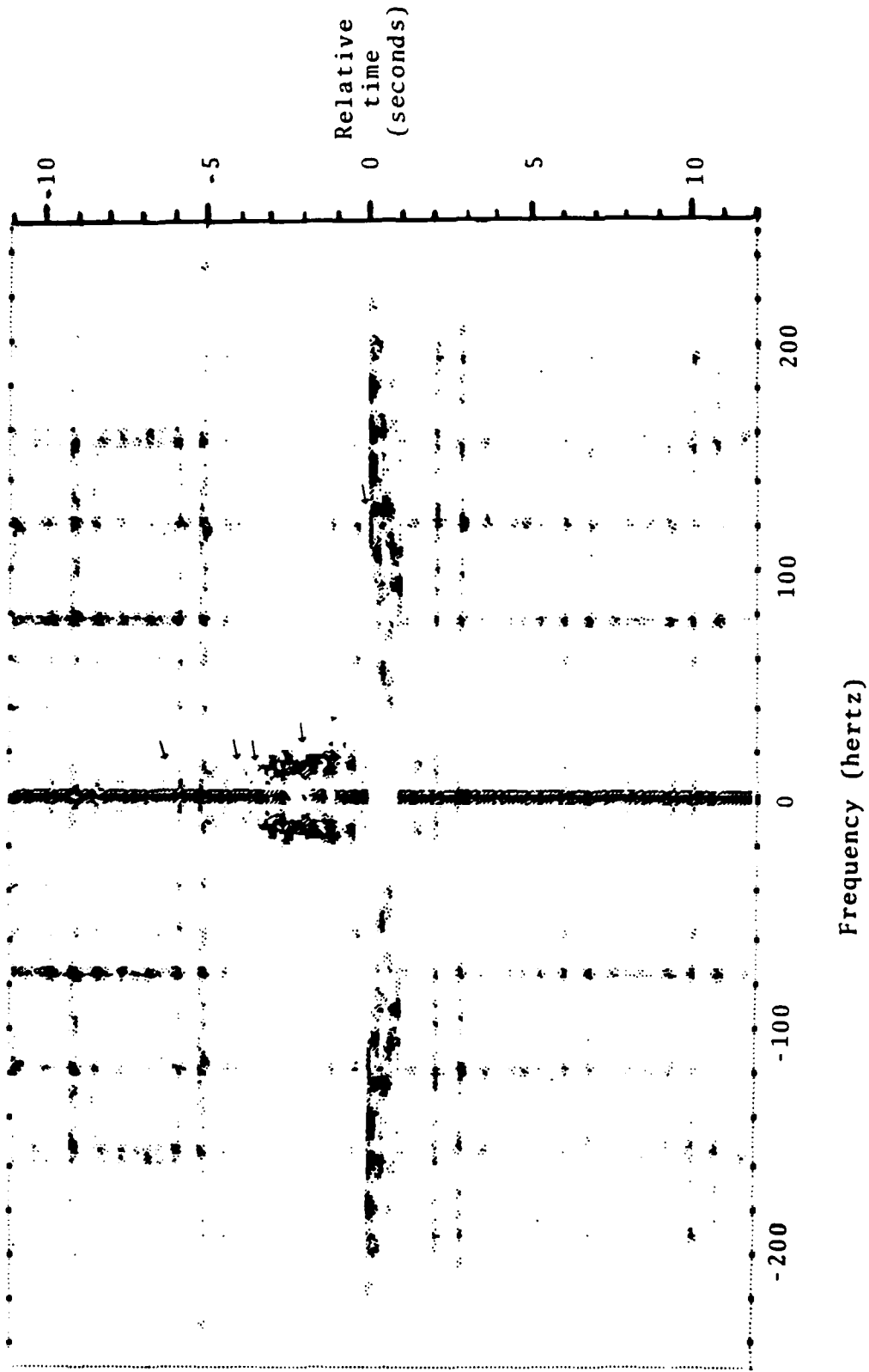
Figure 15f Spectrogram, Shot A14, Hydrophone 4
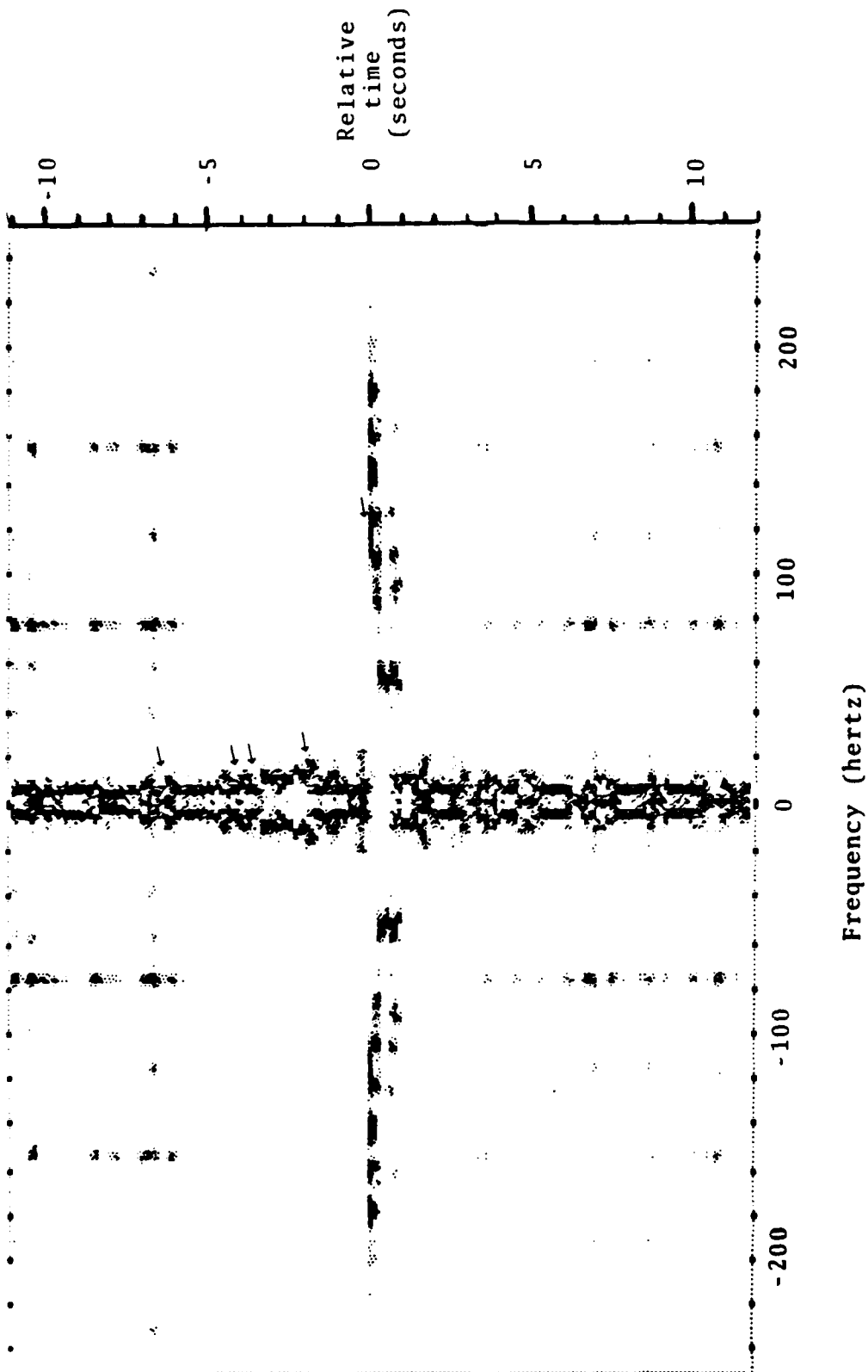
Figure 15g   Spectrogram, Shot A14, Geophone 6X

while the waterwave energy fills the analysis bandwidth
(limited only by the anti-alias digital filter passband).
A moderate degree of frequency diversity characterizes the
different seismic modes. Signals from two seismic modes
are seen to occur nearly simultaneously, and to overlap the
waterwave. In all of the shots, seismic energy can be
observed for a significant time following the waterwave
arrival. Note the strong 5 Hz noise in the geophone spectro-
grams. A 20 Hz modulation is apparent in the waterwave power
spectra, implying the existence of a time delayed arrival.
The approximate time delay of .05 seconds (= 1/20 Hz) corres-
ponds with a 75 meter difference of travel path length. This
could be attributed to a shot self-illumination process, in
which a portion of the hydroacoustic signal reflects off the
ocean-air interface and scatters off the shot bubble. The
multipath could also have been caused by an echo near the
receiving array. However, the phase and spatial consistency
of this spectral modulation favor the former explanation.

Of great concern to this signal processing investigation
was the appearance of very strong harmonic lines in all of
the spectrograms. At first glance, the line structure can
be seen to be quite similar to that generated typically by
marine diesel engines, especially those having a small number
of cylinders. Upon further study, it was found that this
signal occurred simultaneously and highly correlated at all
sensors throughout the data. The implication was that such
a signal had moved vertically, in a plane wavefront, across
the array, an unlikely circumstance. A significant potential

exists that this signal was extraneous to the experimentally acquired signals, having its cause elsewhere. The strength, structure, and persistence of this signal also had adverse effects on subsequent measurements.

2.3 Coherent Crosscorrelation and Beamforming

Signals received at the array, from the selected shots, were analyzed using coherent crosscorrelation techniques, in order to detect and isolate arrival modes, to measure their arrival direction and apparent array transit speed (beam-forming), and to establish input SNR and output processing gain. A discussion of the mechanisms by which the coherent correlation obtains these results is presented first.

The coherent crosscorrelation function, χ, of two digital time series, f and g, is defined here to be

$$\chi(\ell, M, N) \equiv \frac{1}{N} \sum_{i=m}^{M+N-1} f_i^* g_{i+\ell} \qquad (6)$$

where

$$N = \left[\sum_{j=m}^{M+N-1} f_j^* f_j \right]^{\frac{1}{2}} \left[\sum_{k=M-\ell}^{M-\ell+N-1} g_k^* g_k \right]^{\frac{1}{2}} \qquad (7)$$

Subscripts in equations (6) and (7) serve to label elements of the two digital time series. Integration time of the

correlation is equal to $N\delta t$, where δt is the sampling time increment. Start time of the correlation is then $M\delta t$, with respect to the first series, f. The relative shift (search) parameter is ℓ, corresponding with a time shift of $\ell \delta t$.

If the two signals, f and g, have a common signal component, s, then the time series can be redefined by

$$f = s + u; \quad g = s + v, \tag{8}$$

where the relative time shift of s has been set to zero. Introducing equation (8) into equation (6), one has

$$\chi(\ell,M,N) = \frac{1}{N} \sum_{i=M}^{M+N-1} (s_i^* s_{i+\ell} + s_i^* v_{i+\ell} + u_i^* s_{i+\ell} + u_i v_{i+\ell}) \tag{9}$$

If u and v are essentially uncorrelated with s at the time shift which matches the s components (i.e., at zero time delay here), then the zero lag correlation amplitude is found to be, from equation (9),

$$\chi(0,M,N) = \frac{1}{N} \sum_{i=M}^{M+N-1} (s_i^* s_i + u_i^* v_i) \tag{10}$$

Further, if u is essentially uncorrelated with v at zero lag then the correlation amplitude, equation (10), has the value

$$\chi(0,M,N) = \frac{1}{N} \sum_{i=M}^{M+N-1} (s_i^* s_i) \tag{11}$$

where

$$N = [\sum_{j=M}^{M+N-1} (s_j^* s_j + u_j^* u_j)]^{\frac{1}{2}} [\sum_{k=M}^{M+N-1} (s_k^* s_k + v_k^* v_k)]^{\frac{1}{2}} \quad (12)$$

Equation (11) can be rewritten simply as

$$\chi(0,M,N) = \{(1+SNR_f^{-1})^{\frac{1}{2}} (1+SNR_g^{-1})^{\frac{1}{2}}\} \quad (13)$$

where SNR_f, SNR_g refer to the signal-to-noise ratio of the first and second time series, respectively. If both channels have identical SNR, then equation (13) reduces to

$$\chi(0,M,N) = (1 + SNR^{-1})^{-1}$$

or,

$$SNR = \frac{1-\chi}{\chi} \quad (14)$$

by which the SNR can be measured. Gain of the correlation processing is defined here by the deflection ratio, D, where

$$D = \frac{\chi-\bar{\chi}}{\sigma_\chi} \quad (15)$$

In equation (15), $\bar{\chi}$ is the mean value of the correlation function (i.e., of the set of correlation magnitudes for many relative time shifts) and σ_χ is the standard deviation of the correlation function. Equation (15) implies that a gain is achievable only if the common signal correlation magnitude exceeds the mean correlation magnitude. It is

possible to compute, from a theoretical foundation, expected values for the mean correlation amplitude, χ, and the correlation standard deviation, σ_χ, associated with a pair of Gaussian noise input signals. These values can, in turn, be used to quantify the maximum achievable correlation processing gain. Previously, it was shown by Carter (Reference 2) that the magnitude squared correlation probability density function, $\rho_N(u)$, for such input noise, is

$$\rho_N(u) = (N-1)(1-u)^{N-2} \tag{16}$$

where N is the number of (complex) time series points correlated, and $u = \chi^2$. For convenience in notation, it has been assumed that χ represents the modulus (i.e., the magnitude) correlation. From equation (16), it follows that

$$\rho_N(\chi) = 2(N-1)\chi(1-\chi^2)^{N-2} \tag{17}$$

Consequently, from equation (17),

$$\overline{\chi} = \int_0^1 \chi\rho_N(\chi)d\chi$$

$$= \tfrac{1}{2}\sqrt{\pi}\,\Gamma(N)/\Gamma(N+\tfrac{1}{2}) \tag{18}$$

If Stirling's expansion for the gamma function is utilized in equation (18), one finds that

$$\overline{\chi} \approx \tfrac{1}{2}\sqrt{\frac{\pi e}{N}} \; \left(\frac{N}{N+\frac{1}{2}}\right)^{N} \tag{19}$$

However, the expression in braces approaches $1/\sqrt{e}$, for large N, so that equation (19) can be simplified to the form

$$\overline{\chi} \approx \tfrac{1}{2}\sqrt{\frac{\pi}{N}} \tag{20}$$

It is found easily that

$$\overline{\chi^2} \quad \int_0^1 \chi^2 \rho(\chi)\,d\chi = \frac{1}{N} \tag{21}$$

The standard deviation, τ_χ, can be obtained from equations (20) and (21)

$$\sigma_\chi \approx \sqrt{\frac{1}{N}\left(1-\frac{\pi}{4}\right)} \tag{22}$$

Equations (20) and (22) can be used to determine the maximum deflection ratio, D_m,

$$D_m = \frac{1-\overline{\chi}}{\sigma_\chi} \approx \left(1-\tfrac{1}{2}\sqrt{\frac{\pi}{N}}\right) \Big/ \sqrt{\frac{1}{N}\left(1-\frac{\pi}{4}\right)} \tag{23}$$

In the present investigation, correlation lengths of 64-200 points were used, so that the expected ranges of correlation output parameters were

$$.06 < \bar{\chi} < .11$$

$$.03 < \sigma_\chi < .06 \tag{24}$$

$$24dB < D_m < 29dB$$

Coherent crosscorrelation also served as a coherent beamformer and velocity filter. To see this, consider the geometric array configuration shown in Figure 1b. If the incident signal, indicated by the arrow in the Figure, traverses the array as a plane wave, then the arrival angles are related to the arrival time delays by the expression

$$d_{ij}\cos\theta_{ij} = c\tau_{ij} = r_j - r_i \tag{25}$$

In equation (25), c is the apparent transit speed, τ_{ij} is the measured relative arrival time delay as observed between two sensors, i and j; and r_k is the range from the (apparent) source to sensor k.

Since

$$\theta_{13} = \theta_{12} - \phi,$$

then

$$\cos\theta_{13} = \cos\phi\cos\theta_{12} + \sin\phi\sin\theta_{12} \tag{26}$$

If equation (25), for i = 1 and j = 2, is introduced into
equation (26), one finds that

$$\sin\theta_{12} = \frac{c}{\sin\phi} \left[\frac{\tau_{13}}{d_{13}} - \frac{\tau_{12}}{d_{12}} \cos\phi\right] \tag{27}$$

Thus, from equations (25) and (27),

$$\tan\theta_{12} = \frac{1}{\sin\phi} \left[\left(\frac{d_{12}}{d_{13}}\right) \left(\frac{\tau_{13}}{\tau_{12}}\right) - \cos\phi\right] \tag{28}$$

Equations (25), (27), and (28) demonstrate that a group
of coherently related time delays can be used to determine
the apparent propagation direction and speed of a mode which
traverses an array. It is observed, from equation (25), that

$$\tau_{ij} + \tau_{jk} = \tau_{ik} \tag{29}$$

for any coherent signal which might traverse the array.
Equation (29) links multiple pairwise correlation output
data together, coherently. Note that the derivations here
apply, except of course where $\phi = 180°$ (linear array), to
any collection of sensors selected from the array.

Two types of display were utilized to present the raw
correlation output. One, the density plot (Figures 16-19),
is analogous to the spectrogram density plot. Here, the
horizontal axis is a measure of relative time delay, rather
than of frequency. Since the correlation function was nor-
malized, its display was globally, rather than locally,
scaled. Also, the density levels were derived from the

correlation modulus, rather than from the magnitude modulus squared. A variety of A-line correlation format displays are included in Figures 20-26, to illustrate detailed behavior of the coherent correlation.

Correlation peaks were selected from the data for signals arriving from the direction of the shots. Correlation peak occurrence times were used to identify the respective seismic modes. After this selection process, the apparent propagation speed of the modes were calculated. SNR and correlation gain parameters were also developed from the selected events. These results are shown in Tables 5 and 6. The bulk of the seismic parameters reported in Tables 5 and 6. were derived from x-axis signals, although the z-axis signals yielded similar estimates (as is evidenced by the z-axis correlation density plots). Regrettably, the geophone number 6 digitized time series were found to be saturated at maximum negative amplitude. This seriously hindered the independent analysis of vertical geophone array signals in terms of beamforming and of related calculations.

Hydrophone results, shown in the Tables, were derived principally from hydrophone sensors number 4 and 5. Since our method of computing the digital crosscorrelation function had a precision limited by the sample time increment, it was found that estimates for propagation direction and speed, based on the small hydrophone array, were relatively coarse compared with the geophone-based estimates. For this reason, the hydrophone measurements were comparatively less accurate. All of the results in Tables 5 and 6 represent the best data obtained using several different sets of correlation processing parameters.

TABLE 5
CORRELATION PROCESSING GAIN AND SIGNAL-TO-NOISE LEVELS

Shot Number	Mode	Deflection Ratio (dB) 5Z/4Z	5X/4X	*Signal-to-Noise Ratio (dB)* 5X/6X	5H/4H
A27	$P_1P_2P_1$	11, *6*	9, *1*	12, *13*	*8*, *17*
	$P_1S_2P_1$	11, *14*	6, *15*	6, *13*	9, *38*
	$S_1S_2S_1$	11, *14*	5, *16*	6, *13*	9, *38*
	P_1	10, *2*	--	1, *0*	6, *34*
	Water	18, *10*	17, *8*	18, *12*	21, *35*
A25	$P_1P_2P_1$	10, *0*	9, *10*	11, *13*	9, *10*
	$P_1S_2P_1$	10, *9*	9, *6*	9, *20*	8, *26*
	$S_1S_2S_1$	6, *9*	3, *1*	9, *15*	9, *30*
	P_1	8, *14*	--	--	10, *31*
	Water	18, *12*	15, *6*	17, *14*	18, *44*
A20	$P_1P_2P_1$	--	--	--	--
	$P_1S_2P_1$	12, *5*	10, *7*	8, *10*	10, *6*
	$S_1S_2S_1$	11, *6*	8, *7*	8, *8*	7, *20*
	P_1	12, *10*	10, *9*	10, *6*	10, *14*
	Water	18, *8*	17, *5*	17, *11*	20, *38*
A14	$P_1P_2P_1$	--	--	1, *-1*	--
	$P_1S_2P_1$	8, *1*	--	--	--
	$S_1S_2S_1$	2, *5*	--	--	--
	P_1	10, *8*	--	--	6, *20*
	Water	18, *3*	16, *2*	20, *14*	19, *34*

TABLE 6

DERIVED PROPAGATION SPEEDS

| Mode	Travel Time	Correlation	
	Speed (km/sec)	Speed (km/sec)	Direction (deg)
P_2	3.28 ± .16	3.33 ± .67	229 ± 6
S_2	2.34 ± .06	2.56 ± .54	234 ± 6
P_1	1.74 ± .02	--	--
Water Wave	--	1.57 ± .14	228 ± 3
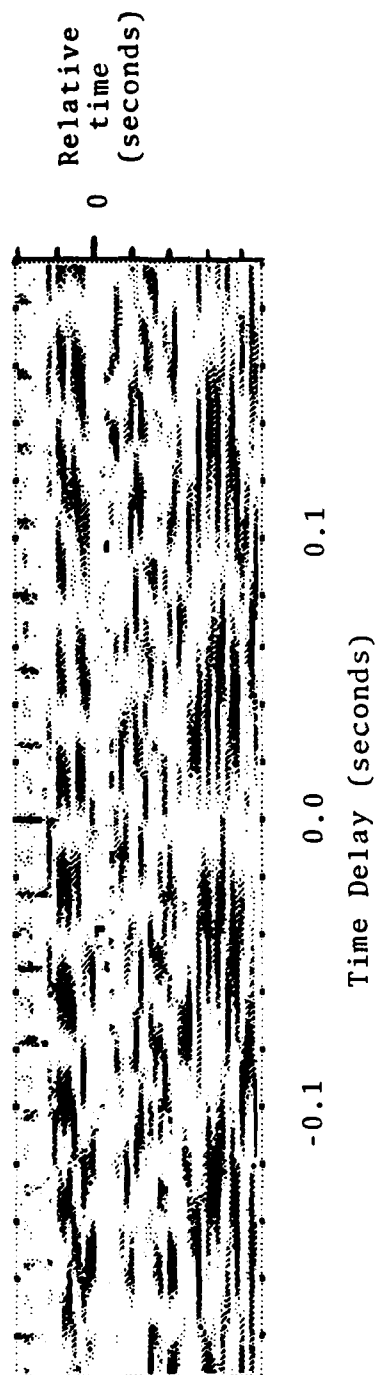
Figure 16a   Correlation Density Display, Shot A27,
              Geophones 4X vs. 5X
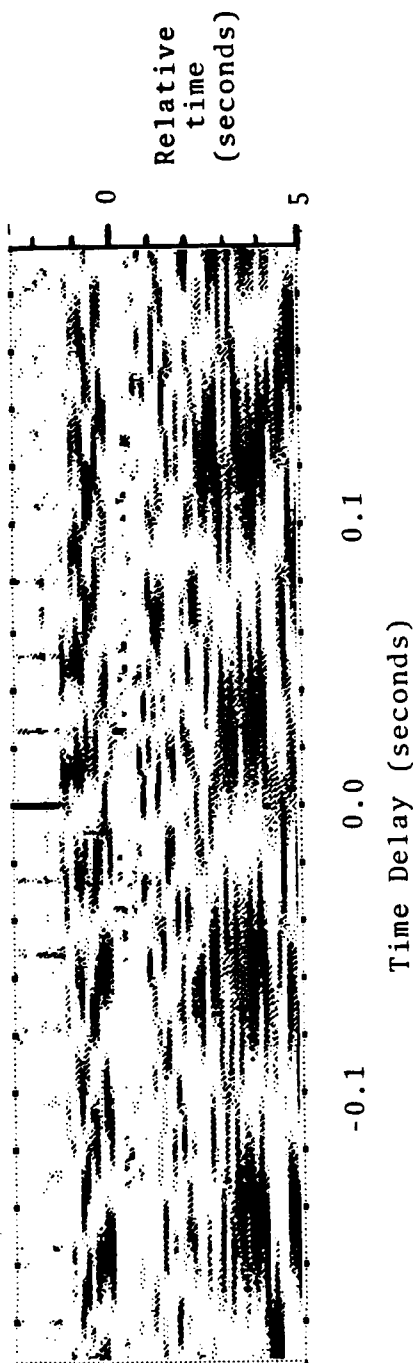
Figure 16b   Correlation Density Display, Shot A27, Geophones 5X vs. 6X
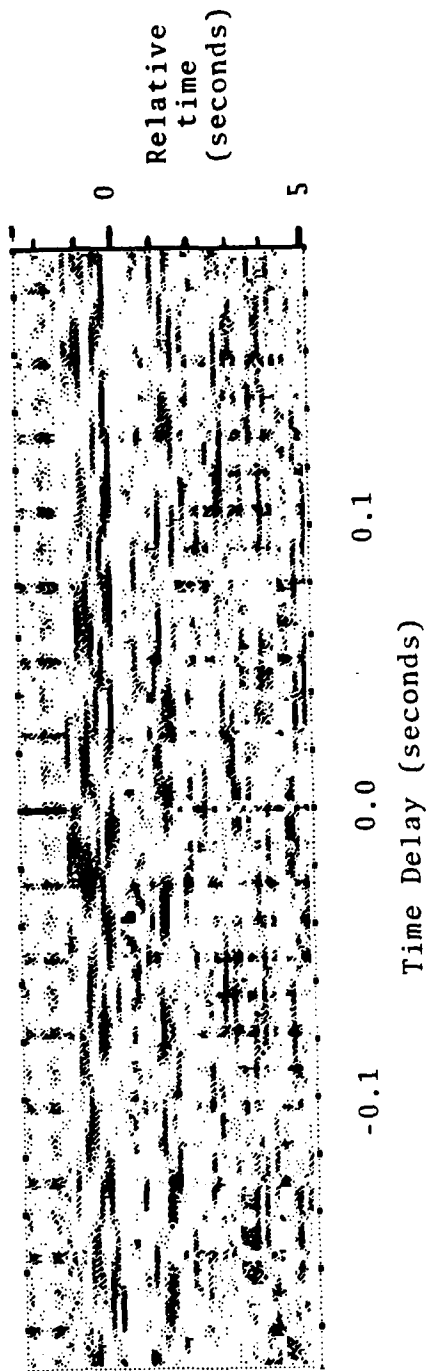
Figure 16c Correlation Density Display, Shot A27, Geophones 4Z vs. 5Z
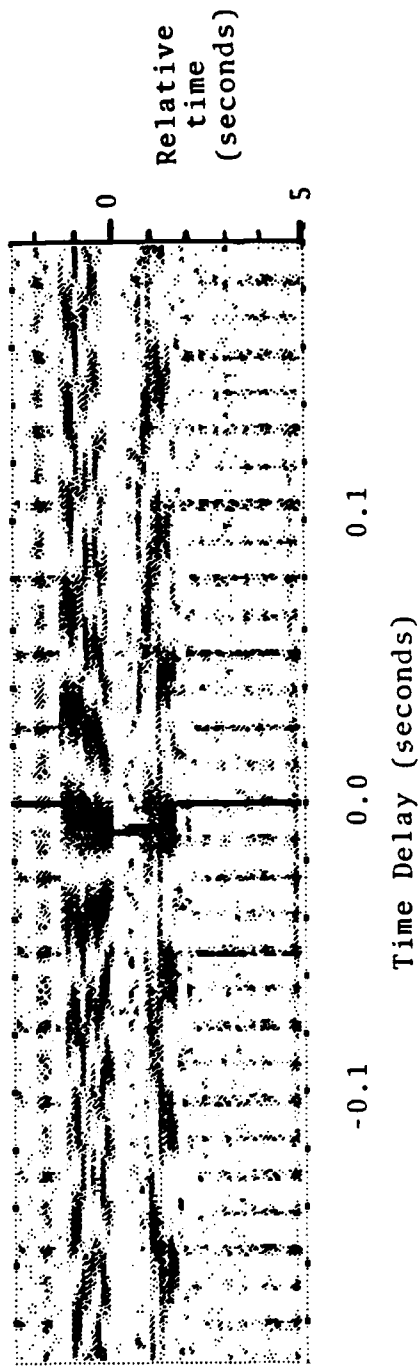
Figure 16d Correlation Density Display, Shot A27, Hydrophones 4 vs. 5

Figure 16e Correlation Density Display, Shot A27, Hydrophone 4 vs. Geophone 5X
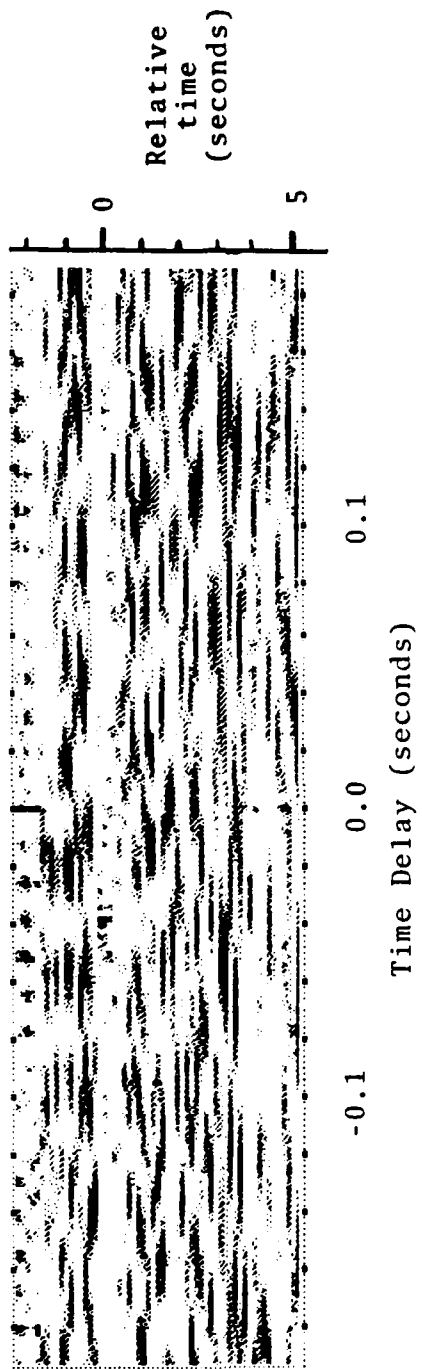
Figure 17a Correlation Density Display, Shot A25, Geophones 4X vs. 5X
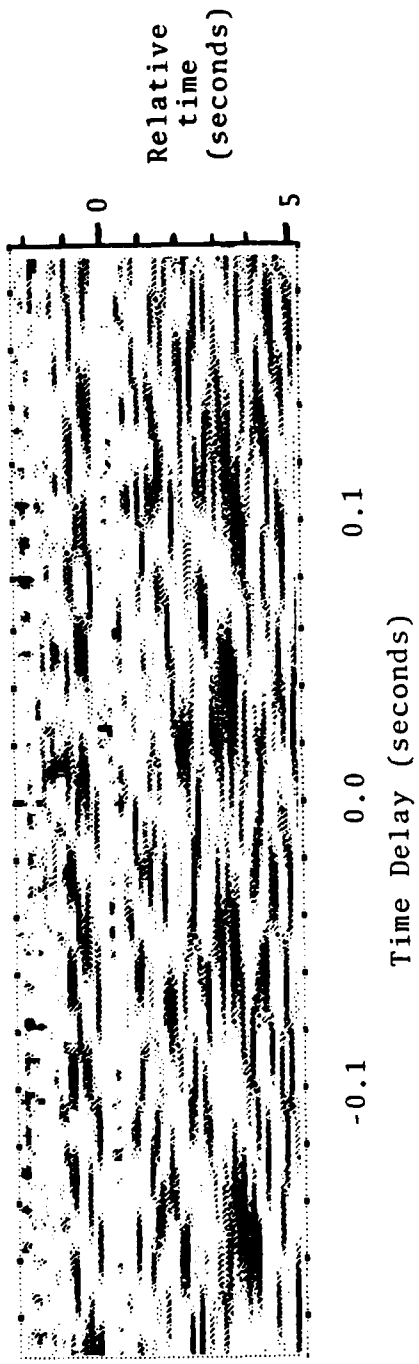
Figure 17b Correlation Density Display, Shot A25,
Geophones 4X vs. 5X
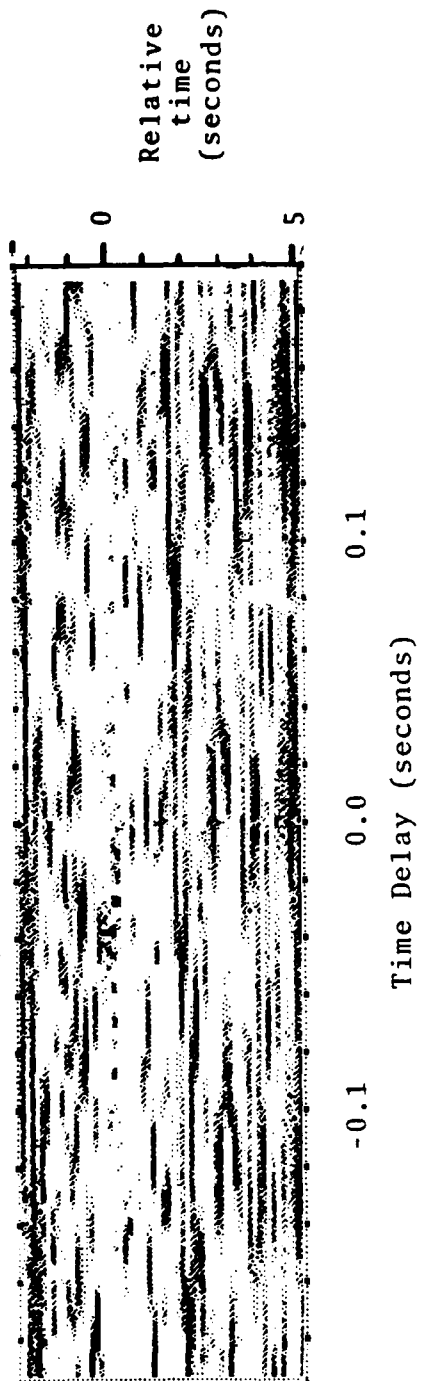
Figure 17c Correlation Density Display, Shot A25,
Geophones 4Z vs. 5Z
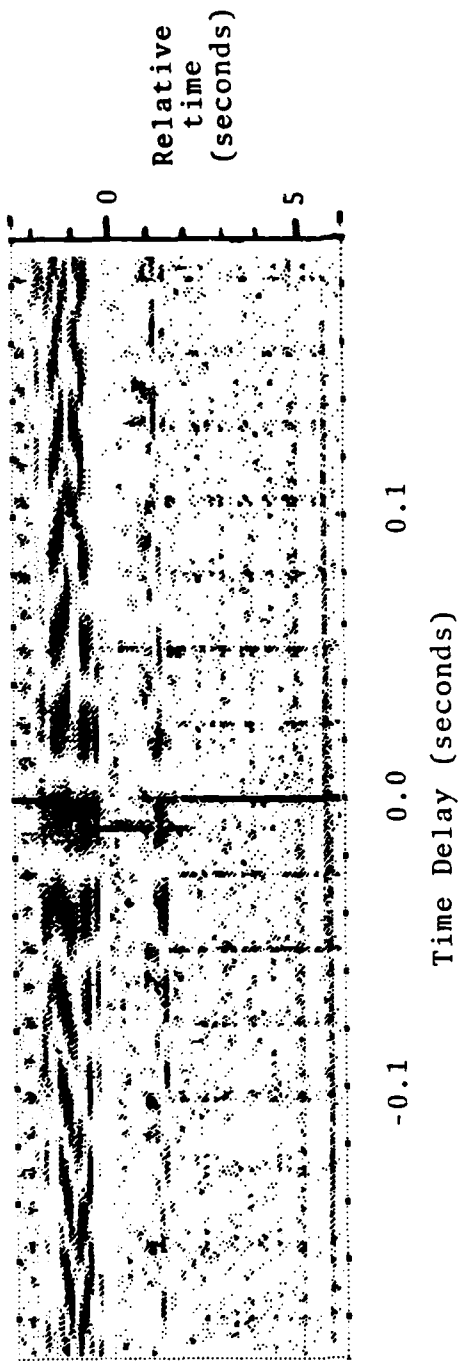
Figure 17d   Correlation Density Display, Shot A25, Hydrophones 4 vs. 5
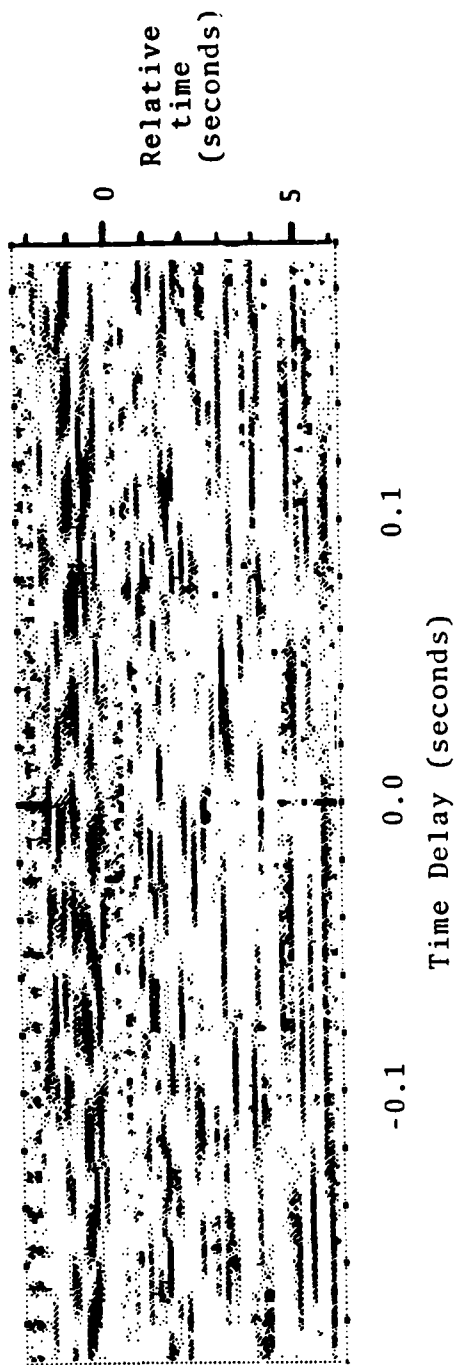
Figure 17e   Correlation Density Display, Shot A25, Hydrophone 4 vs. Geophone 5X
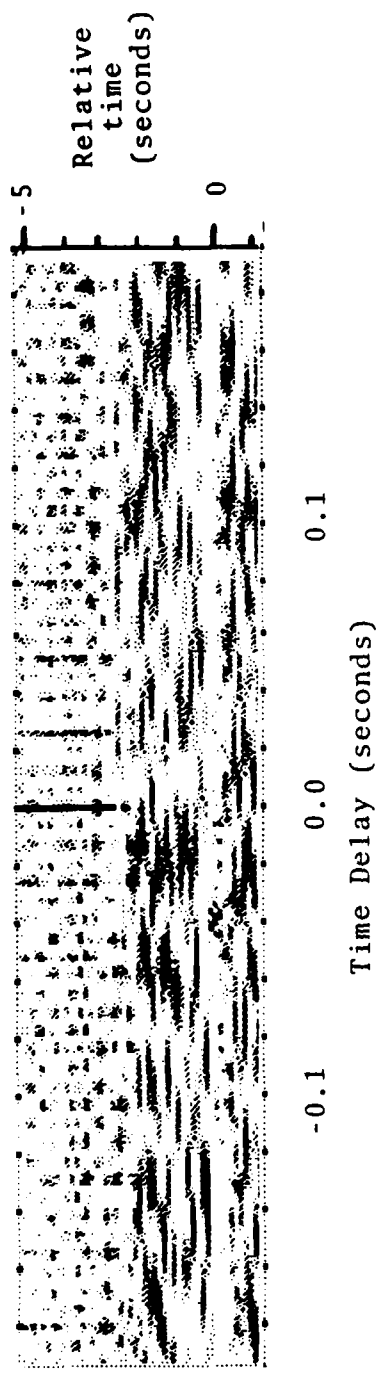
Figure 18a Correlation Density Display, Shot A20, Geophones 4X vs. 5X
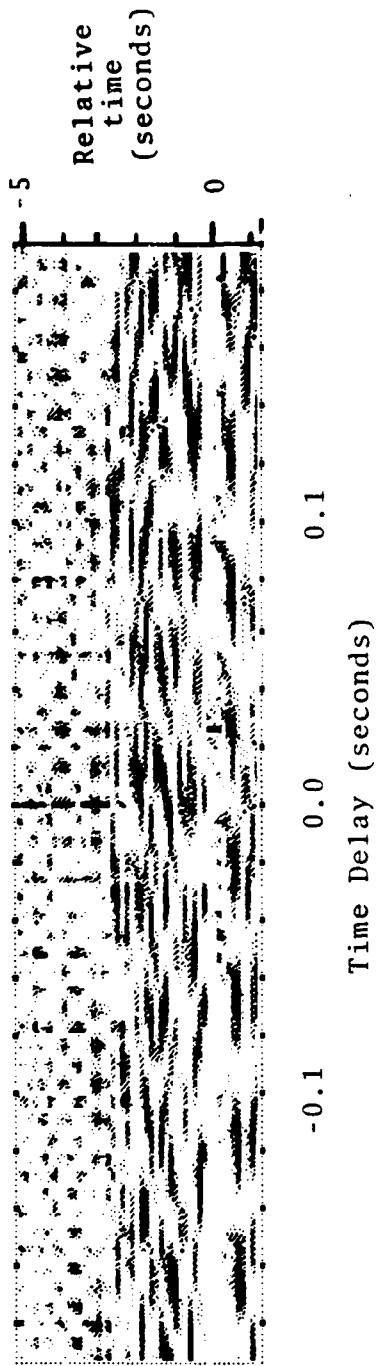
Figure 18b Correlation Density Display, Shot A20,
Geophones 5X vs. 6X
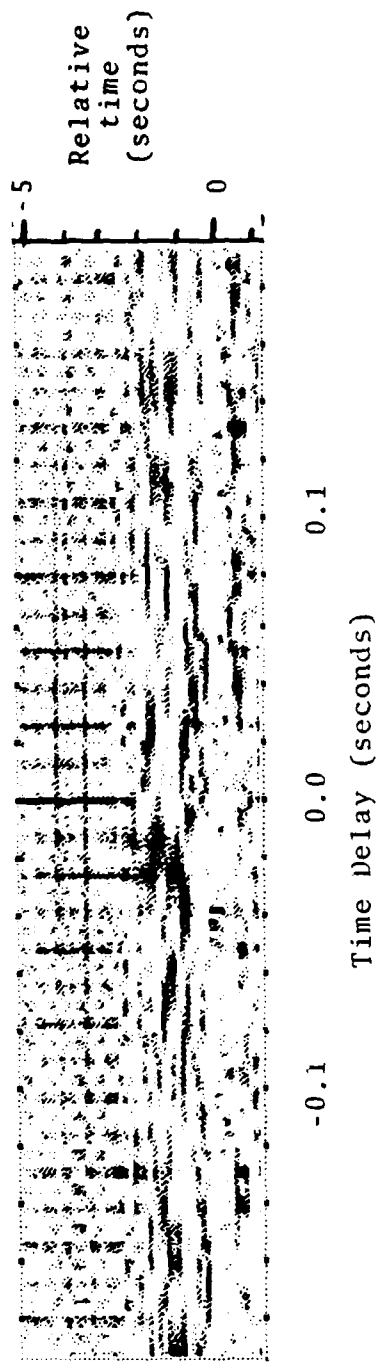
Figure 18c   Correlation Density Display, Shot A20, Geophones AZ vs. 5Z
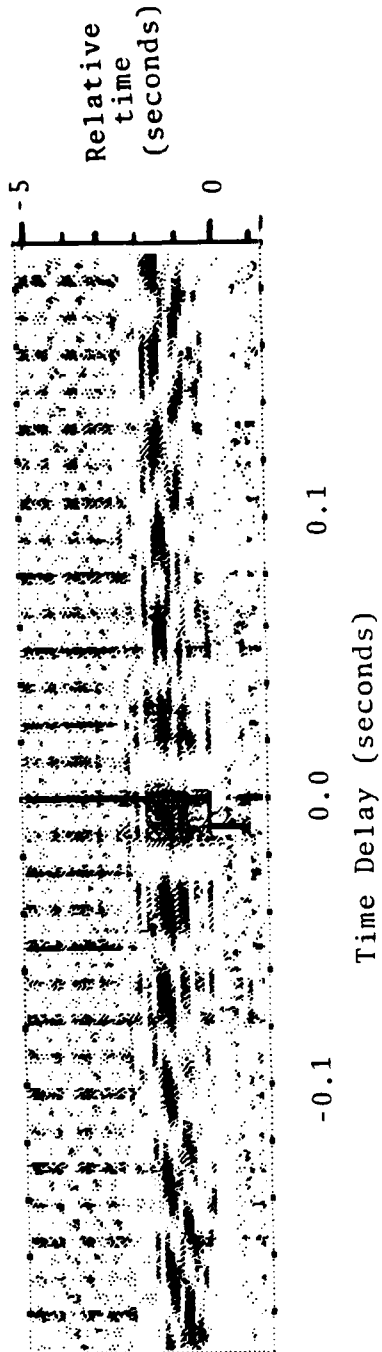
Figure 18d Correlation Density Display, Shot A20,
Hydrophones 4 vs. 5
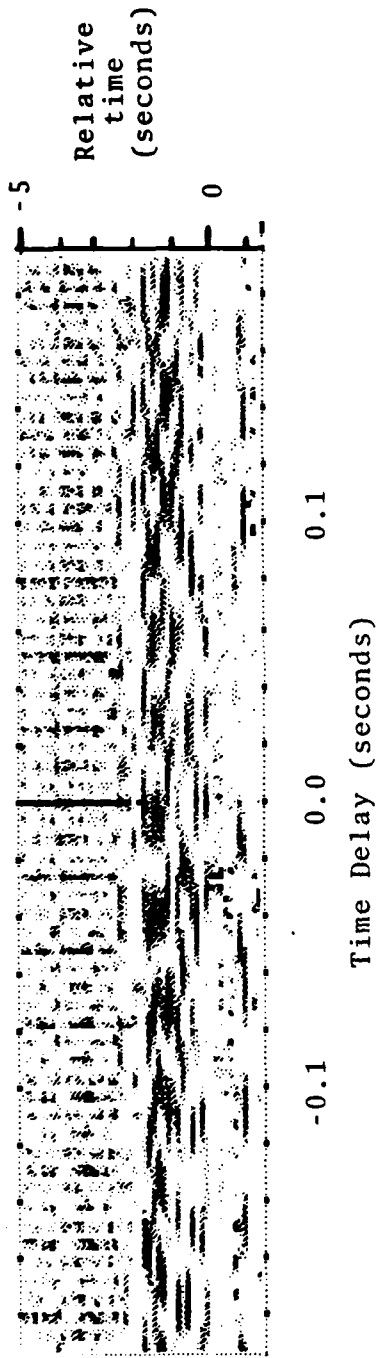
Figure 18e   Correlation Density Display, Shot A20,
Hydrophone 4 vs. Geophone 5X
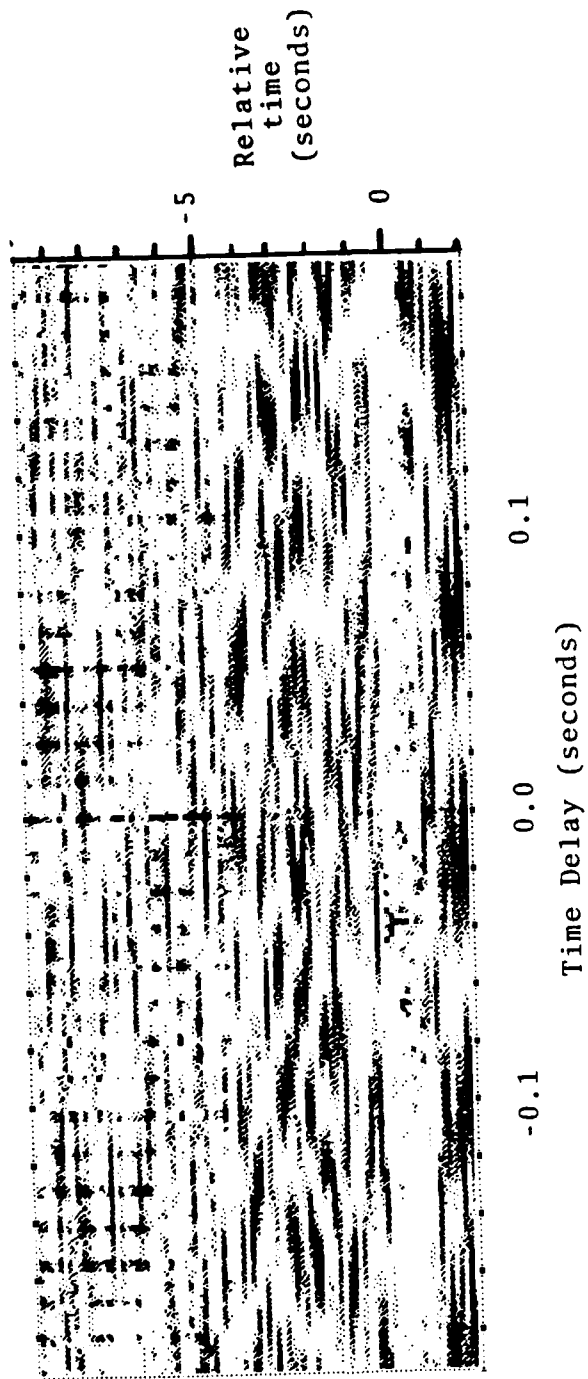
Figure 19a   Correlation Density Display, Shot A14,
Geophones 4X vs. 5X
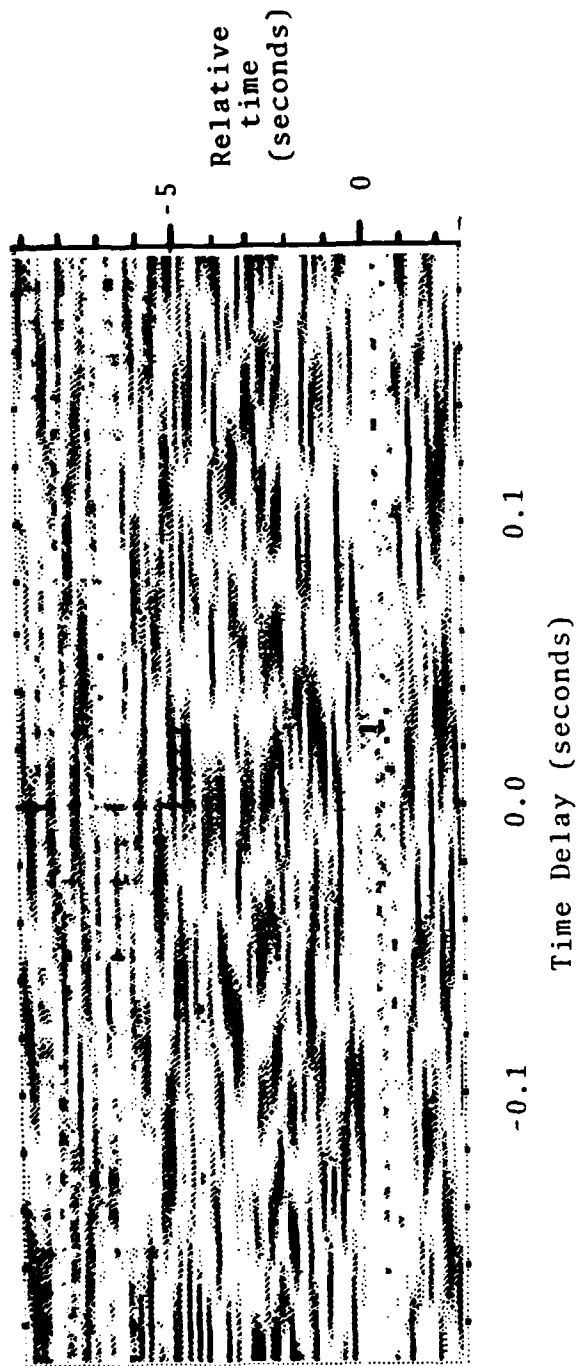
Figure 19b Correlation Density Display, Shot A14,
Geophones 5X vs. 6X

ENSCO, Inc.   - 96 -
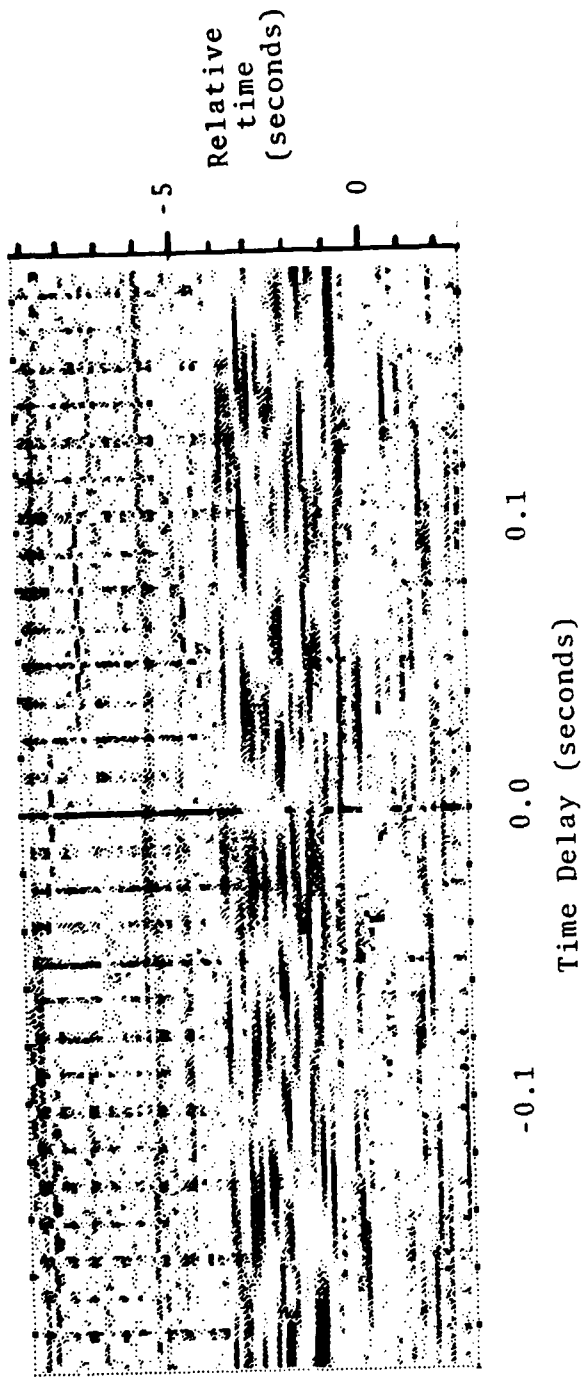
Figure 19c   Correlation Density Display, Shot A14,
Geophones 4Z vs. 5Z
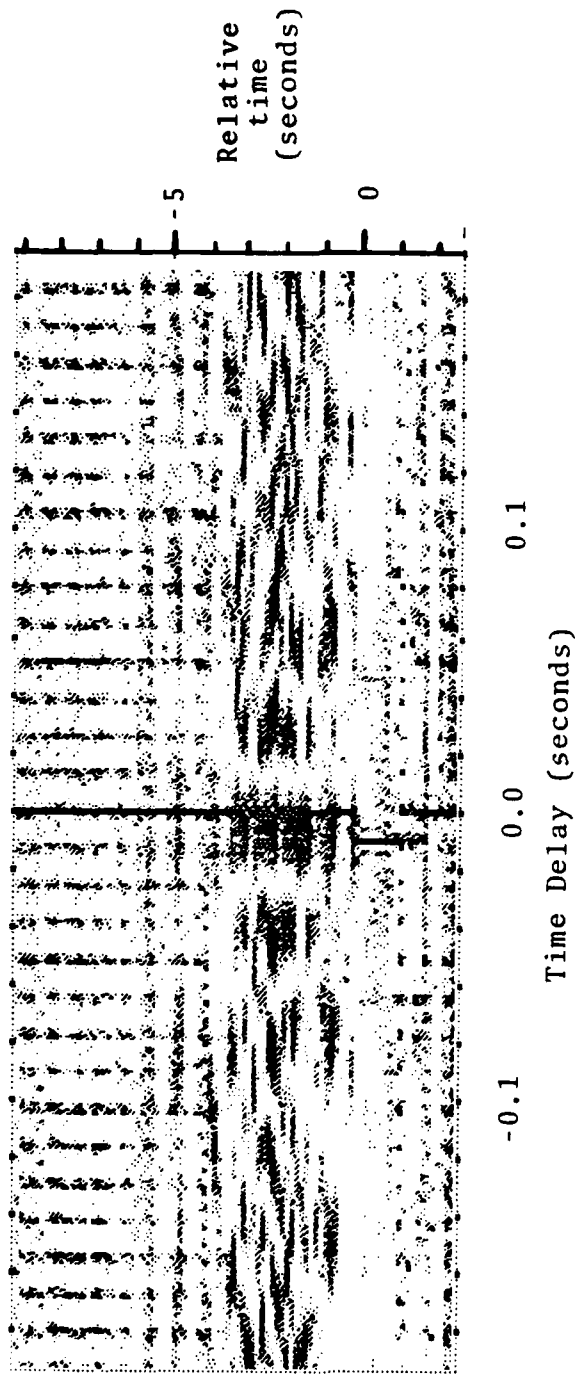
Figure 19d   Correlation Density Display, Shot A14, Hydrophone 4 vs. 5

ENSCO, Inc.

- 98 -
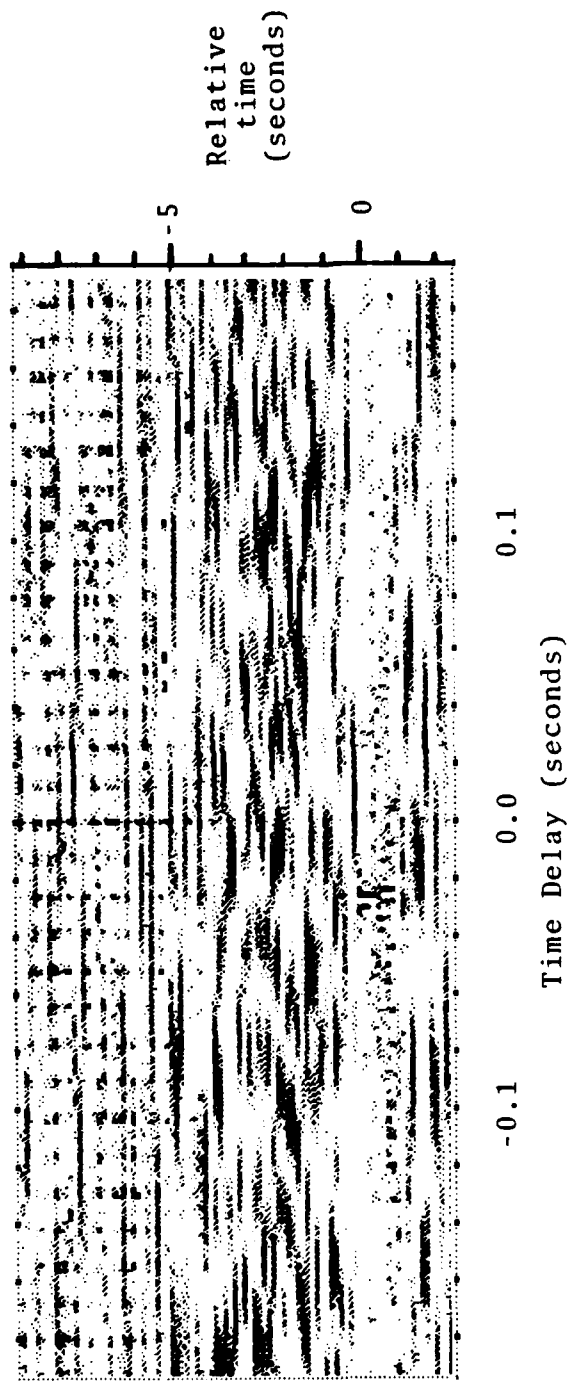
Figure 19e Correlation Density Display, Shot A14, Hydrophone 4 vs. Geophone 5X
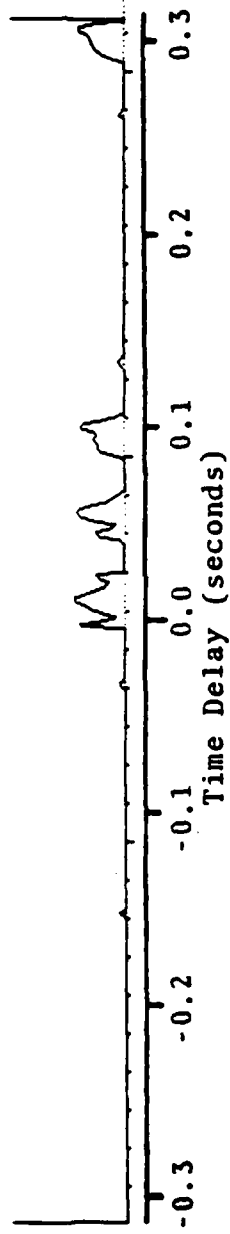
Figure 20a Correlation Function, Shot A27, Geophones 5X vs. 4X, Mode $P_1P_2P_1$
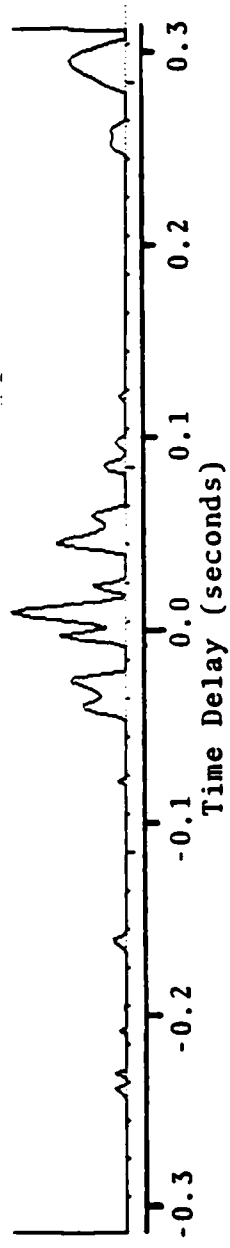
Figure 20b   Correlation Function, Shot A27, Geophones 5X vs. 6X, Mode $P_1P_2P_1$
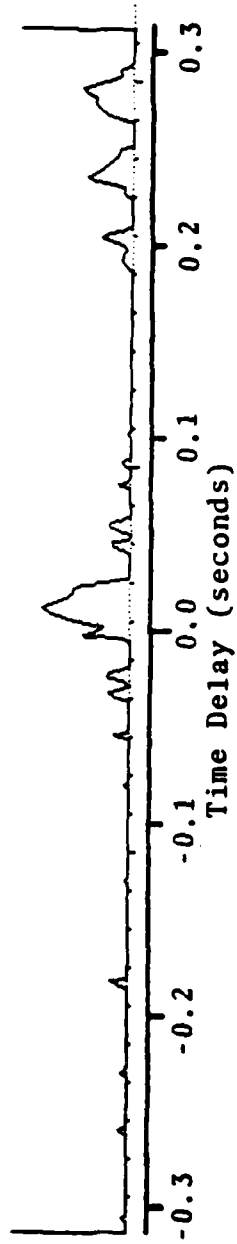
Figure 20c Correlation Function, Shot A27, Geophones 5X vs. 4X, Mode $P_1P_2P_1$
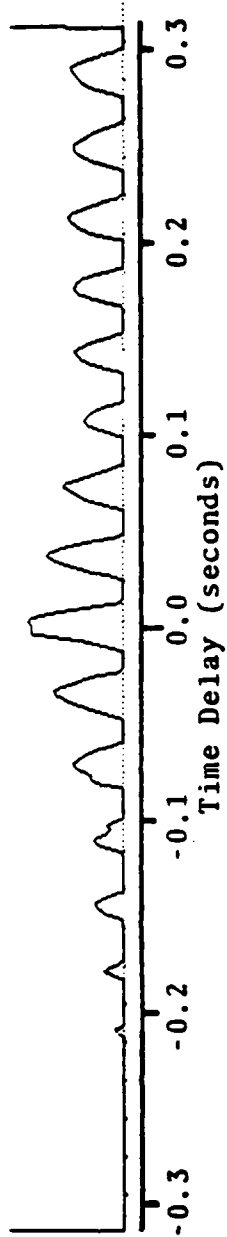
Figure 20d Correlation Function, Shot A27, Hydrophones 5 vs. 4, Mode $P_1P_2P_1$
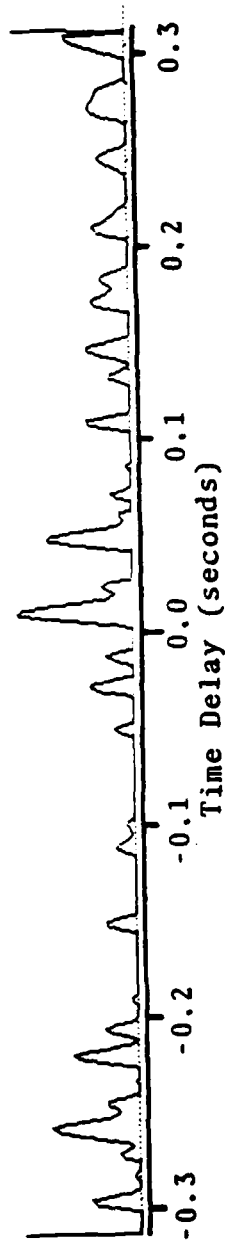
Figure 21a   Correlation Function, Shot A25, Geophones 5X vs. 6X, Mode $P_1S_2P_1$
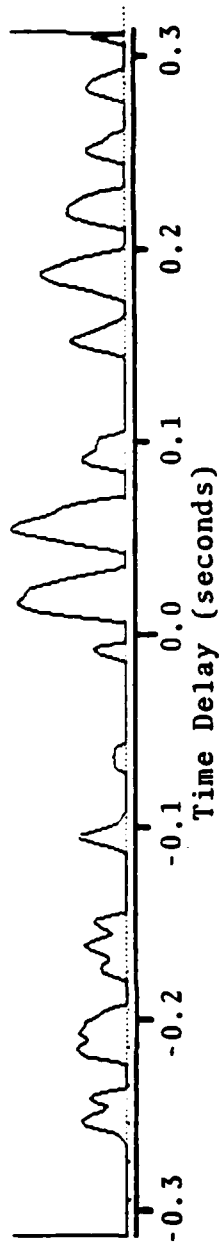
Figure 21b Correlation Function, Shot A25, Geophones 5X vs. 4X, Mode $P_1S_2P_1$
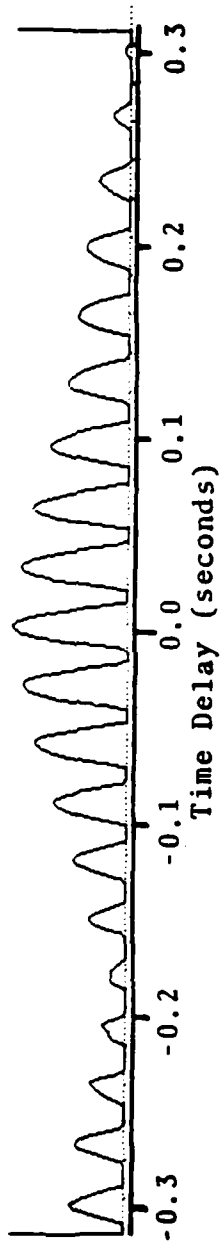
Figure 21c Correlation Function, Shot A25, Hydrophones 5 vs. 4, Mode $P_1S_2P_1$
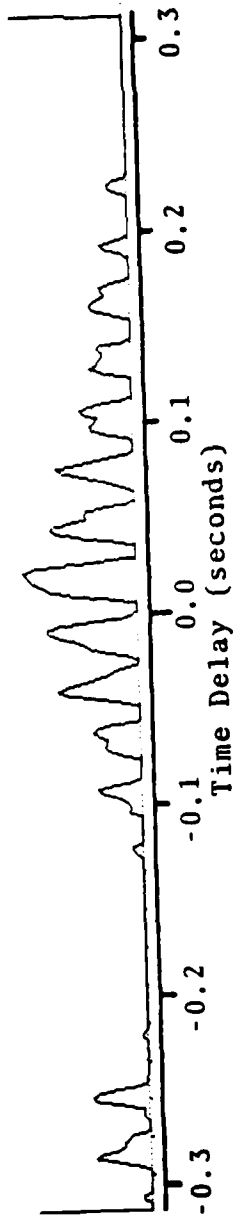
Figure 21d   Correlation Function, Shot A25, Geophones 5Z vs. 4Z, Mode $P_1S_2P_1$
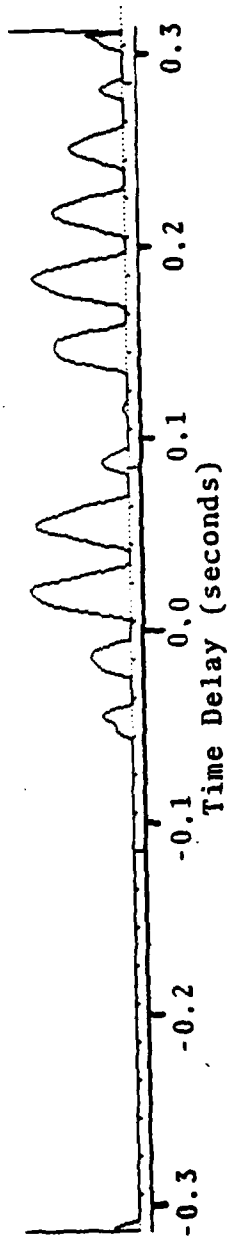
Figure 22a Correlation Function, Shot A20, Geophones 5X vs. 4X,
Mode $S_1S_2S_1$
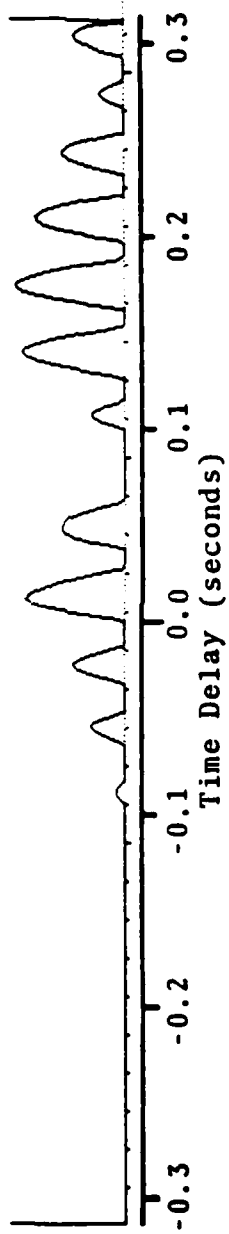
Figure 22b   Correlation Function, Shot A20, Geophones 5X vs. 6X, Mode $S_1 S_2 S_1$
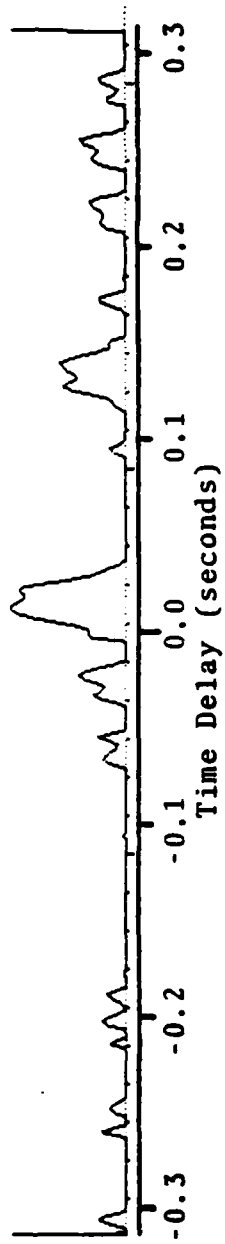
Figure 22c   Correlation Function, Shot A20, Geophones 5Z vs. 4Z, Mode $S_1S_2S_1$
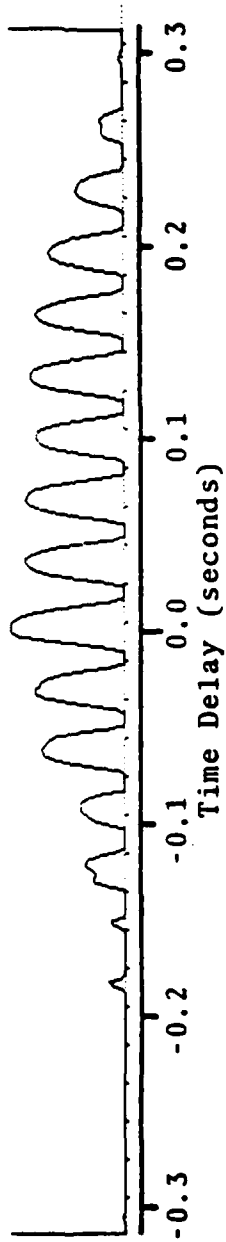
Figure 22d   Correlation Function, Shot A20, Hydrophones 5 vs. 4, Mode $S_1S_2S_1$
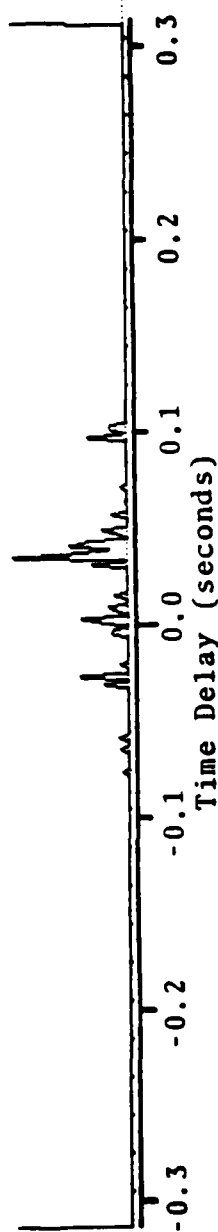
Figure 23a   Correlation Function, Shot A27, Geophones 5X vs. 4X, Water Wave
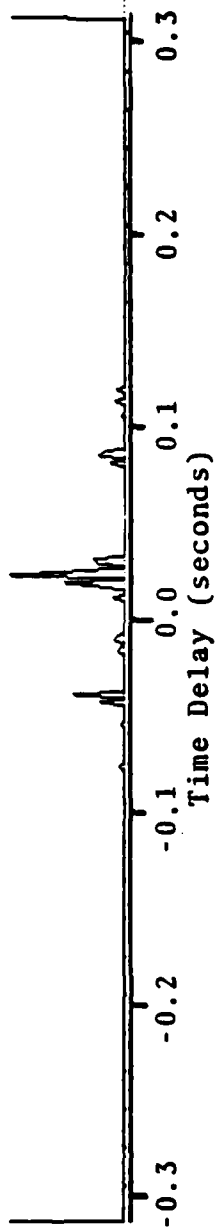
Figure 23b   Correlation Function, Shot A27, Geophones 5X vs. 6X, Water Wave
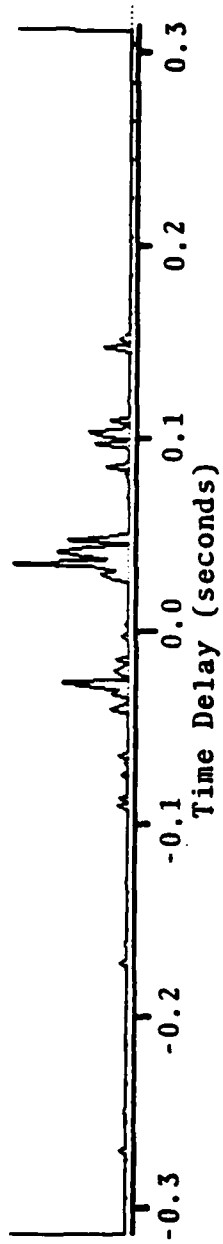
Figure 23c   Correlation Function, Shot A27, Geophones 5Z vs. 6Z, Water Wave
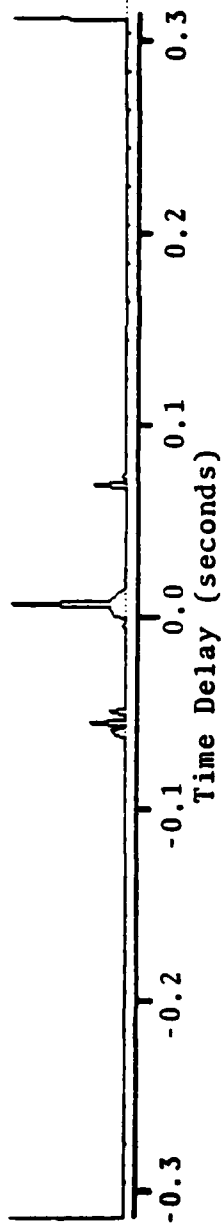
Figure 23d Correlation Function, Shot A27, Hydrophones 5 vs. 4, Water Wave
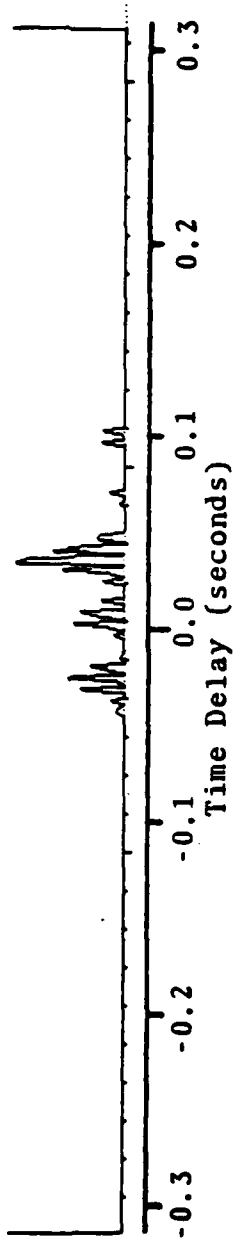
Figure 24a Correlation Function, Shot A25, Geophones 5X vs. 4X, Water Wave
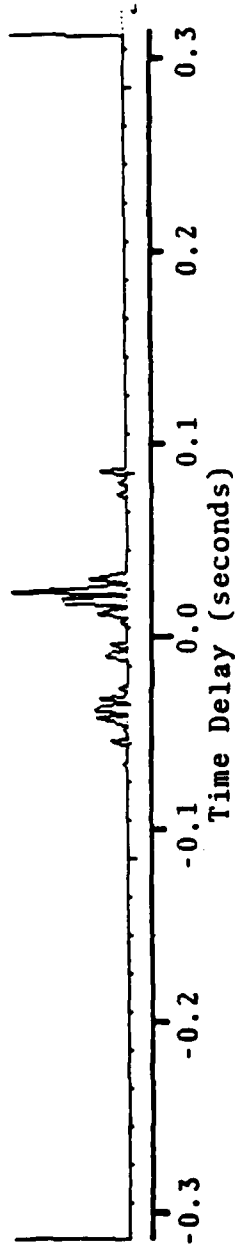
Figure 24b Correlation Function, Shot A25, Geophones 5X vs. 6X,
Water Wave
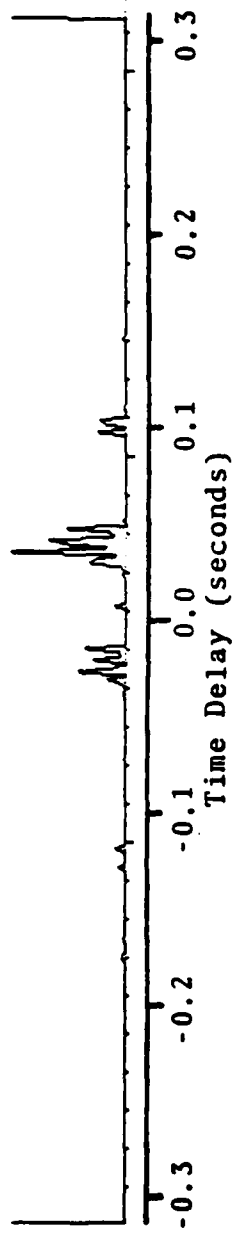
Figure 24c Correlation Function, Shot A25, Geophones 5Z vs. 6Z, Water Wave
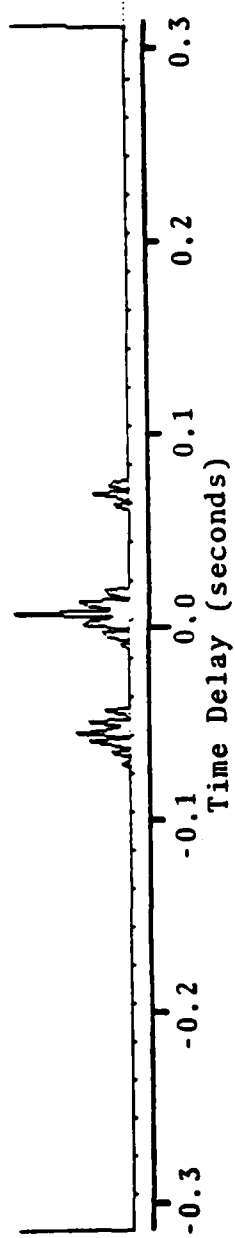
Figure 24d Correlation Function, Shot A25, Hydrophones 5 vs. 4, Water Wave
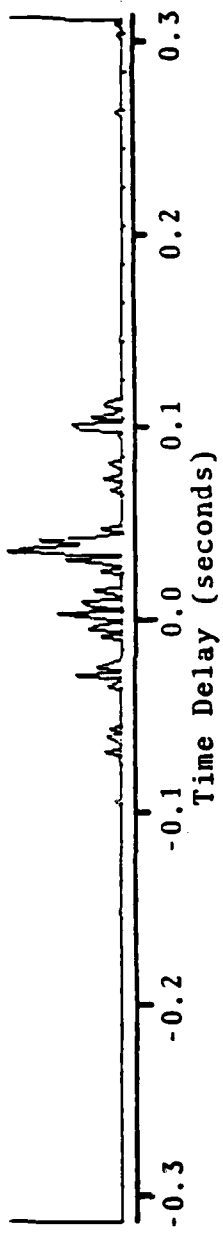
Figure 25a Correlation Function, Shot A20, Geophones 5X vs. 4X, Water Wave
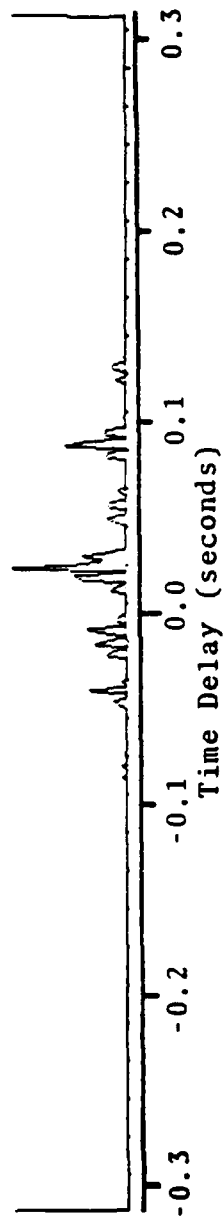
Figure 25b   Correlation Function, Shot A20, Geophones 5X vs. 6X, Water Wave

Time Delay (seconds)
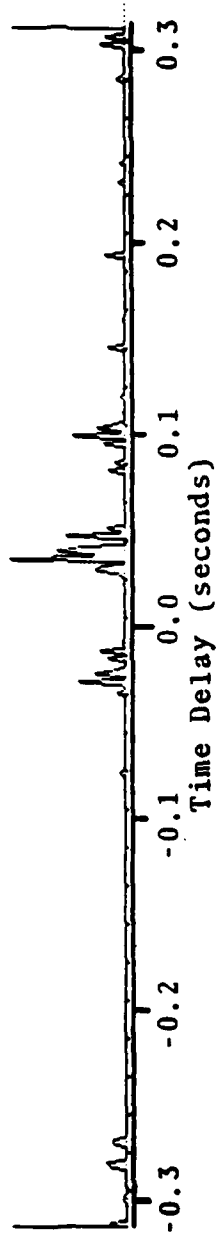
Figure 25c   Correlation Function, Shot A20, Geophones 5Z vs. 4Z,
Water Wave
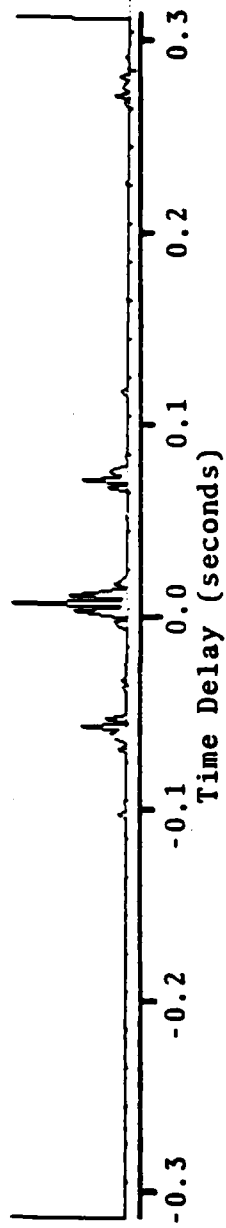
Figure 25d Correlation Function, Shot A20, Hydrophones 5 vs. 4, Water Wave
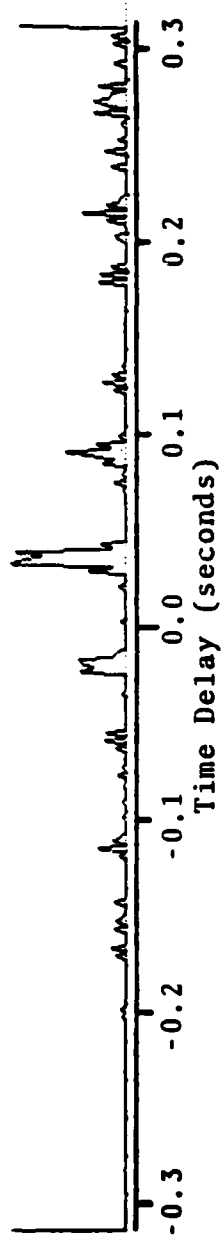
Figure 26a Correlation Function, Shot A14, Geophones 5X vs. 4X, Water Wave
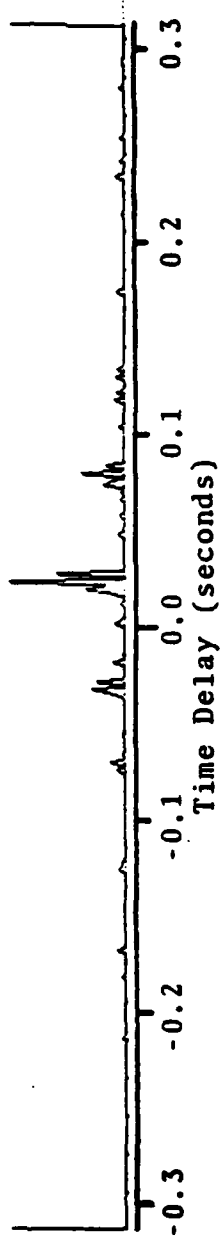
Figure 26b Correlation Function, Shot A14, Geophones 5X vs. 6X, Water Wave
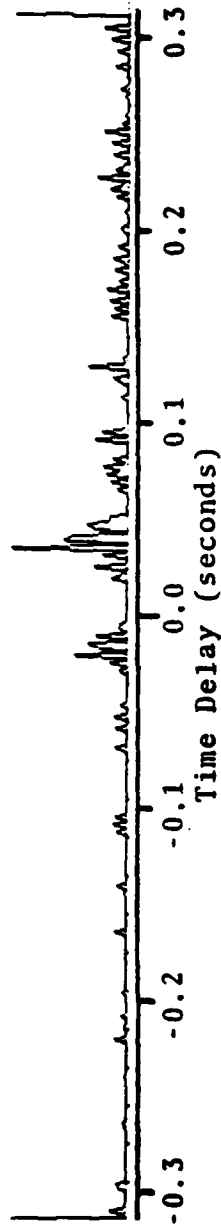
Figure 26c   Correlation Function, Shot A14, Geophones 5Z vs. 4Z, Water Wave
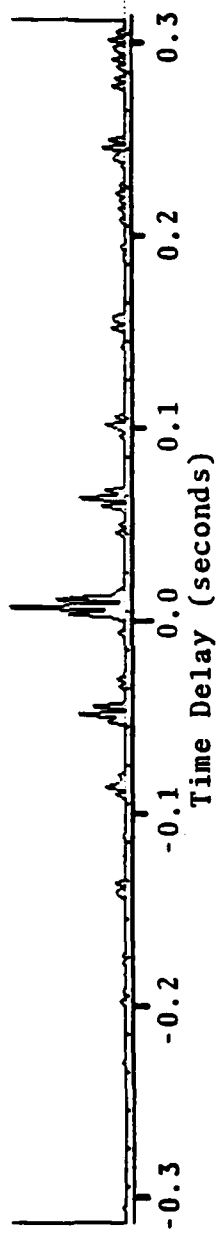
Figure 26d Correlation Function, Shot A14, Hydrophones 5 vs. 4,
Water Wave

As expected from earlier analysis, the correlations were characterized by a strong peak at zero relative time delay, for all sensor pairs. Related strong satellite correlations appeared at intervals of about .025 seconds. Weaker correlations can be seen halfway between the major peaks. These periodic correlation artifacts are readily attributable to the interference signal multiple tonal structure. Assume that an interference signal, $f(t)$, consists of at least two tones, having frequencies, ω_1 and ω_2, respectively. That is,

$$f(t) = e^{i\omega_1 \tau} + e^{i\omega_2 \tau} \qquad (30)$$

where α could be complex-valued. The long term crosscorrelation function, $\chi(\tau)$, obtained from this signal being present, at zero relative time lag, in both channels, would be

$$\chi(\tau) = \left(\frac{1}{1+|\alpha|^2}\right) e^{i\omega_1 \tau} \left(1+|\alpha|^2 e^{i(\omega_2 - \omega_1)\tau}\right) \qquad (31)$$

The modulus correlation amplitude, from equation (31), is

$$|\chi(\tau)| = \left(\frac{1}{1+|\alpha|^2}\right)\sqrt{(1+|\alpha|^4) + 2|\alpha|^2 \cos(\omega_2 - \omega_1)\tau} \qquad (32)$$

which indicates that the correlation function should be modulated at a frequency, $\omega_2 - \omega_1$. Since the spectrograms show the presence of 39 Hz and 78 Hz harmonic component in

ENSCO, Inc.   - 128 -

the interference, then the resultant correlation function should have been modulated at a period of 1/39 Hz = .026 seconds. Presence of the next higher harmonic, also seen in the spectrograms, should have resulted in a modulation period of 1/78 Hz = .013 seconds. Clearly, the observed strong modulation pattern in the correlation functions were caused by the interference signal.

One explanation for such an interference signal is that it was due to a plane wave incident simultaneously across the array; that is, due to a wavefront arriving from either directly above or below the array. Since this signal was present for all shots (covering a period of hours), it seems more likely that it was caused otherwise, perhaps during the recording, playback, or digitizing stages. Intriguingly, the spectral structure of the interference is not inconsistent with that observed from diesel marine engines.

In essentially all results, except for the waterwave arrivals, the interference signal has significantly altered correlation time delays, amplitudes, and statistics. Consequently, the non-waterwave data in Tables 5 and 6 should be regarded with great caution. Consideration was initially given to filtering out the interference by additional digital processing (e.g., bandlimiting, spectral "notching," spectral whitening), but it was recognized that this would have tended to modify signal properties in ways which could not be easily gauged. The effort required to quantify these effects was too extensive to undertake within the limits of this investigation.

It is evident, from Table 5, that the correlation-derived SNR's were nearly always higher for the hydrophones than for the geophones. This probably was the result of the fact that the hydrophones were well isolated from the low frequency (∿5 Hz) seismic noise which affected the geophones. The spectrograms demonstrate this effect. On the other hand, correlation gain (deflection ratio) performance was found to be roughly comparable for both types of sensor. This was not an unexpected result, since directional properties of the arriving signals were maintained in the geophone output, but lost in the hydrophone output. That is, in contrast with a three-axis geophone, a hydrophone would be sensitive to signals (including noise) propagating from all directions.

No clear pattern emerges from the correlation-measured SNR and gain parameters by which one could make decisive judgments regarding the relative merits of hydrophones versus geophones in this application. Indeed, the directly-measured (Table 4) and correlation-measured (Table 5) SNR's do not reflect usual signal propagation attenuation losses. Note, however, that the interference signals might have strongly masked this, and perhaps, other properties of the shot-caused experimental signals.

Apparent array transit speeds for the seismic modes are seen to be larger than derived from the time series analysis. For the purposes of the seismic modeling analysis, it had been assumed that all signals propagated ideally in a horizontal layered medium, undergoing transitions at critical angles. Commonly, apparent seismic transit speeds over an array do not match actual propagation speeds, owing to local layer undulations and inhomogeneities. Also, a non-critically

refracted wavefront incident on an array exhibits a larger
apparent, compared with real, propagation speed. No attempt
was made to model potential local geologies to account for
the apparent speed anomalies. However, the waterwave also
yielded an apparent speed somewhat larger than expected,
although it was not subject to the same propagation vagaries
as were the seismic waves.

2.4 Polarization Filtering

The concept of polarization filtering is based on the
fact that a seismic signal, as observed at a tri-axial geo-
phone, must generate displacements, along the axes, that have
specific relative phase relationships. Consider the seismic
signals as defined in Figure 2S. If a compressive wave is
incident on the geophone from the fourth quadrant, as in
diagram (a), the x-axis displacement will be at maximum posi-
tive when the z-axis displacement is at maximum negative.
Thus, a superposition of the x and z time traces for this
signal would reveal (in the absence of noise) that they were
out of phase by 180° (i.e., by a minus sign). A shear wave,
incident from the fourth quadrant, as in (b), would reveal
x and z time traces that were exactly in phase (i.e., identi-
cal except for amplitude scale). A compressive wave, incident
from the first quadrant, as in (c), would yield x and z time
traces in phase, equivalent to that in the fourth quadrant
shear case, (b). Rayleigh modes would have a 90° or 270°
phase difference, depending on their propagation direction
and type (prograde or retrograde). Similar arguments can be
advanced for Love and other waves. Consequently, processing
gains should be realizable in extracting such signals from
noise, the latter by definition having random relative phase
among the three sensor measurement axes.
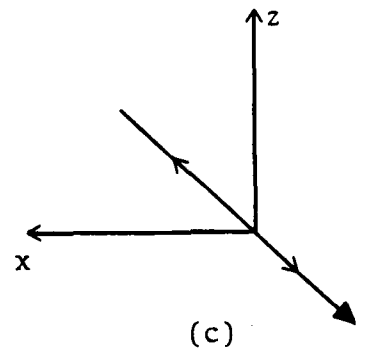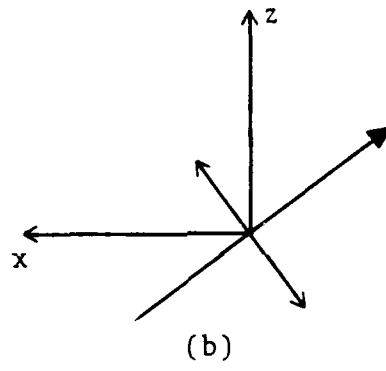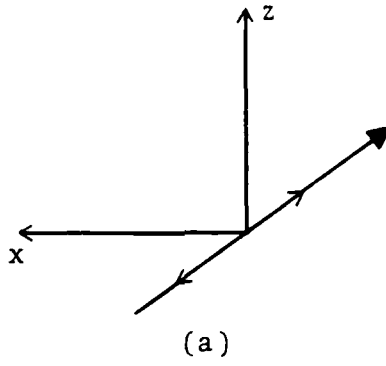
Figure 27 Polarization Configurations

The polarization filtering techniques used here operated in the signal spectral domain. Fast Fourier transformation was first performed on the three axis signals, followed by computation of their relative phase differences at each spectral element (picket). Weights were applied to the separate spectra in a manner which favored the desired phase angles. Spectral pickets which deviated from the desired relative phase relationship were reduced in amplitude, as a function of their deviation. Polarization-filtered time series were then constructed via recombination of these (time-overlapped) modified spectra. Fourier transformation integration lengths were chosen in such a way as to provide near-optimal frequency and phase resolution, for the various arriving modes. Approximately, this resolution varies as

$$(N\delta t / \sqrt{SNR})^{-1}$$

for frequency and

$$2\pi / (\sqrt{SNR})^{-1}$$

for phase, where $N\delta t$ is the integration time of and SNR is the signal-to-noise ratio in the analysis time window.

Polarized time series were then analyzed in the same manner as had been the unfiltered time series. Spectrograms of selected filtered time series are presented in the Figures, for comparison with untiltered time series. A collection of crosscorrelation density plots, computed from polarization
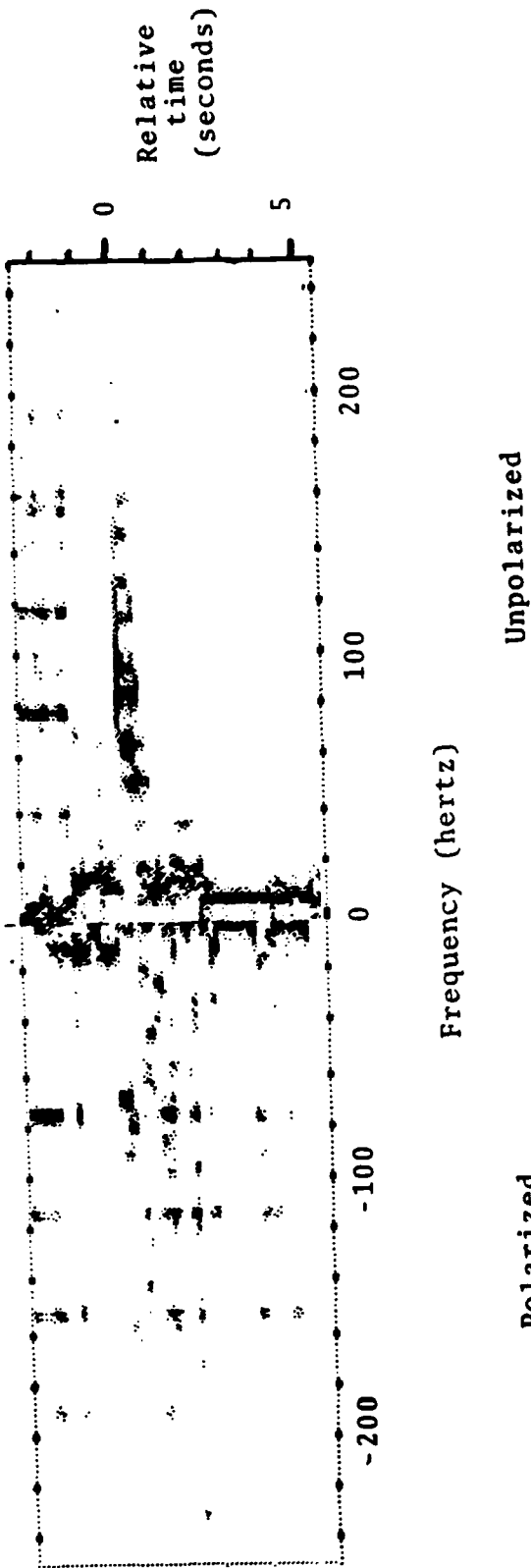
Figure 28a 0° Polarized vs. Unpolarized Spectrogram, Shot A27, Geophone 5X
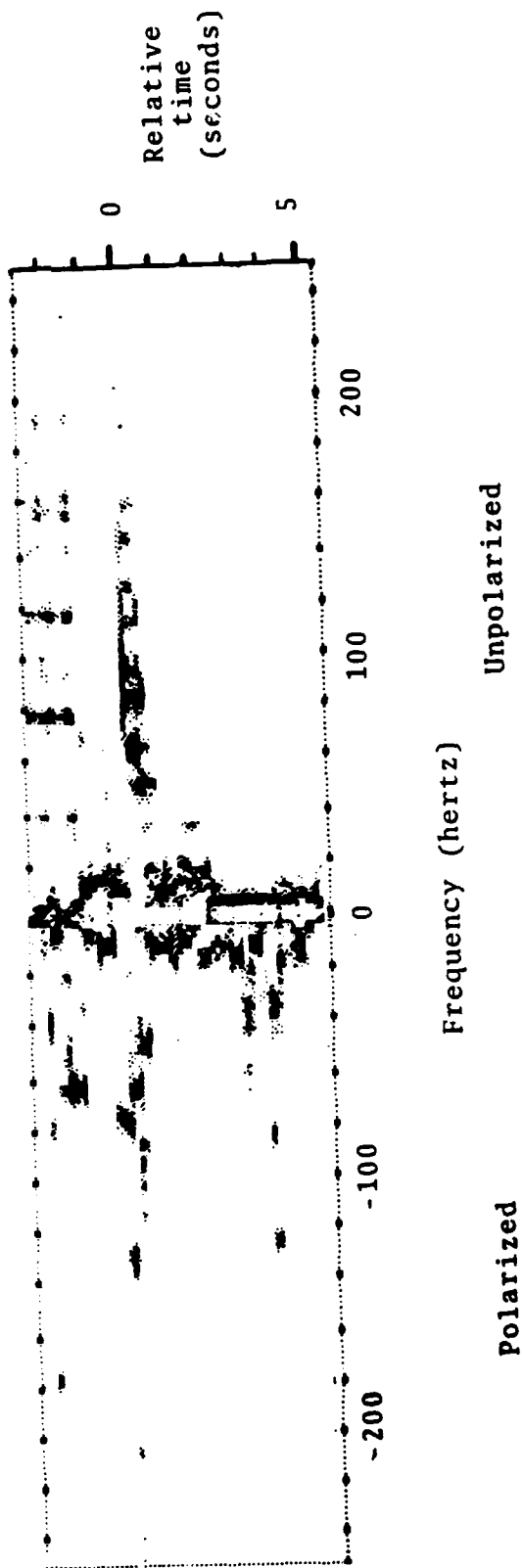
Figure 28b 180° Polarized vs. Unpolarized Spectrogram, Shot A27, Geophone 5X
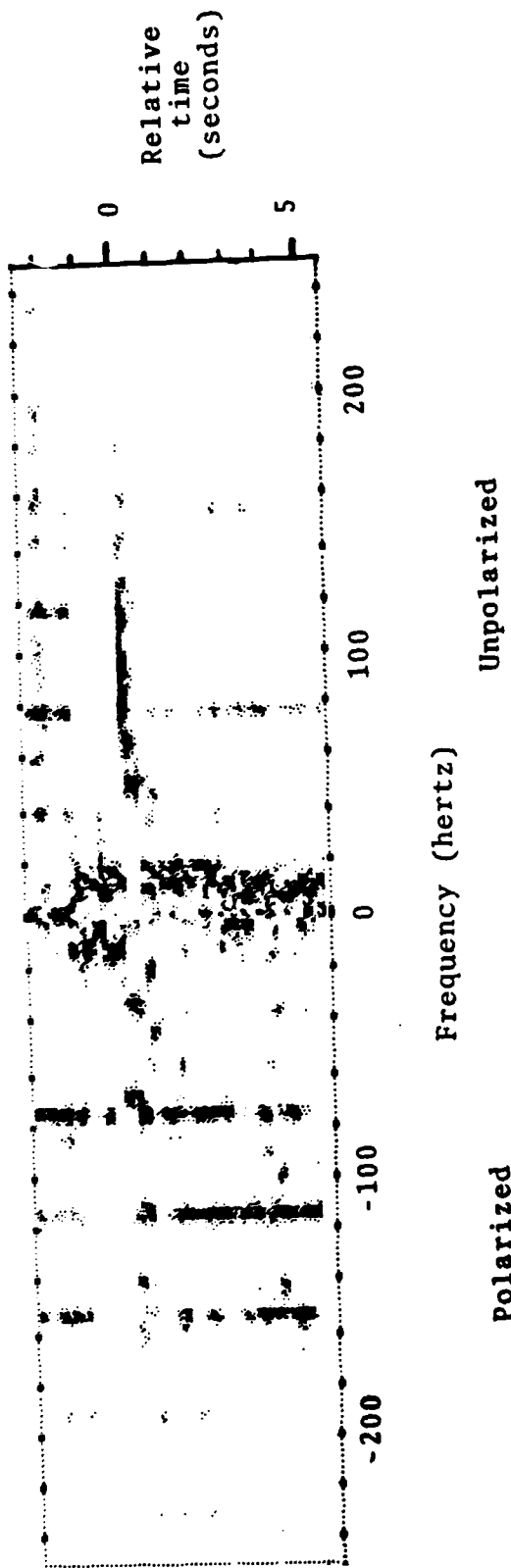
Figure 28c   0° Polarized vs. Unpolarized Spectrogram, Shot A27, Geophone 5Z
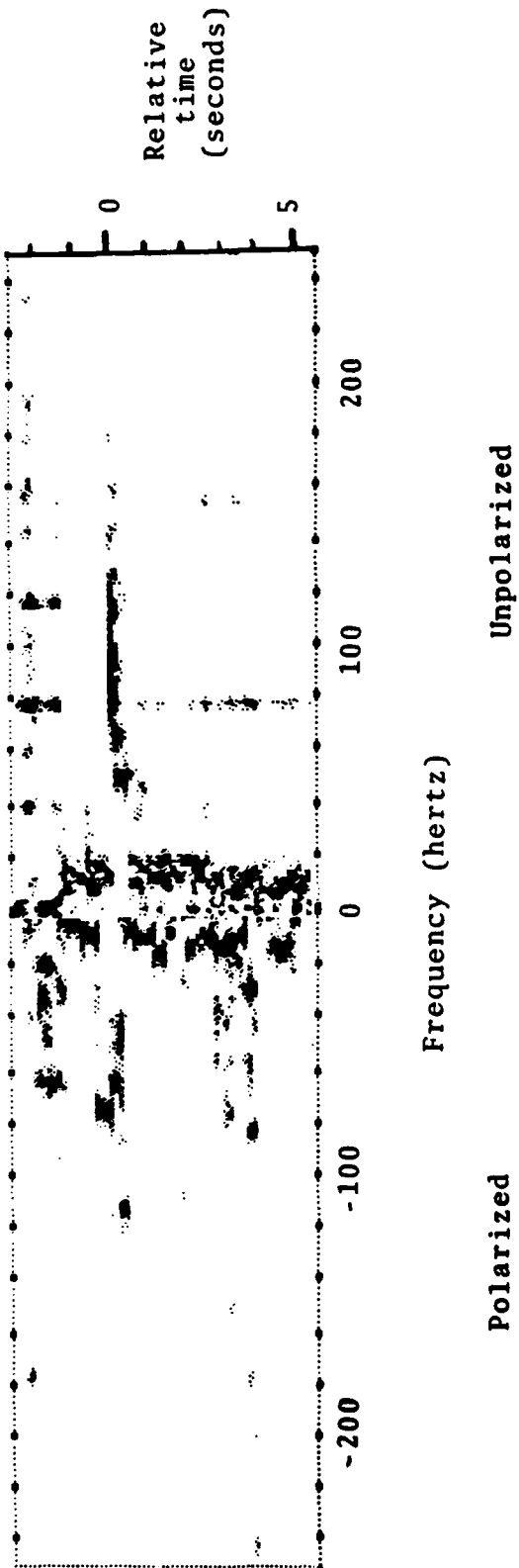
Figure 28d 180° Polarized vs. Unpolarized Spectrogram,
Shot A27, Geophone 5Z
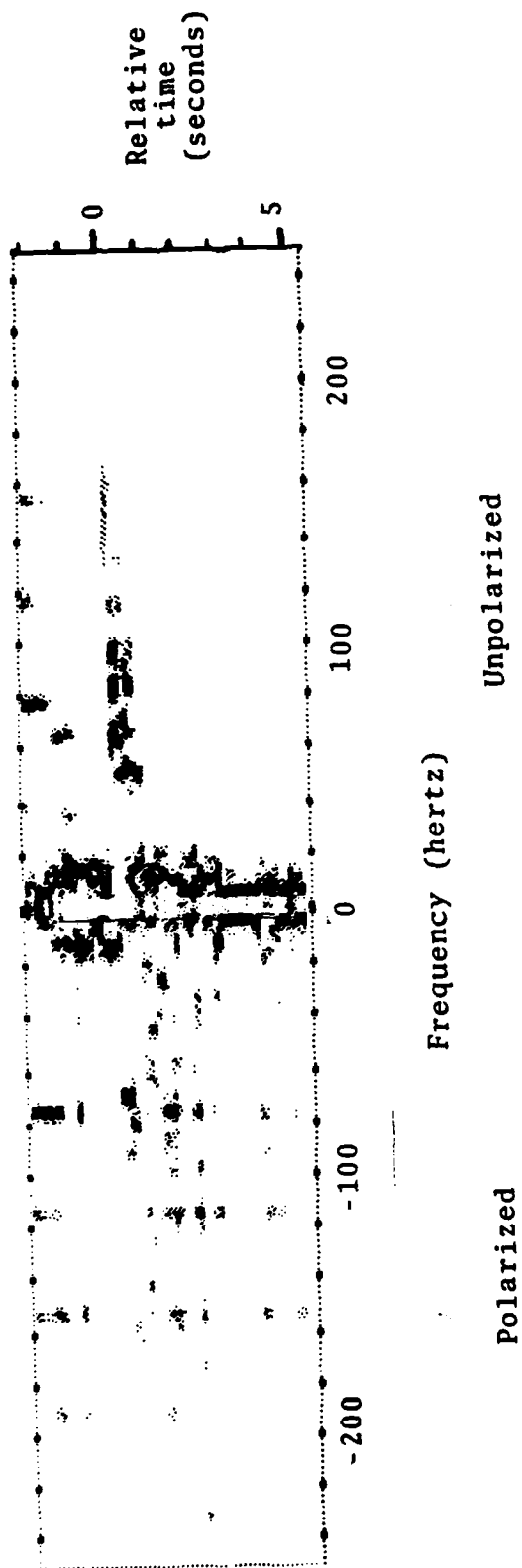
Figure 29a 0° Polarized vs. Unpolarized Spectrogram, Shot A25, Geophone 5X

ENSCO, Inc.   - 138 -
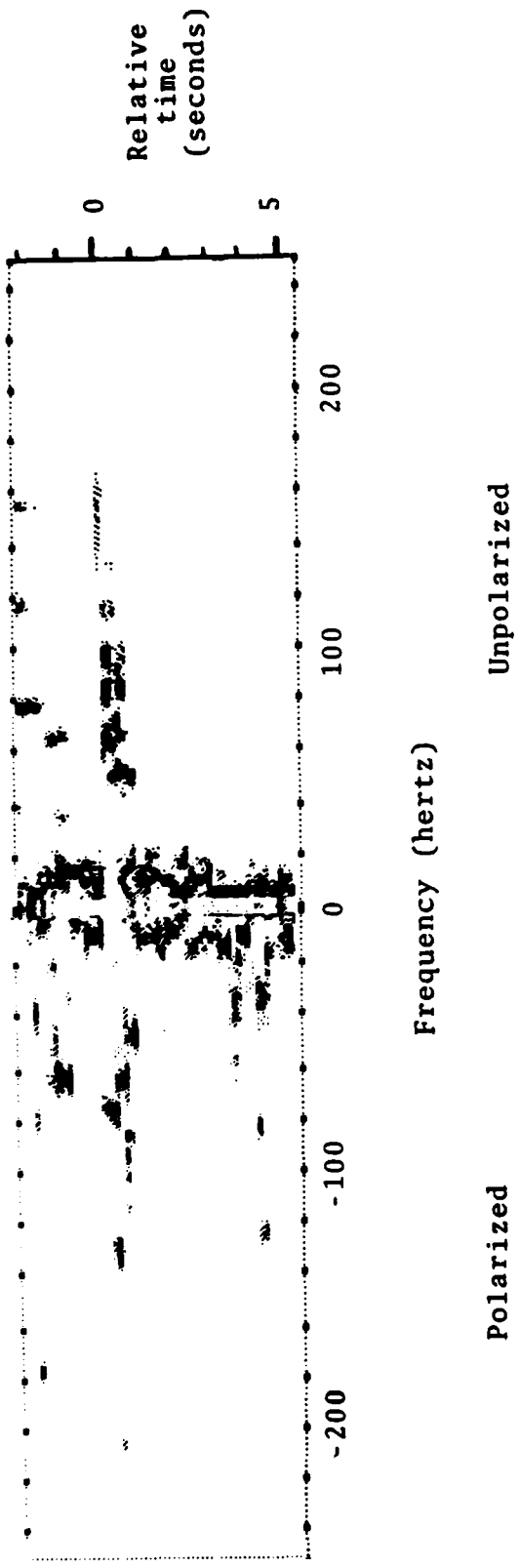
Figure 29b 180° Polarized vs. Unpolarized Spectrogram, Shot A25, Geophone 5X
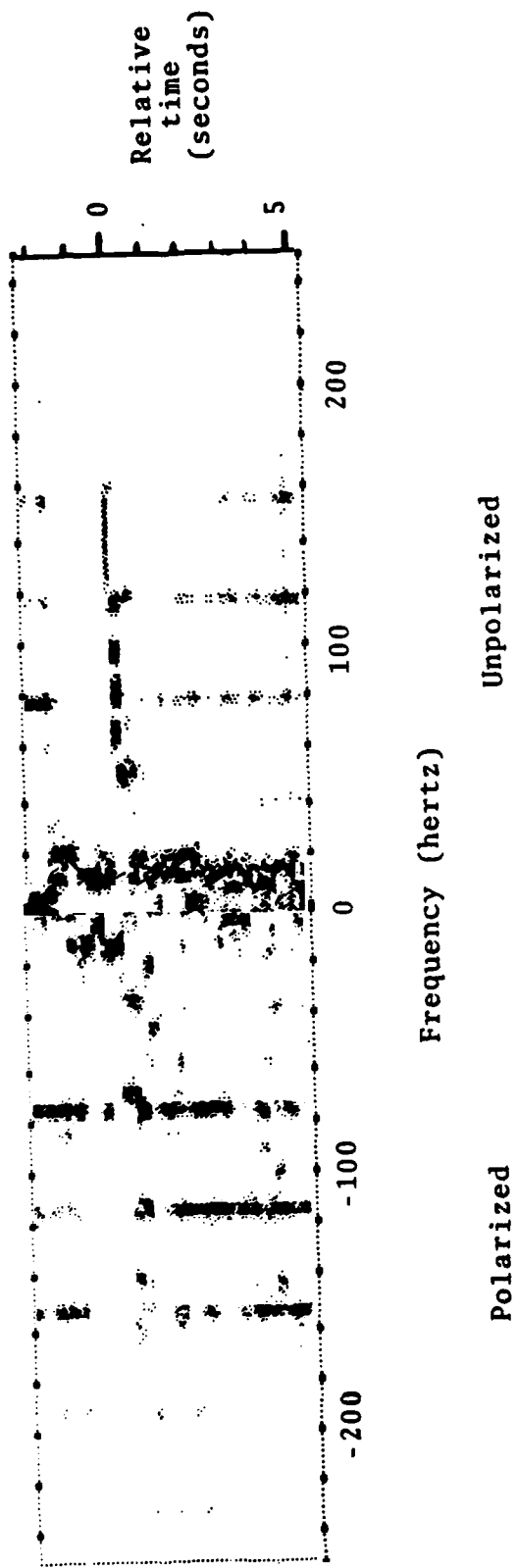
Figure 29c   0° Polarized vs. Unpolarized Spectrogram,
Shot A25, Geophone 5Z
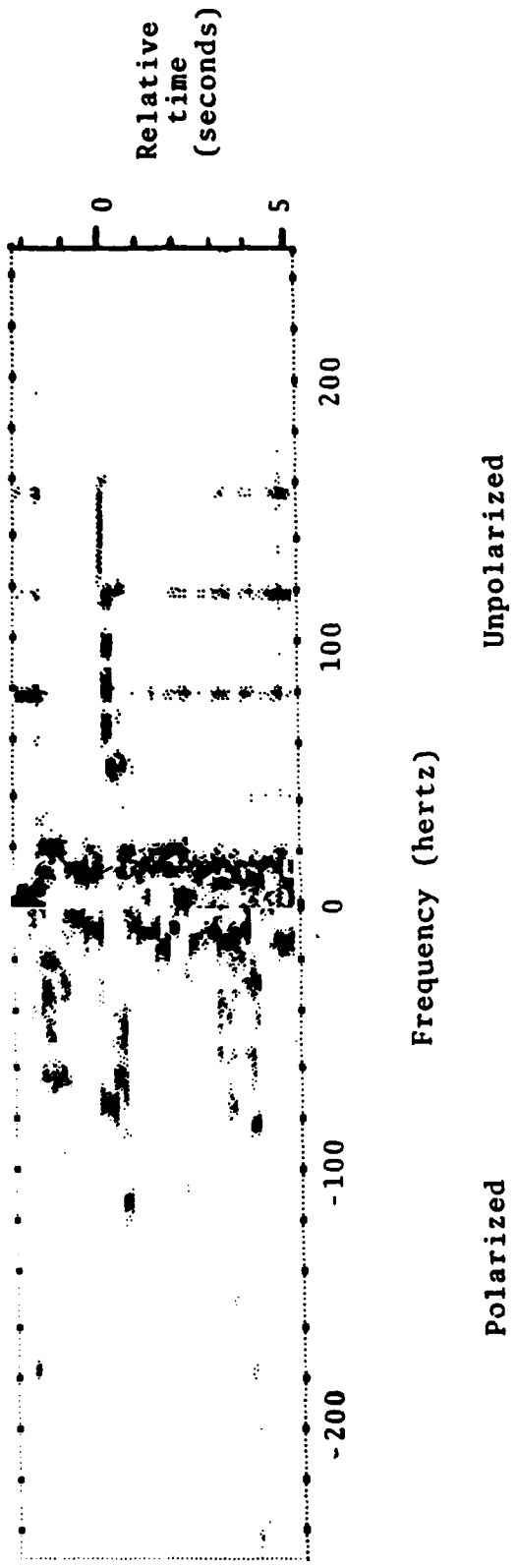
Figure 29d 180° Polarized vs. Unpolarized Spectrogram, Shot A25, Geophone 5Z

ENSCO, Inc. - 141 -
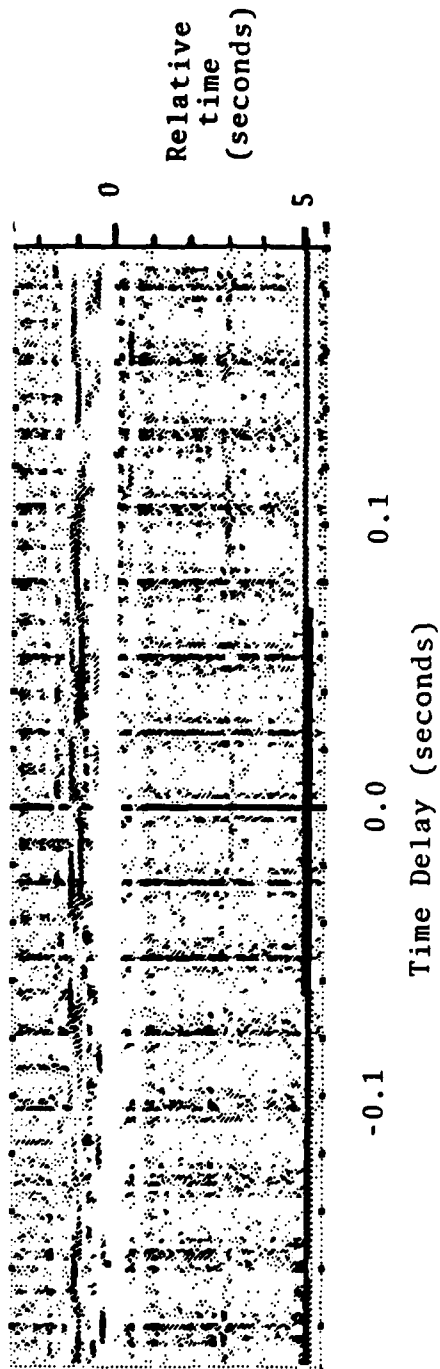
Figure 30a 0° Polarized Correlation Density Display,
Shot A27, Geophoncs 4Z vs. 5Z
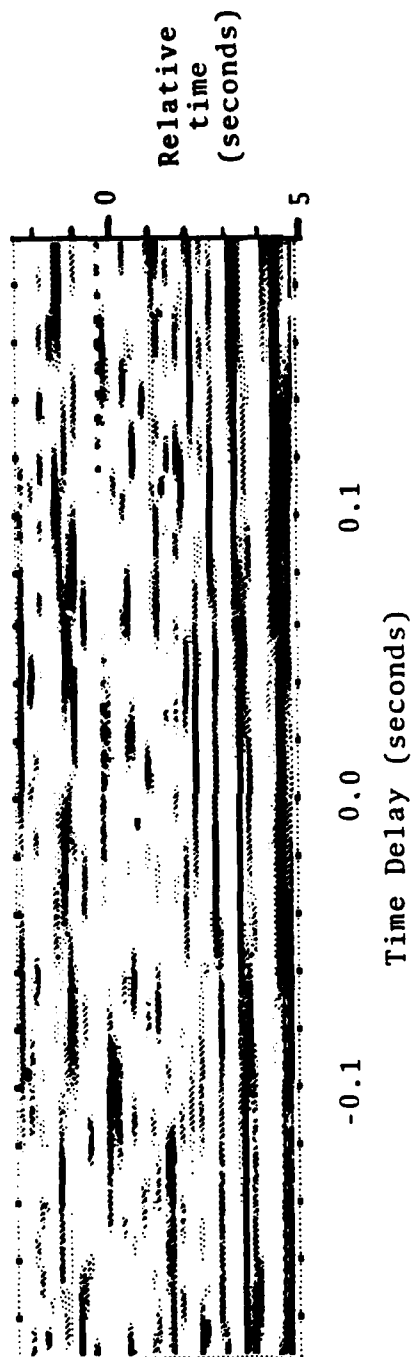
Figure 30b 180° Polarized Correlation Density Display, Shot A27, Geophones 4Z vs. 5Z
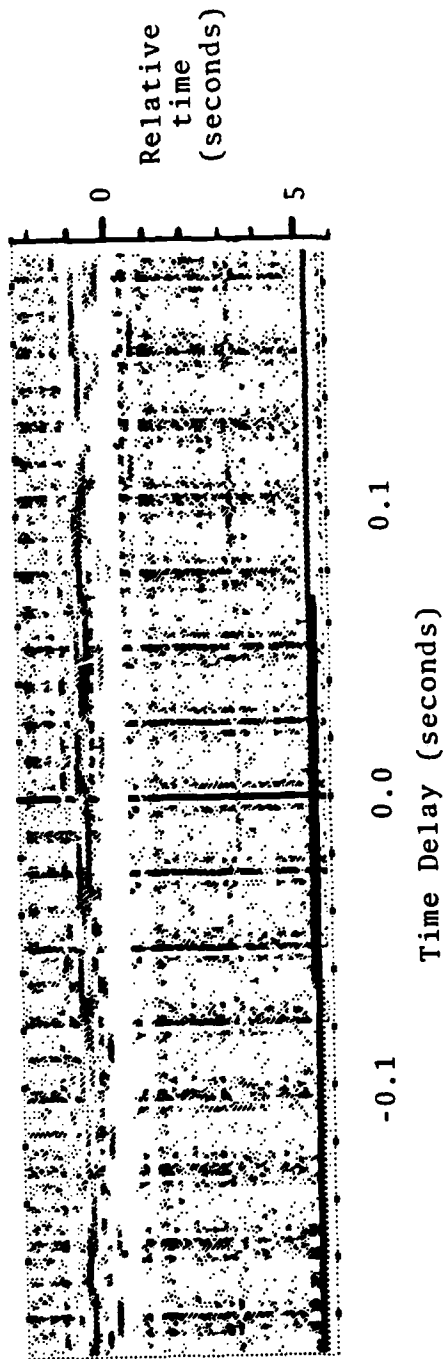
Figure 31a 0° Polarized Correlation Density Display,
Shot A25, Geophones 4Z vs. 5Z
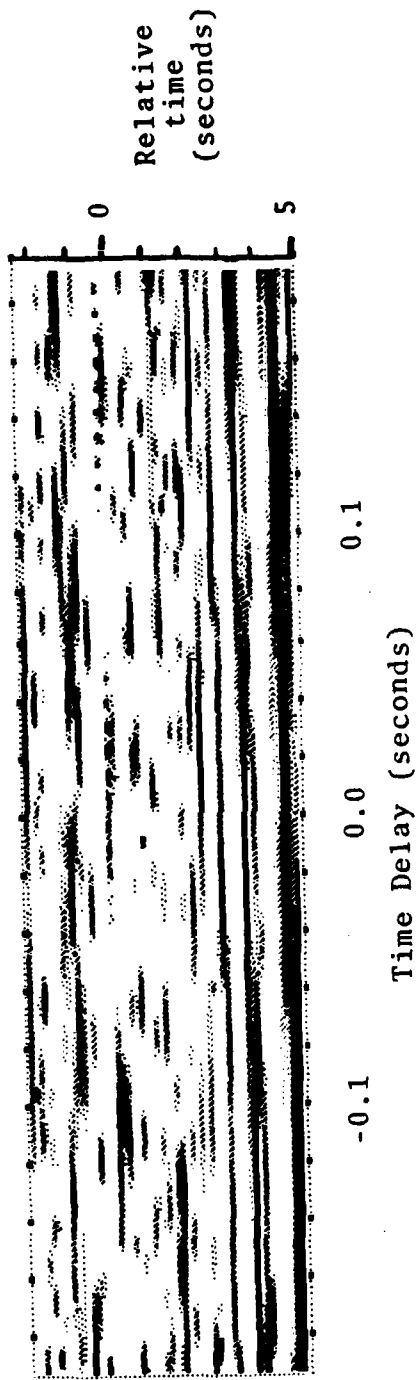
Figure 31b 180° Polarized Correlation Density Display,
Shot A25, Geophones 4Z vs. 5Z

filtered data, is also presented in the Figures. Unfortunately, in the large part, the polarization processing performed here did not perform well at all. These results were in spite of the fact that well-defined phase relationships can be seen clearly in the high resolution time traces, Figures 8 through 11. It is possible that the transfer and modification of existing polarization filter computer code from previous applications were not achieved without error.

A modest degree of successful polarization filtering, nonetheless, is evident in spectral and correlation displays. In the cases where inphase time series were favored, for the x and z axes, the hydroacoustic signals (arriving as a compressive wave from the first quadrant) were preserved (note the persistence of the inphase interference signal). On the other hand, where 180° phase separations were favored, the hydroacoustic (and interference) signals were removed. No obvious pattern emerged, however, for the compressive and shear seismic modes, by which to permit their identification.

3.0 REFERENCES

1. McLeroy, G., "The NCSC Shallow Water Seismic Propagation Study," Naval Coastal Systems Center Report.

2. Carter, G.C., "Estimation of the Magnitude-Squared Coherence Function (Spectrum)," NOSC Technical Report 4343, 19 May 1972.